

AD/A-003 388

PRELIMINARY REPORT ON PROJECT GAS  
EXPLOSIVE SIMULATION TECHNIQUE

Robert A. Bigoni, et al

Air Force Weapons Laboratory

Prepared for:

Defense Nuclear Agency

October 1974

DISTRIBUTED BY:

**NTIS**

National Technical Information Service  
U. S. DEPARTMENT OF COMMERCE

AD A003388



## PRELIMINARY REPORT ON PROJECT GAS EXPLOSIVE SIMULATION TECHNIQUE

Robert A. Bigoni, Major, USAF

Daniel A. Matuska, Captain, USAF

October 1974



Final Report for Period November 1972 - February 1974

Approved for public release; distribution unlimited.

This research was sponsored by the Defense Nuclear Agency under Subtask L25AAXHX634, Work Unit 01, Work Unit Title, "Balloon Simulation of Nuclear Bursts."

Reproduced by  
**NATIONAL TECHNICAL  
INFORMATION SERVICE**  
U S Department of Commerce  
Springfield VA 22151

**AIR FORCE WEAPONS LABORATORY**  
**Air Force Systems Command**  
**Kirtland Air Force Base, NM 87117**

UNCLASSIFIED

SECURITY CLASSIFICATION OF THIS PAGE (When Data Entered)

REPORT DOCUMENTATION PAGE		READ INSTRUCTIONS BEFORE COMPLETING FORM
1. REPORT NUMBER AFWL-TR-74-252	2. GOVT ACCESSION NO.	3. RECIPIENT'S CATALOG NUMBER
4. TITLE (and Subtitle)  PRELIMINARY REPORT ON PROJECT GAS EXPLOSIVE SIMULATION TECHNIQUE		5. TYPE OF REPORT & PERIOD COVERED Final Report November 1972 - February 1974
7. AUTHOR(s)  Major Robert A. Bigoni Captain Daniel A. Matuska		6. PERFORMING ORG. REPORT NUMBER
9. PERFORMING ORGANIZATION NAME AND ADDRESS  Air Force Weapons Laboratory Kirtland Air Force Base, NM 87117		8. CONTRACT OR GRANT NUMBER(s)
11. CONTROLLING OFFICE NAME AND ADDRESS  Air Force Weapons Laboratory Kirtland Air Force Base, NM 87117		10. PROGRAM ELEMENT, PROJECT, TASK AREA & WORK UNIT NUMBERS  Program Element WDNB4601 Subtask HX634
14. MONITORING AGENCY NAME & ADDRESS (if different from Controlling Office)  Air Force Weapons Laboratory Kirtland Air Force Base, NM 87117		12. REPORT DATE October 1974
		13. NUMBER OF PAGES 128
		15. SECURITY CLASS. (of this report)  UNCLASSIFIED
		15a. DECLASSIFICATION/DOWNGRADING SCHEDULE
16. DISTRIBUTION STATEMENT (of this Report)  Approved for public release; distribution unlimited.		
17. DISTRIBUTION STATEMENT (of the abstract entered in Block 20, if different from Report)  Same as block 16.		
18. SUPPLEMENTARY NOTES		
19. KEY WORDS (Continue on reverse side if necessary and identify by block number) air blast calculation nuclear fireball simulation gas detonation		
20. ABSTRACT (Continue on reverse side if necessary and identify by block number) The Air Force Weapons Laboratory (AFWL) fielded a series of experiments to simulate low-altitude nuclear fireball phenomenology. Thirty-two-foot diameter gas containers were filled with a near-stoichiometric mixture of CH <sub>4</sub> and O <sub>2</sub> and were detonated with yields equivalent to approximately 1500 pounds of TNT. The Reynolds number describing the motion of the resulting hot gases was high enough so that the motion of the gases was dynamically similar to that in a nuclear fireball. Experiments fielded included AGA temperature measurements by Los Alamos Scientific Laboratory (LASL), IR vidicons by General Electric (GE) (OVER)		

DD FORM 1 JAN 73 1473

EDITION OF 1 NOV 65 IS OBSOLETE

UNCLASSIFIED

SECURITY CLASSIFICATION OF THIS PAGE (When Data Entered)

**UNCLASSIFIED**

SECURITY CLASSIFICATION OF THIS PAGE(When Data Entered)

**ABSTRACT (Cont'd)**

Company, an IR rapid scanning iterferometer by Air Force Cambridge Research Laboratories (AFCRL), hot-wire anemometry by TRW Systems Group, and pressure gauges and a Raman scattering experiment by AFIL.

**UNCLASSIFIED**

SECURITY CLASSIFICATION OF THIS PAGE(When Data Entered)

## PREFACE

The authors wish to express their appreciation to Captain R. Harris and Lt T. Fabian of the Air Force Weapons Laboratory who made the MACE chemistry calculations, Captain M. Marcucci, Mr. F. X. Doherty, and Mr. Jim Drye of the Air Force Cambridge Research Laboratories who helped design the gas containers, Dr. S. Fields of the General American Research Division of General American Transportation Corporation who helped design the balloon fill system, and Dr. J. Doran of GE TEMPO who compiled this report.

Appreciation is also extended to the experimenters of the Los Alamos Scientific Laboratory, Space Sciences Laboratory of General Electric Company, TRW Systems Group and the Air Force Cambridge Laboratories for their cooperation and patience during the fielding of these experiments. The guidance and advice of Lt Colonel M. Monahan of Defense Nuclear Agency is also gratefully acknowledged.

## CONTENTS

<u>Section</u>		<u>Page</u>
I	INTRODUCTION	8
II	THE GEST EXPERIMENT	10
	1. Test Site Location	10
	2. Test Site Layout	10
	3. Physical Setup	10
	4. Instrumentation	14
	5. Photo Coverage	15
III	CALCULATIONS	22
	1. Early Calculations	22
	2. New Calculations	22
IV	INDIVIDUAL EXPERIMENTS	39
	1. AGA Temperature Measurements	40
	2. Measurement of Infrared Spectra in the Range 1.56 to 4.67 Microns	43
	3. Raman Scattering Experiment to Determine Air Entrainment Rates.	60
	4. Fast Response Temperature Measurements	63
	5. Infrared Vidicon Observations	72
	6. AFWL Test Measurement Results	100
V	DISCUSSION OF RESULTS	118
	REFERENCES	124

## ILLUSTRATIONS

<u>Figure</u>		<u>Page</u>
1	GEST Test Site Location	10
2	GEST Test Site Layout	11
3	Leakage Testing of 10 m Mylar Balloon	12
4	MB-4 Balloon Prior to Detonation	16
5	MB-4 Balloon Detonating	17
6	MB-4 4 Seconds after Detonation	18
7	MB-4 8 Seconds after Detonation	19
8	MB-4 12 Seconds after Detonation	20
9	MB-4 Torus 60 Seconds after Detonation	21
10	Burned Methane Density Contours at 0.500 Seconds - HULL Calculation	24
11	Burned Methane Density Contours at 1.000 Seconds - HULL Calculation	25
12	Burned Methane Density Contours at 2.000 Seconds - HULL Calculation	26
13	Burned Methane Density Contours at 3.000 Seconds - HULL Calculation	27
14	Early Time Average Rise Velocity and Altitude versus Time - HULL Calculation	28
15	Late Time Altitude versus Time - HULL Calculation	30
16	Torus Radius versus Time - HULL Calculation	31
17	Late Time Rise Velocity versus Time - HULL Calculation	32
18	Peak Temperature versus Time - Old and New HULL Calculations	33
19	Temperature Gradients versus Time - Old and New HULL Calculations	35
20	Constant Temperature Contours at 2.000 Seconds - HULL Calculations	36
21	Constant Temperature Gradient Contours at 2.000 Seconds - HULL Calculations	37
22	Constant Temperature Contours at 2.000 Seconds - Old HULL Calculations	38
23	Peak Brightness Temperature versus Time - LASL AGA Measurements - Event MB-1	41
24	Peak Brightness Temperature versus Time - LASL AGA Measurements - Event MB-2	42

# ILLUSTRATIONS (Continued)

<u>Figure</u>		<u>Page</u>
25	Spectral Irradiance for Event DMB-1 at 0.20 Seconds	45
26	Spectral Irradiance for Event DMB-1 at 1.59 Seconds	46
27	Spectral Irradiance for Event DMB-1 at 3.27 Seconds	47
28	Spectral Irradiance for Event DMB-1 at 7.54 Seconds	48
29	Spectral Irradiance versus Time for Event DMB-1	49
30	Spectral Irradiance for Event MB-3 at 0.11 Seconds	50
31	Spectral Irradiance for Event MB-3 at 5.15 Seconds	51
32	Spectral Irradiance versus Time for Event MB-3	53
33	Atmospheric Spectral Transmission for Event MB-3	54
34	Spectral Radiant Intensity for Event MB-3 at 0.11 Seconds	55
35	Spectral Radiant Intensity for Event MB-3 at 5.15 Seconds	56
36	Relative Spectral Irradiances at $3414\text{ cm}^{-1}$ - GEST Events	57
37	Relative Spectral Irradiance at $2396\text{ cm}^{-1}$ - GEST Events	59
38	Hot Wire Probe Configurations for GEST Temperature Measurements	64
39	Probe Strut Installation - Event MB-4	65
40	Thermal Sensor Locations - Events MB-1 through MB-4	67
41	Thermal Sensor Locations - Event DMB-1	68
42	Thermal Time Traces - Event MB-4	69
43	Expanded Thermal Time Traces - Event MB-4	70
44	Predicted Event Temperature Profile at $T=2.0$ Seconds	73
45	Predicted Event Temperature Profile at $T=6.0$ Seconds	74
46	Vidicon Spectral Filter Transmission Calibration Curve	76
47	Ge: Cu Vidicon Spectral Response	77
48	Vidicon Measurement Dynamic Range	78
49	Belvoir Camera Post - Mission Calibration	80
50	Sample Vidicon Data Frame	82
51	MB-4 Vidicon Data Frames	84
52	Torus Orientation versus Time - Event MB-4	89
53	Torus Region Height versus Time - Event MB-4-Camera 1	90
54	Torus Region Height versus Time - Event MB-4-Camera 2	91
55	Torus Region Width versus Time - Event MB-4-Camera 1	92



# ILLUSTRATIONS (Continued)

<u>Figure</u>		<u>Page</u>
56	Torus Region Width versus Time - Event MB-4-Camera 2	93
57	Torus Region Separation versus Time - Event MB-4-Camera 1	94
58	Image Width versus Time - Event MB-4-Camera 1	95
59	Cloud Mean Altitude versus Time - Event MB-4-Camera 1	96
60	Spectral Radiant Intensity versus Horizontal Distance-Upper Portion of Image - Event MB-4	97
61	Spectral Radiant Intensity versus Horizontal Distance-Lower Portion of Image-Event MB-4	98
62	Iso-Intensity Contour - Event MB-4	99
63	GEST TOA Crystal Deployment Configuration	101
64	GEST Pressure Gage Deployment Configuration-MB Series	104
65	GEST Event DMB-1 Blast Pressure Gage Layout	105
66	GEST DMB-1 Pressure Measurement 100	106
67	GEST DMB-1 Pressure Measurement 101	107
68	GEST DMB-1 Pressure Measurement 102	108
69	GEST DMB-1 Pressure Measurement 103	109
70	GEST DMB-1 Pressure Measurement 104	110
71	GEST DMB-1 Pressure Measurement 105	111
72	GEST DMB-1 Pressure Measurement 106	112
73	GEST DMB-1 Pressure Measurement 107	113
74	GEST DMB-1 Pressure Measurement 108	114
75	GEST DMB-1 Pressure Measurement 109	115
76	GEST DMB-1 Pressure Measurement 110	116
77	GEST DMB-1 Pressure Measurement 111	117
78	Power Spectrum of MB-4 Temperature Measurement	119
79	Comparison of LASL Computed Temperatures with HULL Predictions - Event MB-2	121
80	Torus Radius versus Time - Optical Measurements and HULL Predictions Compared	122
81	Altitude versus Time - MB Series and HULL Prediction Compared	123

## SECTION I

### INTRODUCTION

Project GEST (Gas Explosive Simulation Technique) consisted of a series of tests intended to simulate late-time, low altitude nuclear fireball phenomenology. Individual events involved the explosion of a large balloon filled with a detonable (near stoichiometric) mixture of methane and oxygen. A gaseous mixture was chosen as the energy source rather than a conventional high explosive (TNT, AN/FO, etc) for two reasons. Gas explosives are of low density so that there is no problem with jetting of hot species out of the fireball. In addition, gases tend to form a more stable initial fireball.

In a nuclear detonation the early escape of energy is radiative. As the temperature drops below a few thousand degrees, however, the energy loss by radiation decreases drastically. The hot fireball now expends energy by doing PdV work on the surrounding atmosphere and grows until it reaches pressure equilibrium. The result is that there is now a hot, underdense, mixture of gases and bomb materials in the atmosphere. Due to bouyancy the fireball starts rising. The flow around the rising fireball deforms it until it becomes finally a fully developed torus.

In rising through the atmosphere the fireball entrains air into itself. This entrained air interacts with the bomb debris to form hot metal oxides which radiate in the 10-12  $\mu$  wavelength region. Since the atmosphere is transparent to these wavelengths the effects of the radiated energy are felt at a considerable distance from the detonation.

The mechanisms by which air entrainment and subsequent mixing with bomb debris take place are not completely understood. Turbulence at the edge of the fireball and subsequent torus may be a primary factor in the entrainment process. Knowledge of the details of the air entrainment and mixing processes would be of great value in determining the rate of metal oxide formation and the consequent long wavelength infrared (LWIR) emission.

Fireball radar clutter is another facet of late time nuclear fireball phenomenology of great interest. Its source mechanism could be high temperatures and high temperature gradients at the edge of the torus, or it could be due to reflections from turbules of size comparable to the radar wavelength. Although it was not expected that the questions of radar clutter

origin could be fully answered in the types of experiment discussed here, some additional insight could perhaps be gained.

The role of turbulence as a mechanism in the various phenomena of interest has not been resolved. Most of the production-type hydro codes are laminar flow codes and do not take turbulence into account. A study of the GEST series test results in comparison with HULL predictions should, hopefully, enable a determination as to the desirability, or necessity, for introducing turbulence into the codes.

A brief description of the experimental setup for the five GEST events involving 10 m diameter balloons filled with a detonable mixture of methane and oxygen is given in Section II.

Section III discusses the theoretical modeling of the GEST event using the HULL code. Preliminary results from the diagnostic instrumentation which was fielded in an attempt to better understand the fireball and torus phenomenology are included in Section IV.

The last section, Section V, presents the preliminary conclusions which have been drawn from the first five GEST events. Some comparisons are made between predicted and measured values of torus and fireball parameters. These comparisons reflect favorably on the HULL code.

A sixth GEST event - a double burst - is tentatively scheduled for February 1975. This will be a repeat of the fifth GEST event which was a double balloon shot. Because of operational difficulties one of the two balloons was not charged with the correct amount of methane and the primary objective of that particular experiment - to observe air flow interactions for multi bursts - was not met.

In general, the first four GEST events which involved the detonations of single balloons can be considered to have been successfully conducted and much useful data was obtained.

## SECTION II

### THE GEST EXPERIMENT

This section gives only a brief description of the GEST experiments and related technologies. The final report on the test series will contain more detailed descriptions of the physical equipments and their use and deployment.

#### 1. TEST SITE LOCATION

The GEST series was carried out at the Sandia Laboratories Aerial Cable Test Facility in the southeast field test areas of Kirtland Air Force Base. Ground zero location was  $34^{\circ}58'$  North latitude and  $106^{\circ}27'$  West longitude. Figure 1 shows the location of the test site with respect to topographical and cultural features of the surrounding area.

#### 2. TEST SITE LAYOUT

The Sandia Cable Test Facility is characterized by having a 1-1/4 inch diameter steel cable strung across a relatively flat but sloping area between hills on either side of a canyon. The maximum height to which the cable can be raised above surface ground zero (SGZ) is 193 feet. Figure 2 is a plan view of the area showing the locations of camera stations, instrumentation vans, etc. with respect to the cable and SGZ.

#### 3. PHYSICAL SETUP

##### a. Balloons

The envelopes of the balloons used for the main GEST events were constructed of three mil Mylar. The Mylar was coated on both sides with a 5000 Å thick layer of aluminum. They were, when inflated, 10 meters in diameter and had a volumetric capacity of 17,157 cubic feet. Figure 3 shows one of the balloons undergoing leakage testing.

The balloons were filled with a mixture of methane ( $\text{CH}_4$ ) and oxygen ( $\text{O}_2$ ) in the approximate ratio of 1 part to 2 parts, respectively, by volume. The detonation of this mixture in the quantity assumed was approximately equivalent in energy yield to the detonation of 1500 pounds of TNT.

The measured quantity of oxygen was first pumped into the balloon through a fitting and poppet valve located at the lowermost point of the balloon. After the required amount of  $\text{O}_2$  was in the balloon, the methane was pumped in. A diffuser installed on the poppet valve acted to introduce

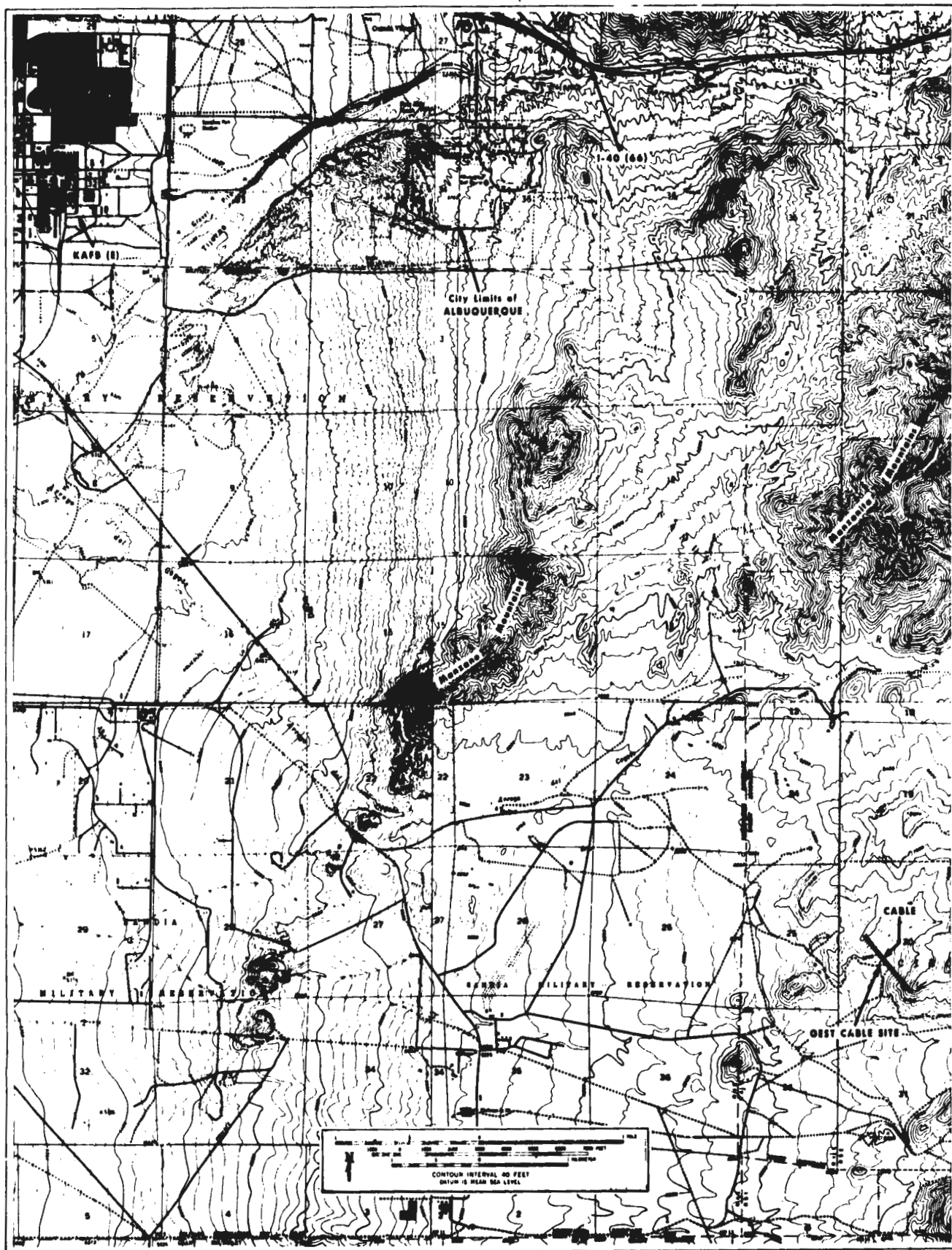


Figure 1. GEST Test Site Location

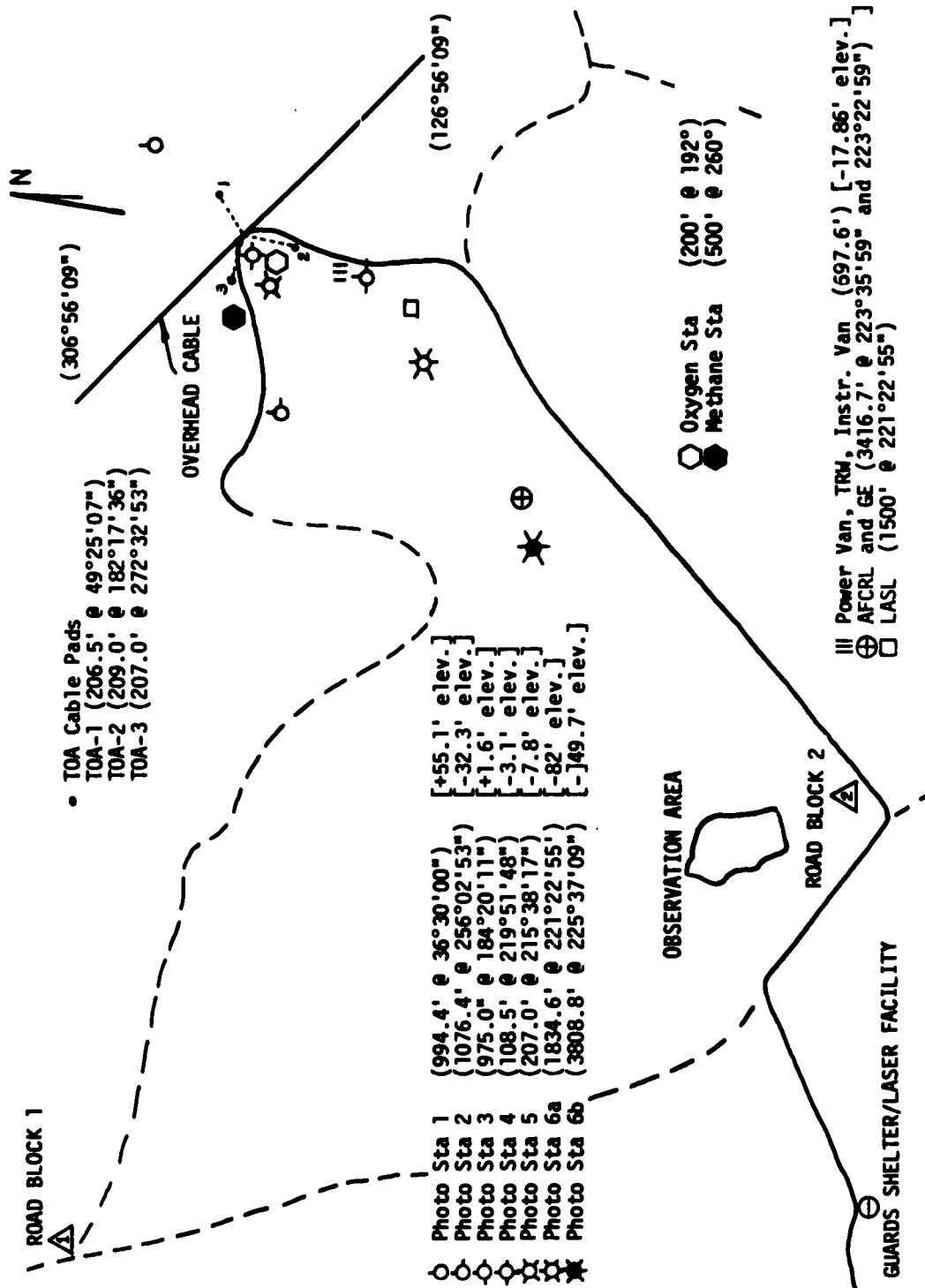


Figure 2. GEST Test Site Layout



Figure 3. Leakage Testing of 10m Mylar Balloon

turbulent motion in the gas flow. The lighter  $\text{CH}_4$  bubbled up through the heavier  $\text{O}_2$  in a light plume which effectively caused mixing of the gases in a reasonably short time (reference 1).

After filling, the balloon was hoisted to the detonation altitude. See table 1 which lists the schedule of GEST events, the relative configurations, and the computed yields. Events MB-1 through MB-4 were single balloon events; event DMB-1 was a double balloon event.

TABLE 1. SCHEDULE OF GEST EVENTS

EVENT	DATE	BURST ALT. (FT)	SEPARATION (FT)	YIELD ( $10^9$ JOULES)
MB-1	28 Nov 73	150	NA	2.86
MB-2	30 Nov 73	140	NA	2.93
MB-3	11 Dec 73	130	NA	3.00
MB-4	13 Dec 73	130	NA	2.72
DMB-1	19 Jan 74	130	100	1.3-1.6 and 3.20

Detonation of the explosive mixture was initiated by three RP-1 detonators in each balloon. Two of the detonators for each balloon were surrounded by plastic sacks each containing 2.5 pounds of 5-10  $\mu$  aluminum powder. This powder was dispersed through the balloon when the detonators were fired, and acted to render the late fireball and the torus optically visible. Subsequent to the second shot (MB-2) 50 gm of C-4 was wrapped around each of the powder dispersing detonators to improve powder dispersal.

#### 4. INSTRUMENTATION

The Air Force Weapons Laboratory (DEX) fielded time of arrival (TOA) gages and blast pressure gages on each of the five events. Experiments involving IR measurements and hot-wire anemometry were fielded by AFCRL, GE, LASL and TRW. These experiments are described in Section IV, together with some of the test results and early conclusions. A laser experiment fielded by AFWL, but aborted due to equipment malfunction, to measure Raman scattering from the fireball and torus is also described there.



## 5. PHOTO COVERAGE

Figure 2 gives the location of the various camera stations. Table 2 lists the various types of photo coverage at each of the stations. Good photo footage was obtained on all events and a documentary film is in preparation as part of the final report. Figures 4 thru 9 are a sequence of photos of the MB-4 event from prior to detonation to formation of a "picture book" torus.

Table 2. Photographic Coverage of GEST Events

STATION	EVENTS	CAMERA	FR/SEC.	LENS	COMMENTS
1	A11	16 mm Hycam	5000	Zoom	MB-1 thru -4 75 mm lens setting DMB-1 50 mm lens setting 400' color T=3 sec. 200' color T=62.3 sec. B&W 400' B&W T=53 sec.
(Dist=994.4')	A11 A11 A11	16 mm Milliken 70 mm Hasselblad 70 mm Multidata	126 4/3 30	10 mm 50 mm 5"	
2	A11	16 mm Hycam	5000	Zoom	MB-1 thru -4 75 mm lens setting DMB-1 43 mm lens setting 200' color T=20 sec. 200' color T=20 sec. 200' color T=125 sec. -aimed up into sky B&W 400' B&W T=78 sec.
(Dist=1076.4')	MB-1 thru MB-4 DMB-1 A11	16 mm Milliken 16 mm Milliken 16 mm Milliken	400 400 64	25 mm 20 mm 10 mm	
	A11 MB-1, MB-2	70 mm Hasselblad 70 mm Photosonic	4/3 20	80 mm 80 mm	
3	MB-1 thru MB-4 DMB-1 A11 MB-1, MB-2	16 mm Milliken 16 mm Milliken 70 mm Multidata 70 mm Multidata	500 400 45 30	25 mm 20 mm 10" 5"	200' color T=16 sec. 200' color T=16 sec. 400' B&W T=35 sec. 400' B&W T=53 sec. -looking up at sky 400' B&W T=78 sec. color negatives following torus
(Dist=975.0')	MB-3, MB-4, DMB-1 A11	70 mm Photosonic 70 mm Still	20 rapid	80 mm 85 mm	
4	A11	16 mm Milliken	48	10 mm	200' color T=166 sec. -looking up through torus
(Dist=108.5')	MB-3, MB-4, DMB-1	16 mm Milliken	48	10 mm	200' color T=166 sec. -looking up through torus
(Dist=207')	MB-3	70 mm Multidata	10	5"	400' B&W T=3 min.
6a	(Dist=1834.6')				
6b	MB-4, DMB-1 DMB-1	70 mm Multidata 16 mm Milliken	10 32	5" 15 mm	400' B&W T=3 min. 200' color T=5 min.
(Dist=3808.8')					

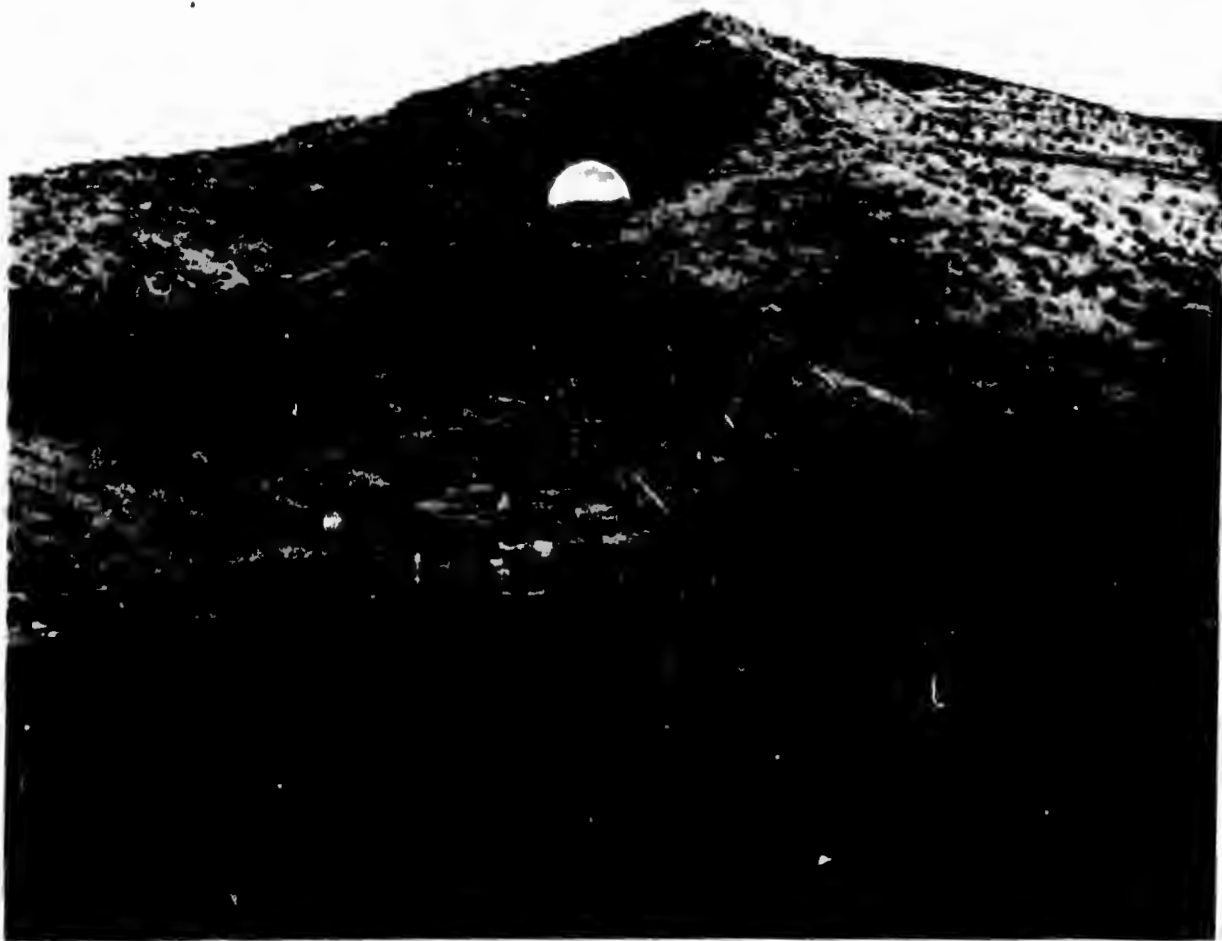


**Figure 4. MB-4 Balloon Prior to Detonation**



Figure 5. MB-4 Balloon Detonating

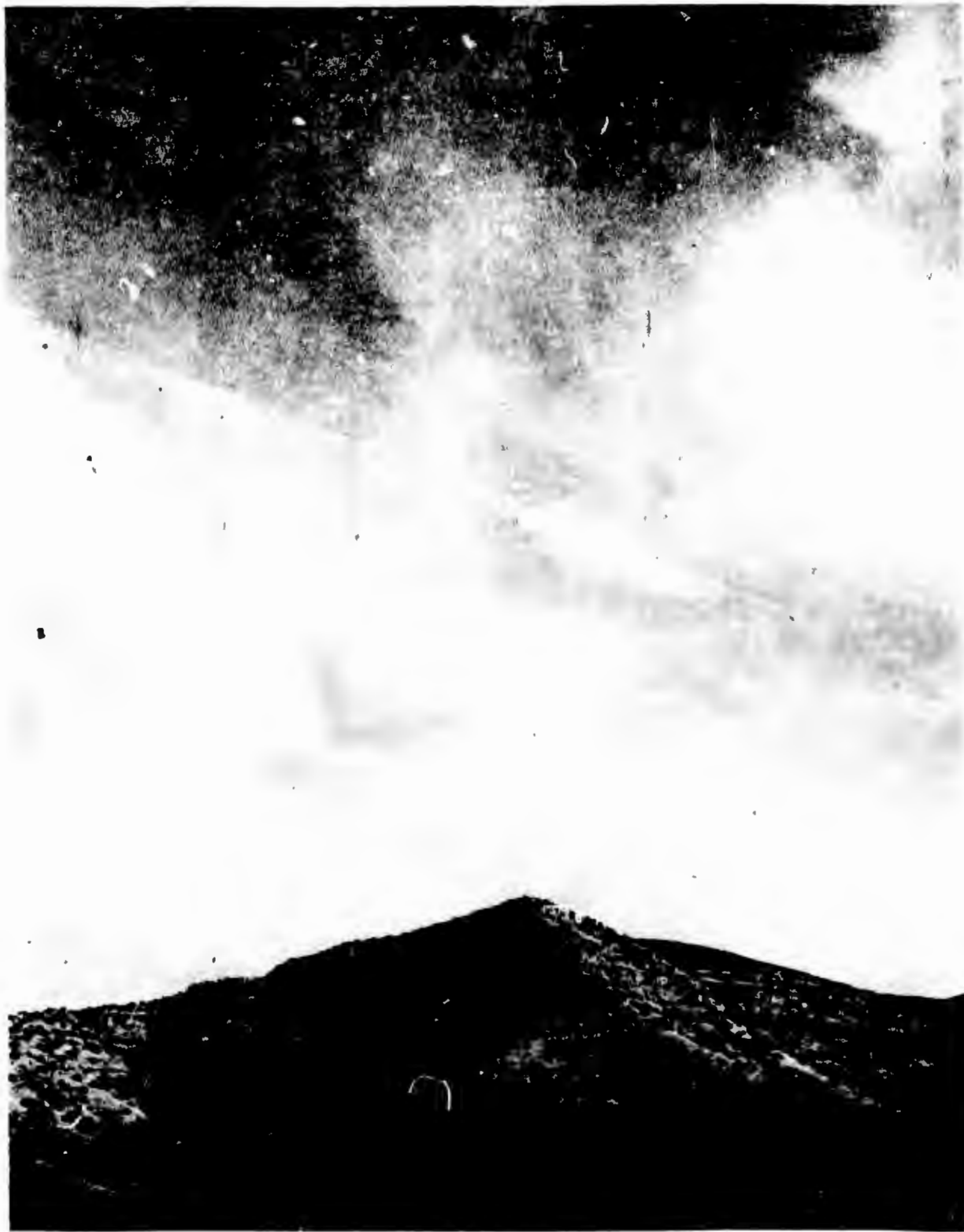


Figure 6. MB-4 4 Seconds after Detonation



Figure 7. MB-4 8 Seconds after Detonation



Figure 8. MB-4 12 Seconds after Detonation



Figure 9. MB-4 Torus 60 Seconds after Detonation



## SECTION III

### CALCULATIONS

#### 1. EARLY CALCULATIONS

Prior to the GEST series a computer simulation of the events was performed using the HULL code. These calculations are described in reference 2. Briefly, however, the calculations involved the following. The SAP code (reference 3) was first used to burn a methane oxygen mixture with the burn being "forced" in that the detonation wave front was advanced at the experimentally determined wave velocity of  $2.75 \times 10^5$  cm/sec. The equation of state used for the unburned methane oxygen mixture was that of an ideal gas with  $\gamma = 1.3986$  and for the burned gas  $\gamma$  was taken to be 1.214. For the equation of state of the surrounding atmosphere the Doan-Nickel equation (reference 4) was used. The burn calculation was carried out until the resulting shock was well into the surrounding air.

The SAP burn output was then used as initial conditions for the HULL code portion of the calculation. The SAP data were inserted into an ambient atmosphere modeled by the U. S. Standard Atmosphere with the balloon center being placed 70 m above the ground in the 2-D cylindrically symmetric HULL mesh.

The chemistry describing the detonation was expressed using the MACE code (reference 5). With thermodynamic parameters of the chemical species of the problem as inputs the equilibrium concentrations were calculated by specifying the pressure and temperature representative of the specific problem.

#### 2. NEW CALCULATIONS

The HULL calculation reported here is similar to that of reference 3 except for the height of burst and the equation of state. For the new calculations the detonation velocity was taken to be  $2.41 \times 10^5$  cm/sec in the SAP burn. The actual site elevation of about 1800 m above sea level was used to determine the atmospheric conditions for the SAP calculation. These conditions were also used to initialize the HULL calculations. This new HULL calculation was placed 43 meters above a reflecting surface rather than 70 m as was the old calculation. Table 3 compares the old and new sets of calculations.

TABLE 3. COMPARISON OF OLD AND NEW GEST CALCULATIONS

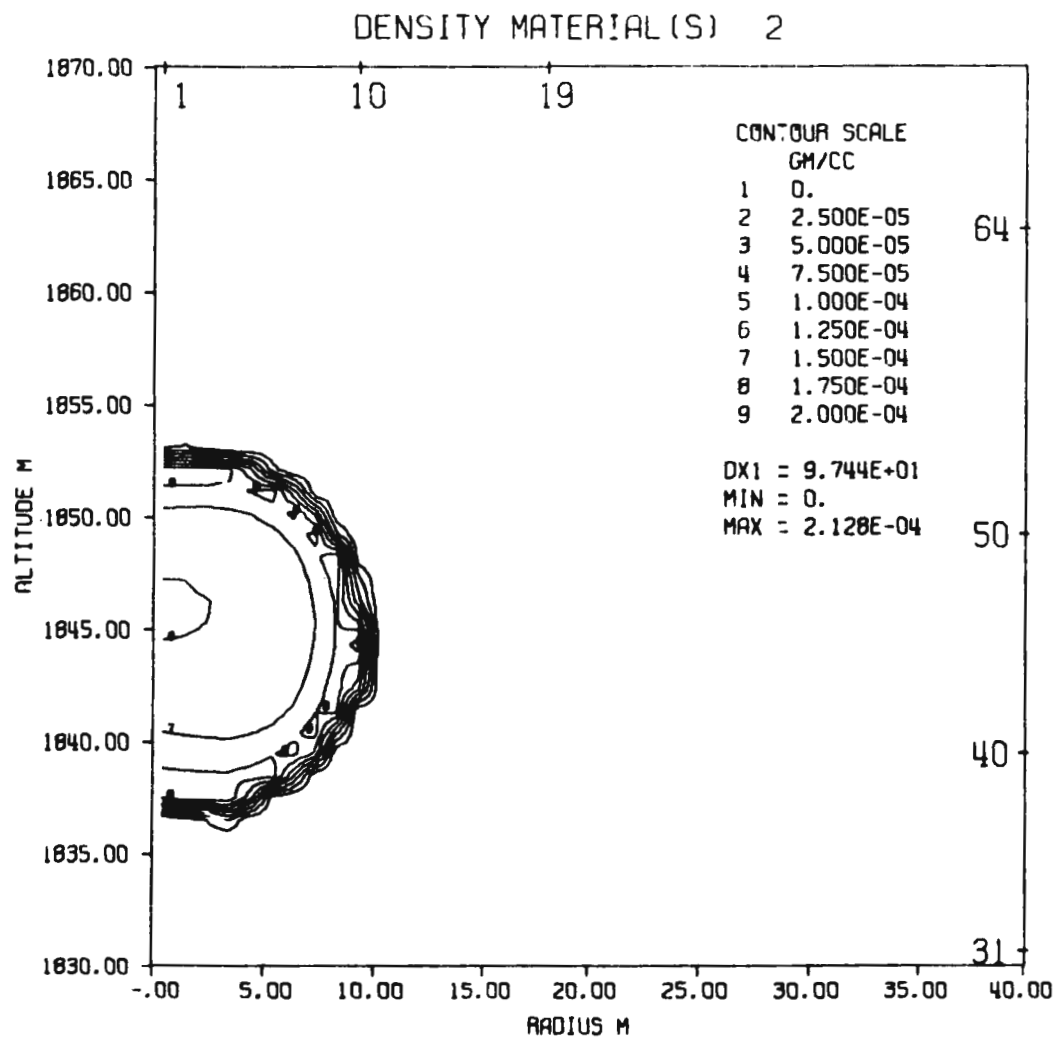
	Original Calculations	Final Calculations
Height of Burst	70 m	43 m
Atmospheric Conditions	STP	Site Conditions
SAP Calculation Burned gas equation of state	$\gamma = \text{Const.}$	$\gamma = \gamma(\rho, E)$
HULL Calculation Equation of State	Air	Air/Burned methane

In order to incorporate the equation of state for burned methane in the HULL calculations, it was necessary to identify those portions of the fluid which were air (material 1) and those which were burned methane (material 2). This multimaterial calculation was run with a "diffusion limiter" which attempts to preserve material gradients. Although these procedures can give rise to spurious flows at material interfaces, they do not affect the total flow in the calculation since only a few cells are affected. The handling of two materials in this fashion affords the opportunity to determine where the detonation products are as a function of time. Figures 10, 11, 12, and 13 are contours in the  $r, z$ -plane of the methane burn products at .5, 1, 2, and 3 seconds, respectively.

The importance of the lower (43 m) height of burst is illustrated by figure 14. This is a plot of rise velocity during the first second. The large rise and fall in velocity at .2 seconds results from the passage of the ground reflected shock through the fireball. Since the shock is stronger for this lower (43 m) HOB than it was for the older calculation (70 m HOB), the cumulative rise and earlier torusing are rather significant.

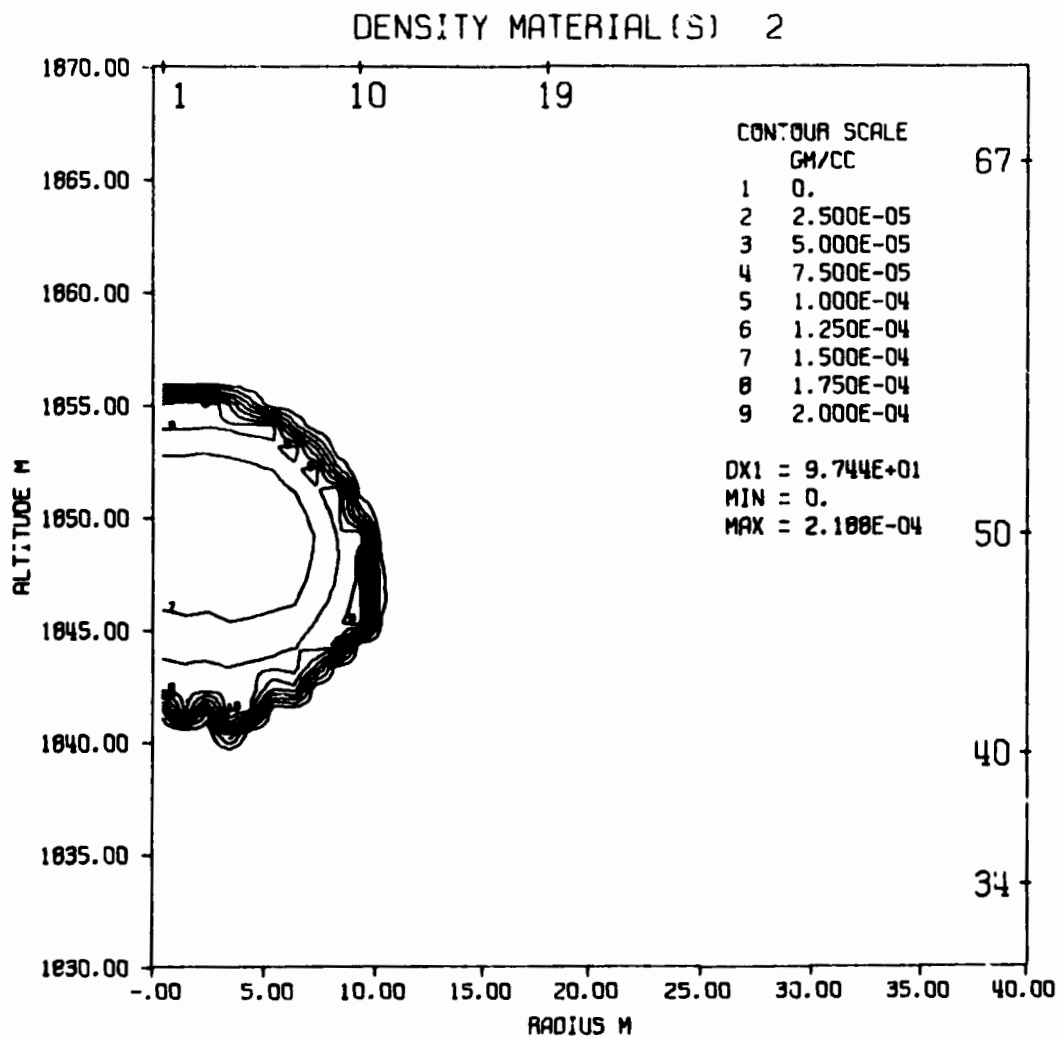
Figures 15, 16, 17 are plots of the altitude, radius and velocity of the fireball over the first 100 seconds. Since no wind profiles are included in the calculation, a large deviation in rise at late times can be expected. This matter will be addressed when the final data reductions are completed.

The most dramatic effect of using the methane burn products equation of state is reflected in the temperature time history (figure 18). The behavior of the burn products is quite different from that of air at a given internal energy and density. The new calculation shows a peak temperature of about



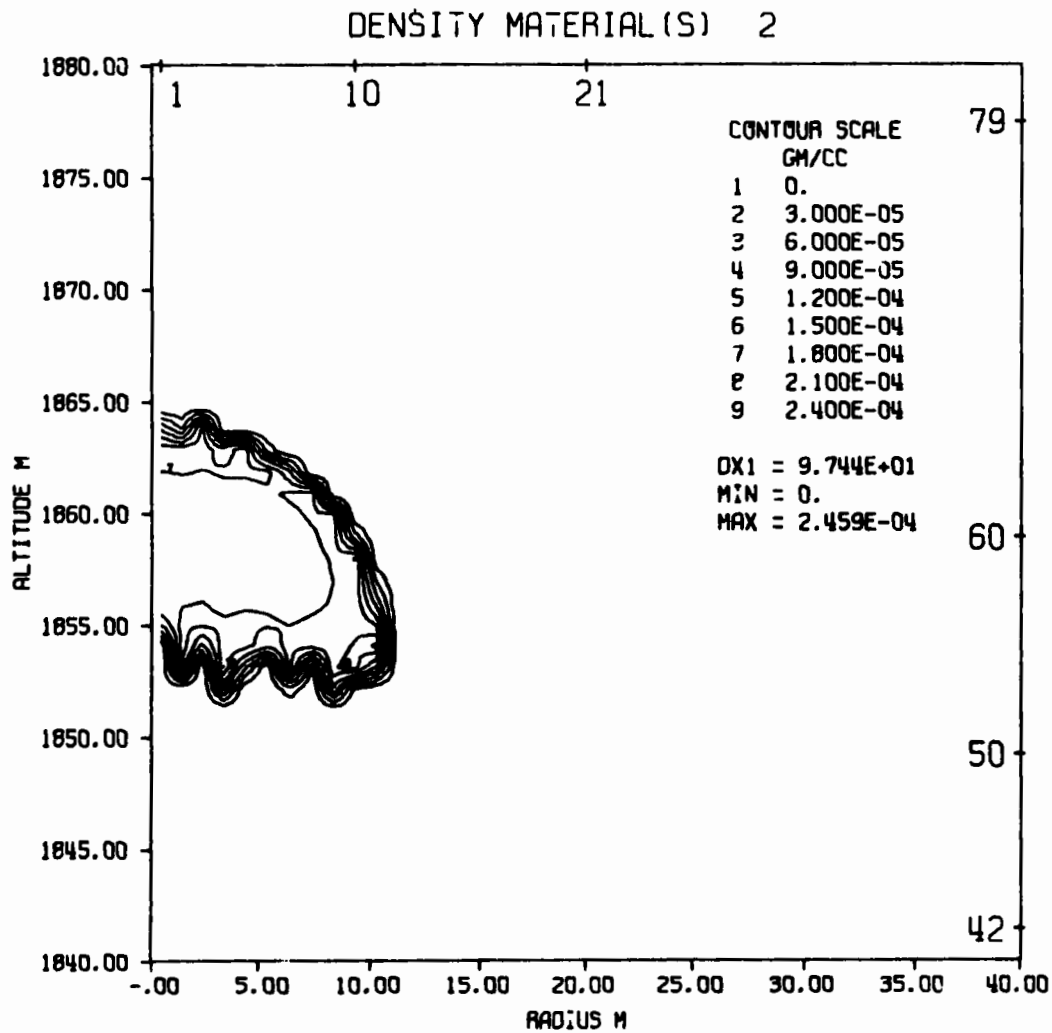
AFWL HULL CALCULATION OF 5 M CH<sub>4</sub> BALLOON AT 13 M SAP INPUT  
TIME 500.000 MSEC CYCLE 1162. PROBLEM 1.0018

**Figure 10. Burned Methane Density Contours at 0.500 Seconds-HULL Calculation**



AFWL HULL CALCULATION OF 5 M CH<sub>4</sub> BALLOON AT 43 M SAP INPUT  
TIME 1.000 SEC CYCLE 2142. PROBLEM 1.0018

**Figure 11. Burned Methane Density Contours at 1.000 Seconds-HULL Calculation**



AFWL HULL CALCULATION OF 5 M CH<sub>4</sub> BALLOON AT 43 M SAP INPUT  
TIME 2.000 SEC CYCLE 4096. PROBLEM 1.0018

Figure 12. Burned Methane Density Contours at 2.000 Seconds-HULL Calculation

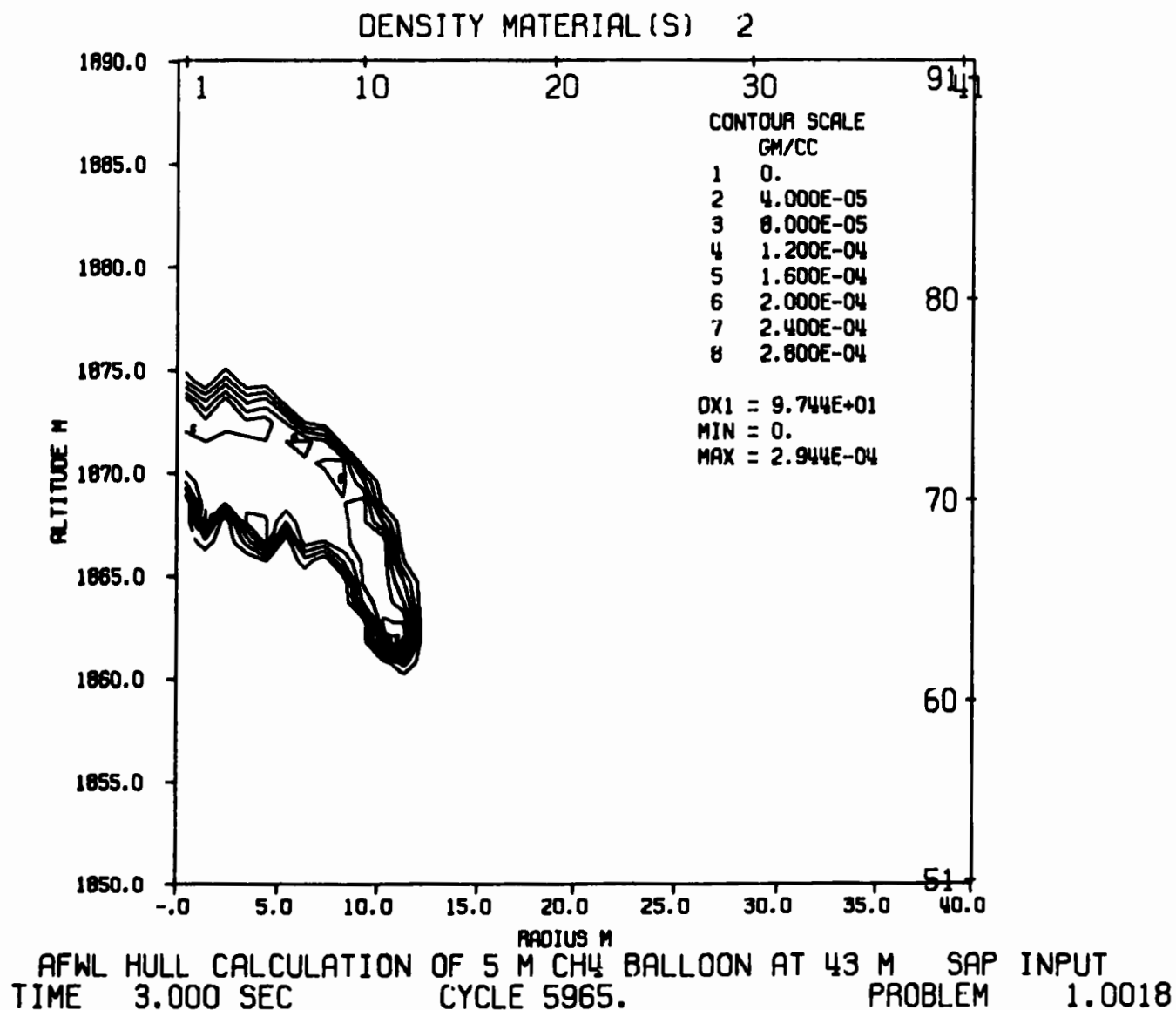
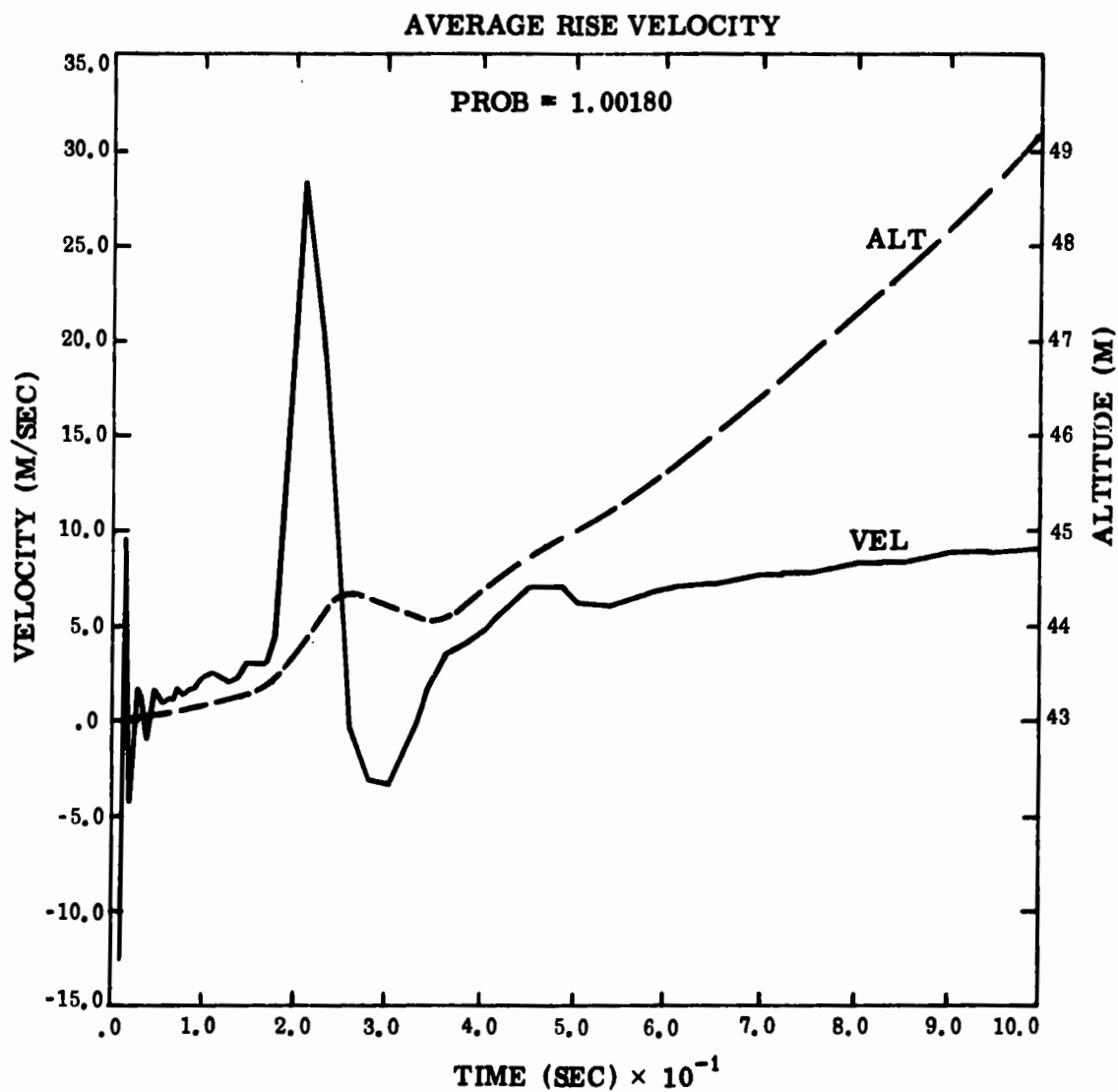
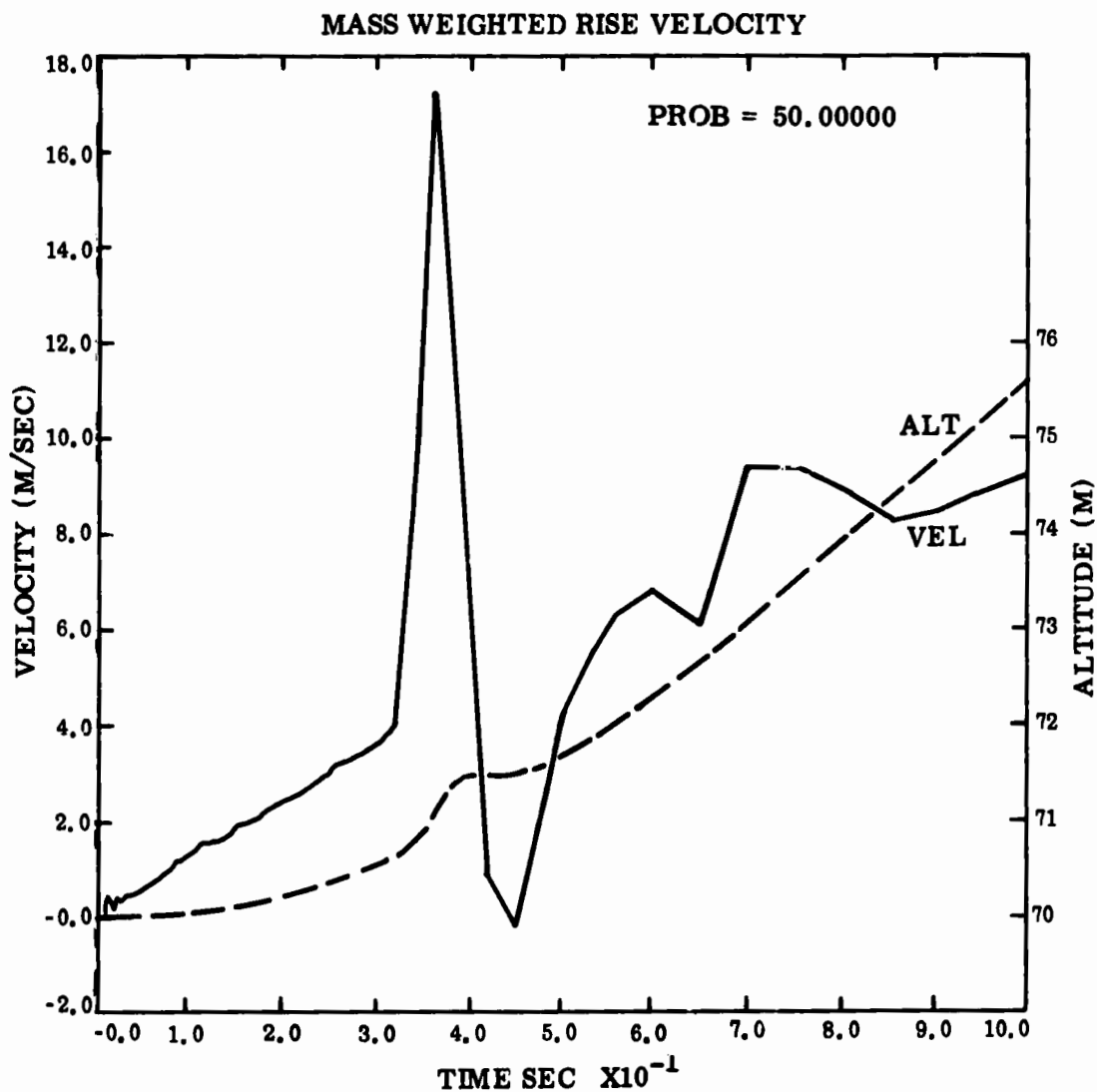


Figure 13. Burned Methane Density Contours at 3.000 Seconds-HULL Calculation



AFWL HULL CALCULATION OF 5M CH4 BALLOON AT 43 M SAP INPUT

Figure 14a. Early Time Rise Velocity and Altitude Versus Time - 43m HULL Calculation.



AFWL HULL CALCULATION OF 5M CH<sub>4</sub> BALLOON AT 70M SAP INPUT 19 OCT 72

Figure 14b. Early Time Rise Velocity and Altitude Versus Time - 70m HULL Calculation.



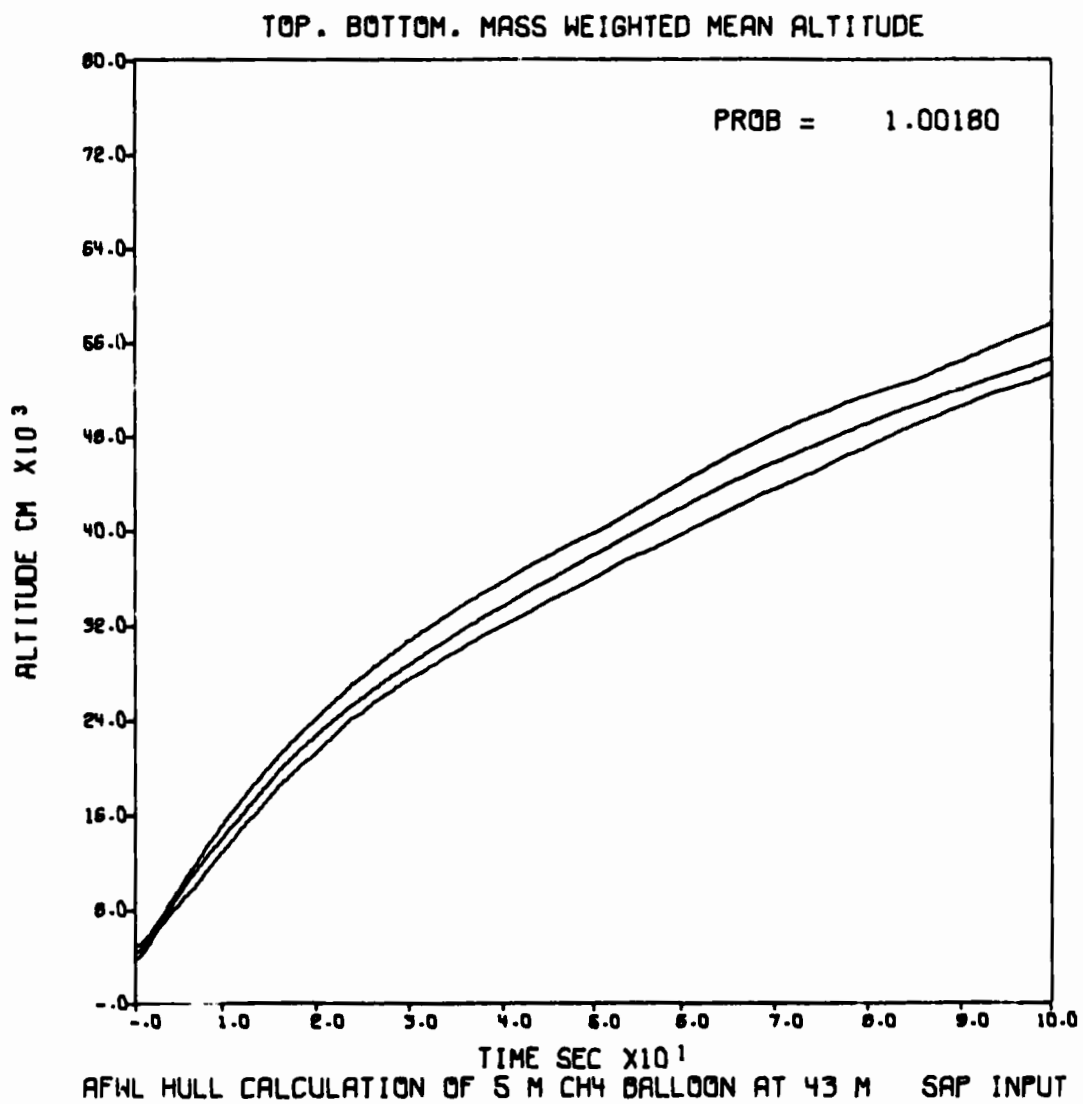


Figure 15. Late Time Altitude versus Time-HULL Calculation

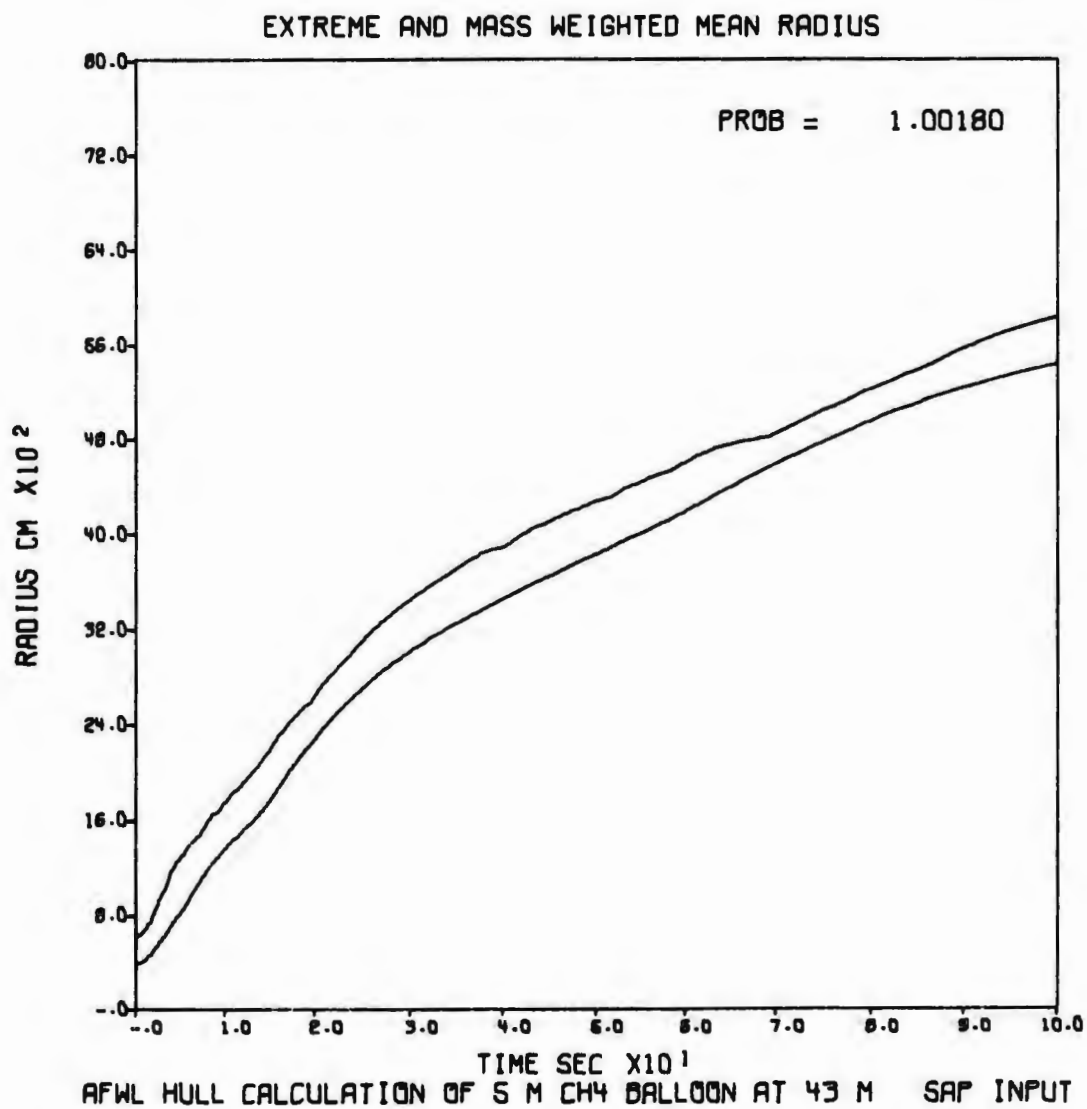


Figure 16. Torus Radius versus Time-HULL Calculation

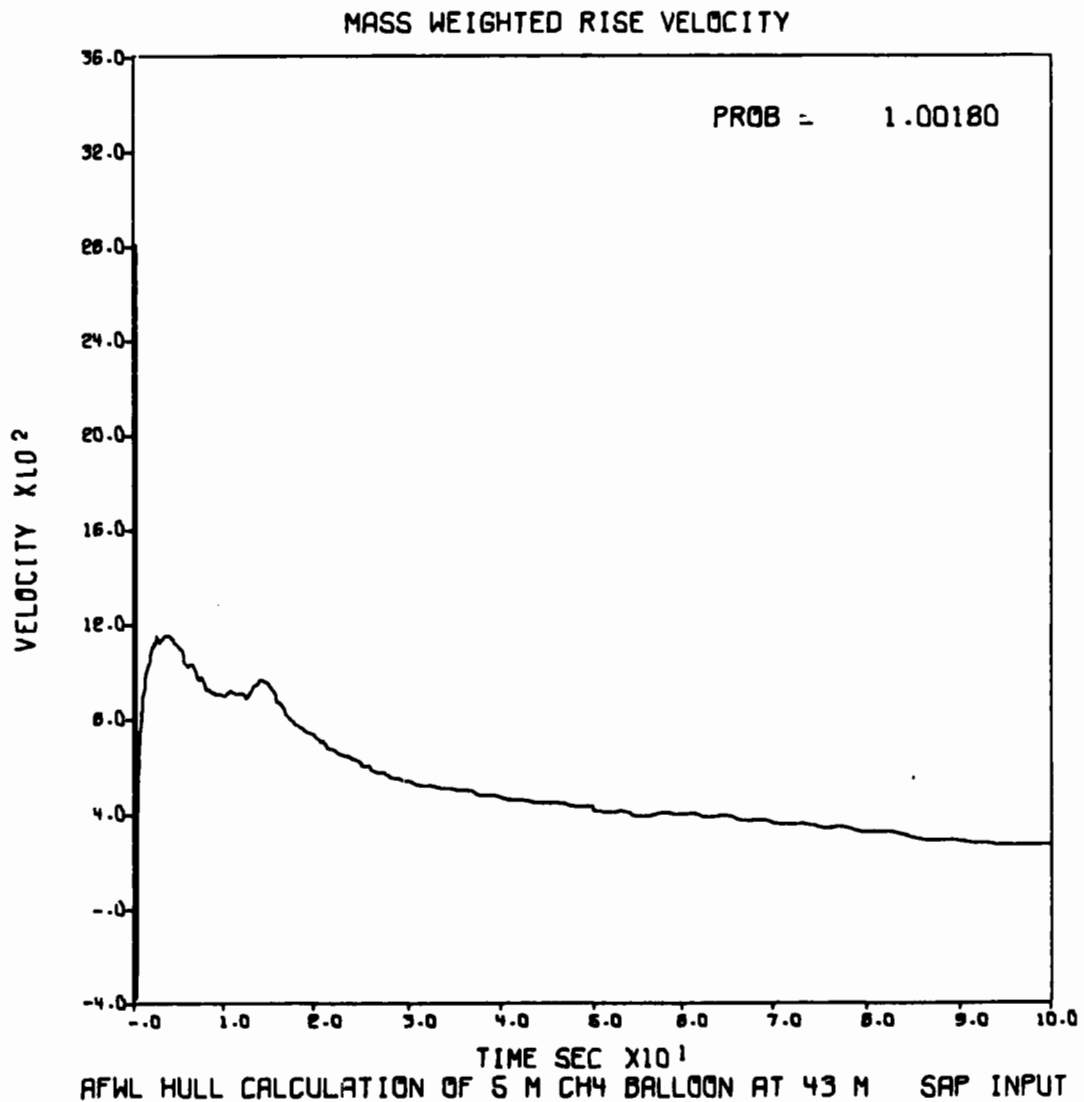


Figure 17. Late Time Rise Velocity versus Time-HULL Calculation

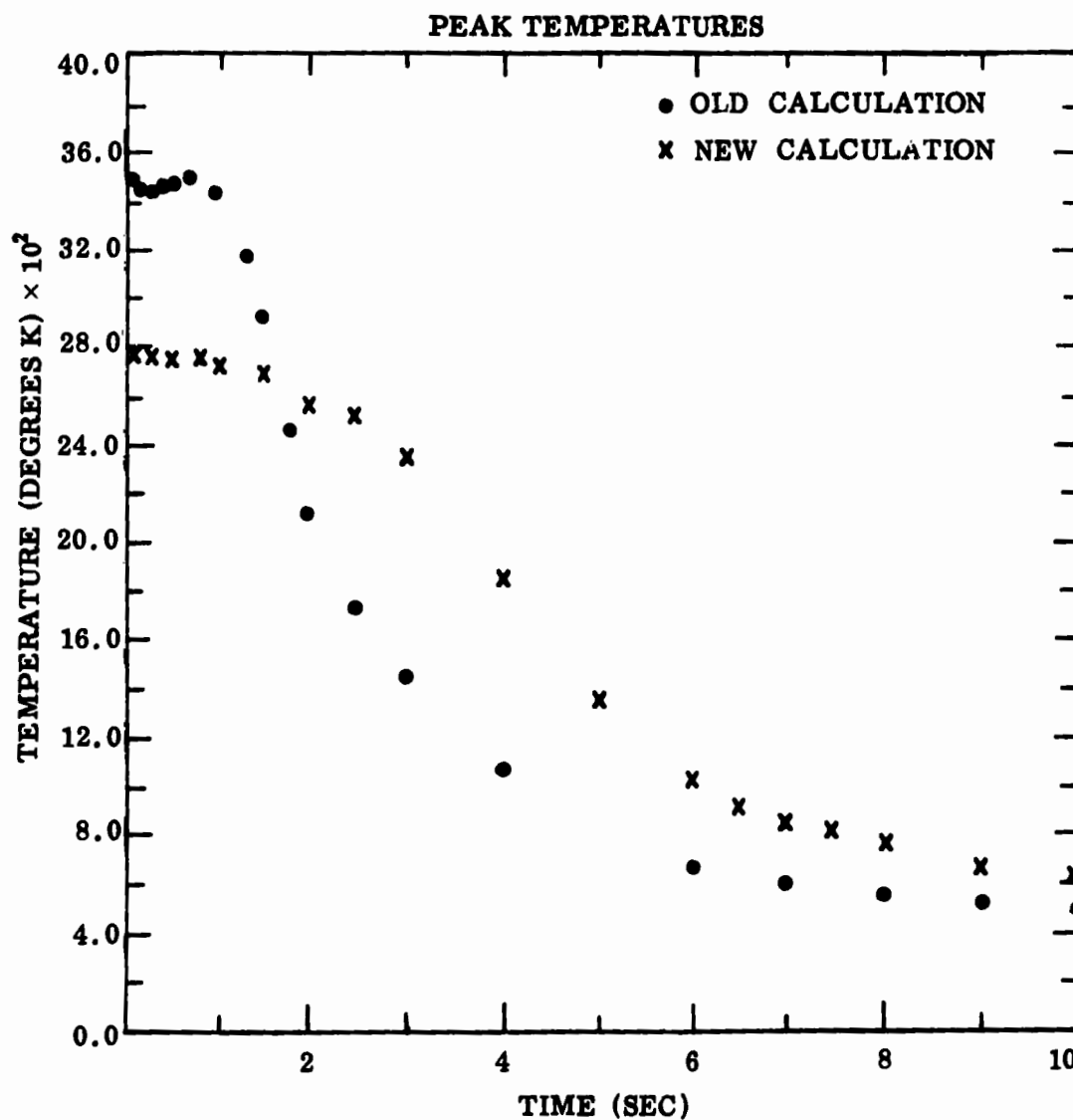


Figure 18. Peak Temperatures versus Time-Old and New HULL Calculations

3100° at burn time and a corresponding slower cooling in time. An important point is that the new temperature calculations are representative of the true temperatures, whereas the earlier ones were not. The effect of the methane equation of state on temperature gradients (figure 19) is not as marked except that, as one would expect, the gradients persist at somewhat higher magnitudes for longer periods of time.

Additional calculations of single material (air) at the 43 m HOB and 2 material (air & burned methane) problems are being done to evaluate the shock torusing effects and to provide more detail in the fireball interior for comparisons with the data. These will be reported separately.

In the new calculations the 1-D equilibrium code ODE (reference 6) was used to obtain equilibrium compositions. This code uses a Newton-Raphson iteration procedure to solve the equations of conservation of mass and energy subject to the relationships describing the state of chemical equilibrium and minimization of total system free energy. The chemical system involved in the calculations may be any combination of ideal gases, solids or liquids.

The ratio of specific heats,  $\gamma$ , for the equation of state, and the specific heat at constant volume,  $C_V$ , were obtained as functions of density ( $\rho$ ) and energy ( $E$ ). To facilitate running the subsequent SAP and HULL calculations the non-linear least squares code VARMIT (reference 7) was used to fit a surface to the data. The surface was expressible in the form

$$\sum_{i,j} a_{ij} \rho^i E^j / \left( 1 + \sum_{k,l} b_{kl} \rho^k E^l \right)$$

Figures 20 & 21 show constant temperature and constant temperature gradient contours, respectively, for  $T + 2.0$  seconds as calculated with the HULL code using the two material equation of state. Superimposed on each of these figures are the hot wire anemometer strut locations. These locations have been adjusted vertically to reflect the fact that the actual height of burst for event MB-4 was 39 m rather than the 43 m for which the computations were run. Figure 22 is included here to illustrate the considerably different temperature contours which results when the equation of state for air (with constant ratio of heat capacities = 1.4) and HOB of 70 m are used in the HULL computations.

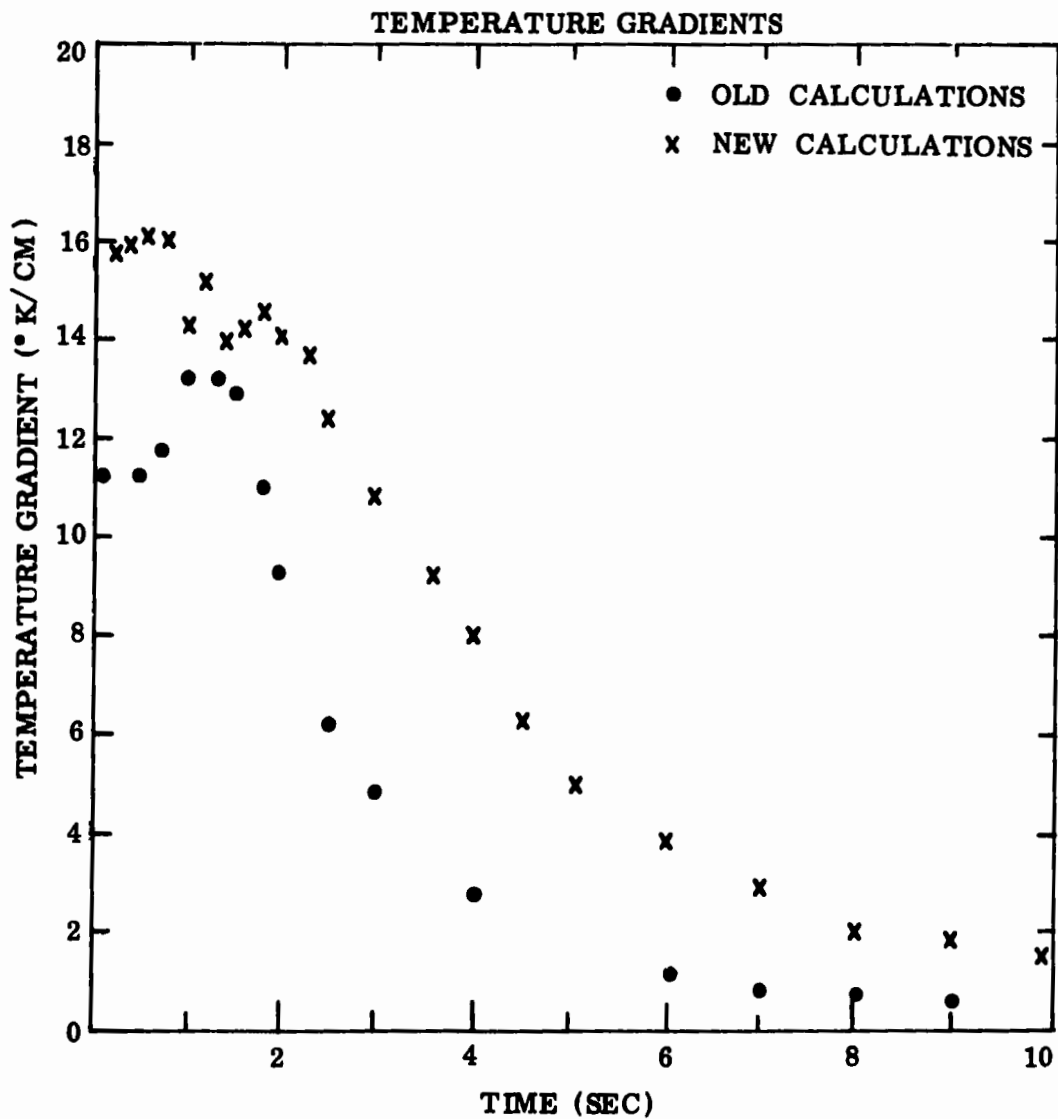
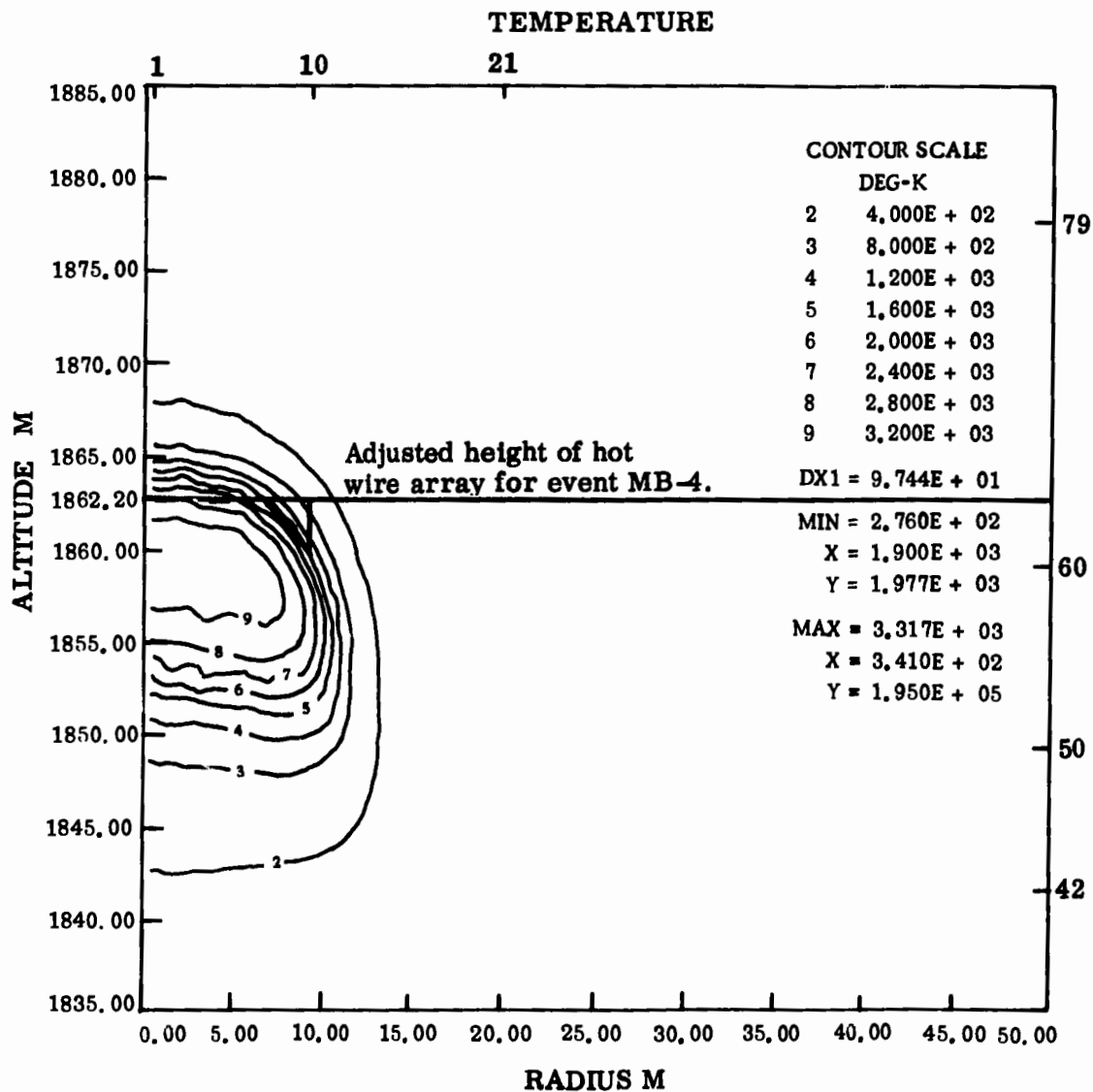
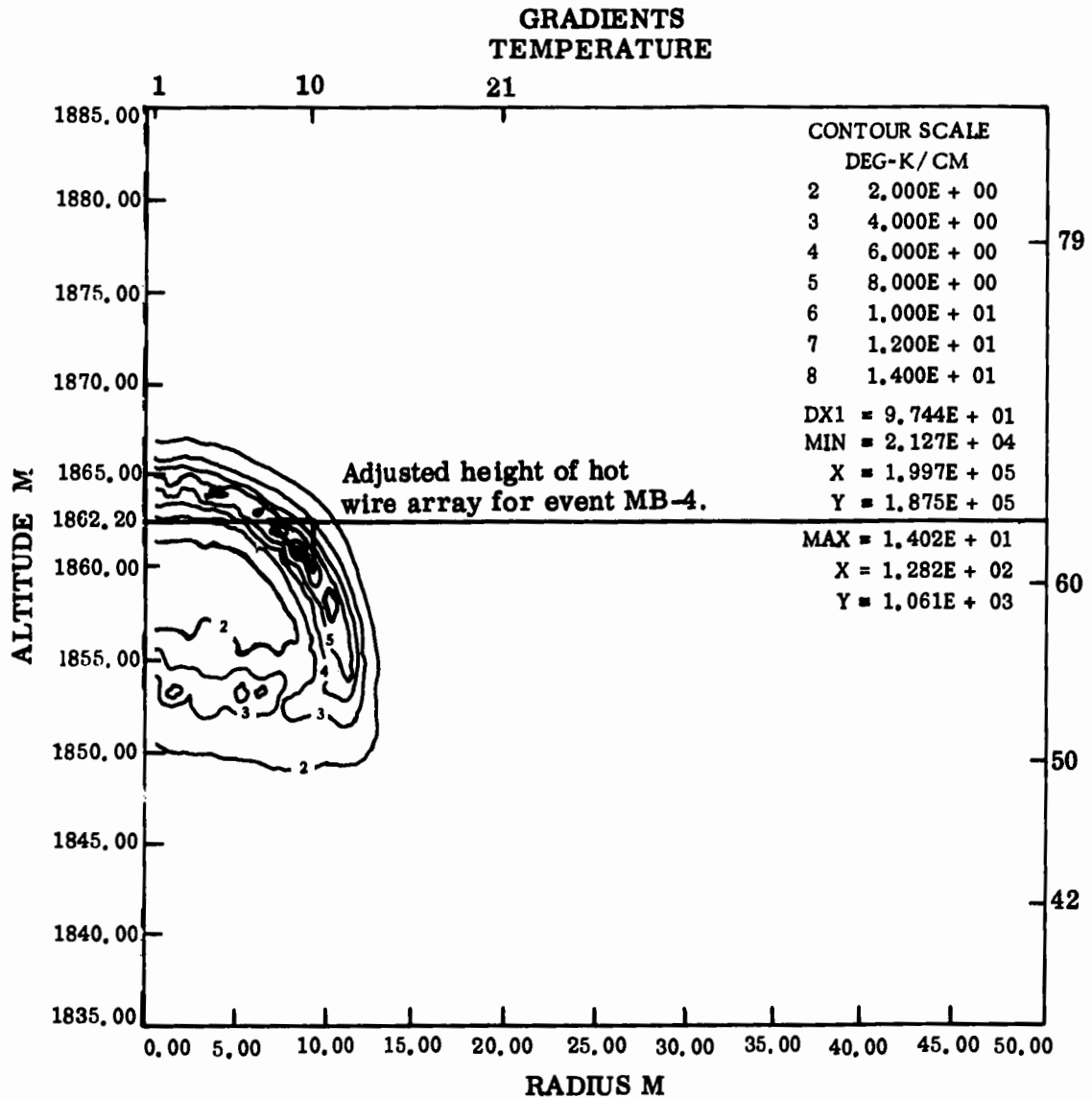


**Figure 19. Temperature Gradients versus Time-Old and New HULL Calculations**



AFWL HULL CALCULATION OF 5 M CH4 BALLOON AT 43 M SAP INPUT  
TIME 2.000 SEC      CYCLE 4096.      PROBLEM 1.0018

Figure 20. Constant Temperature Contours at 2.000 Seconds-HULL Calculations



AFWL HULL CALCULATION OF 5 M CH<sub>4</sub> BALLOON AT 43 M SAP INPUT  
 TIME 2.000 SEC                      CYCLE 4096.                      PROBLEM 1.0018

Figure 21. Constant Temperature Gradient Contours at 2.000 Seconds-HULL Calculations



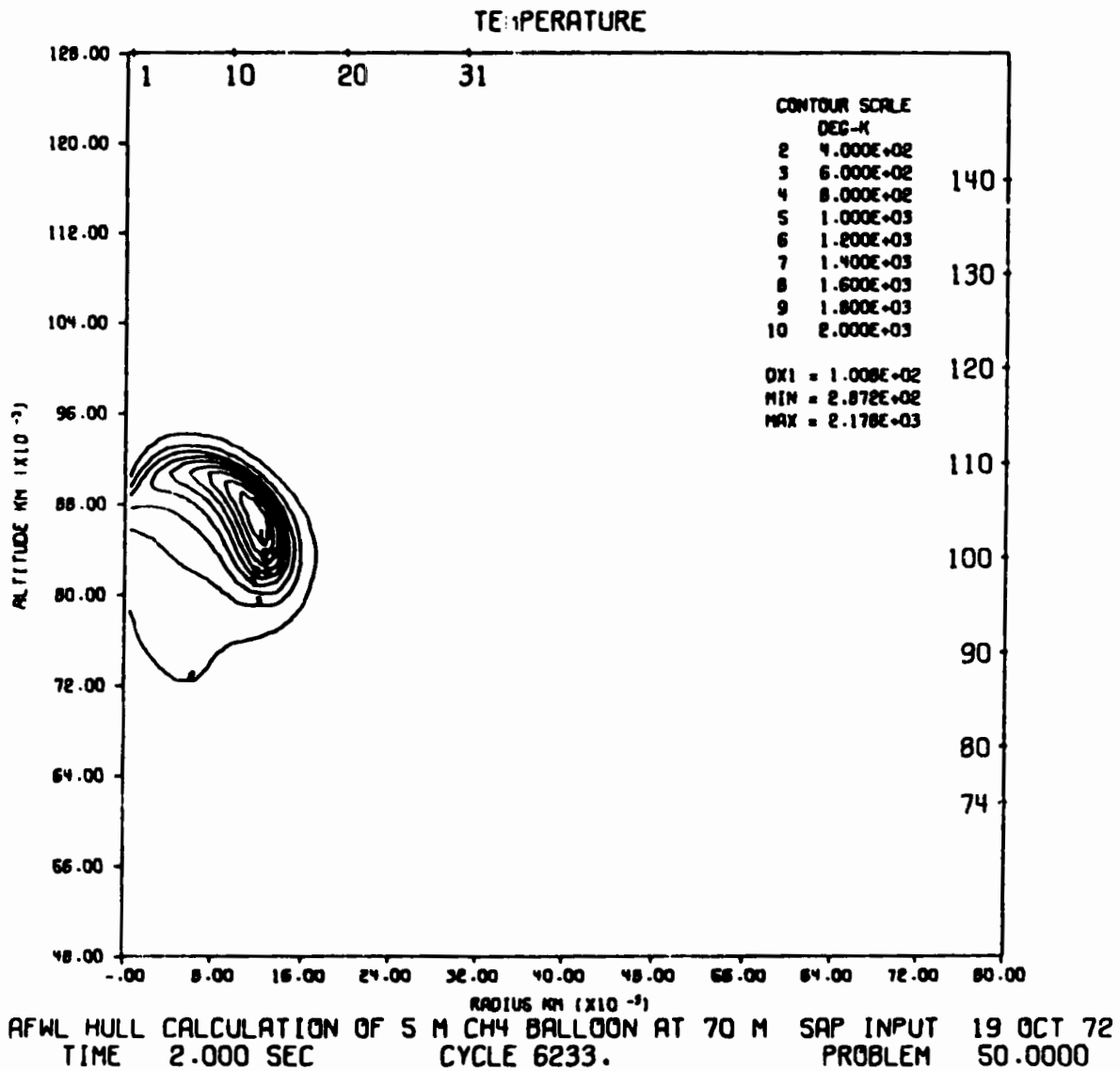


Figure 22. Constant Temperature Contours at 2.000 Seconds-Old HULL Calculations

## SECTION IV

### INDIVIDUAL EXPERIMENTS

In addition to the air blast pressure and time of arrival measurements carried out by AFWL/DEX several experimental measurement programs were carried out by groups external to the AFWL. These programs used or intended to use infrared (IR) diagnostics, and hot-wire anemometry to examine fireball temperatures and species concentrations, turbulence effects on species concentrations and on temperatures and velocities. These individual experiments and certain preliminary findings are presented below. Where they were available, preliminary reports by the individual investigators serve as basis for the material presented.

1. TEMPERATURE MEASUREMENTS  
(Los Alamos Scientific Laboratories - Reference 13)

IR measurements of the fireball and torus were made by LASL during several of the GEST events. Fireball temperatures could be deduced from these measurements. Figures 23 and 24 give the temperatures determined for events MB-1 and MB-2. The device used was an AGA thermovision camera. The camera scans the field of view and focuses the infrared radiation on a detector which converts the IR signal to an electrical signal. This electrical signal is then amplified and used to control the electron beam of a TV monitor tube, thereby showing the thermal distribution.

SAGA is a short wavelength AGA. It uses an indium-antimonide detector with sensitivity in the  $4.5 - 5.5 \mu$  region. LAGA is a long wavelength AGA with its main sensitivity in the  $9.2 - 11.7 \mu$  region; however, it also has windows at  $3.5$  and  $2.1 \mu$ . LAGA uses a mercury-cadmium-telluride detector.

The background brightness temperature lines were derived by assuming that the blank sky which served as backdrop for the GEST events was a solid blackbody radiator. From the AGA device output when pointed at the sky the equivalent blackbody temperature was calculated.

In the calculations, allowance was made for atmospheric attenuation. However, no allowance was made for (1) less than unity emissivities, (2) transient cloud transparencies, or (3) masking of the hottest regions by optically thick outer regions of the cloud. All of these would tend to raise the calculated temperatures.

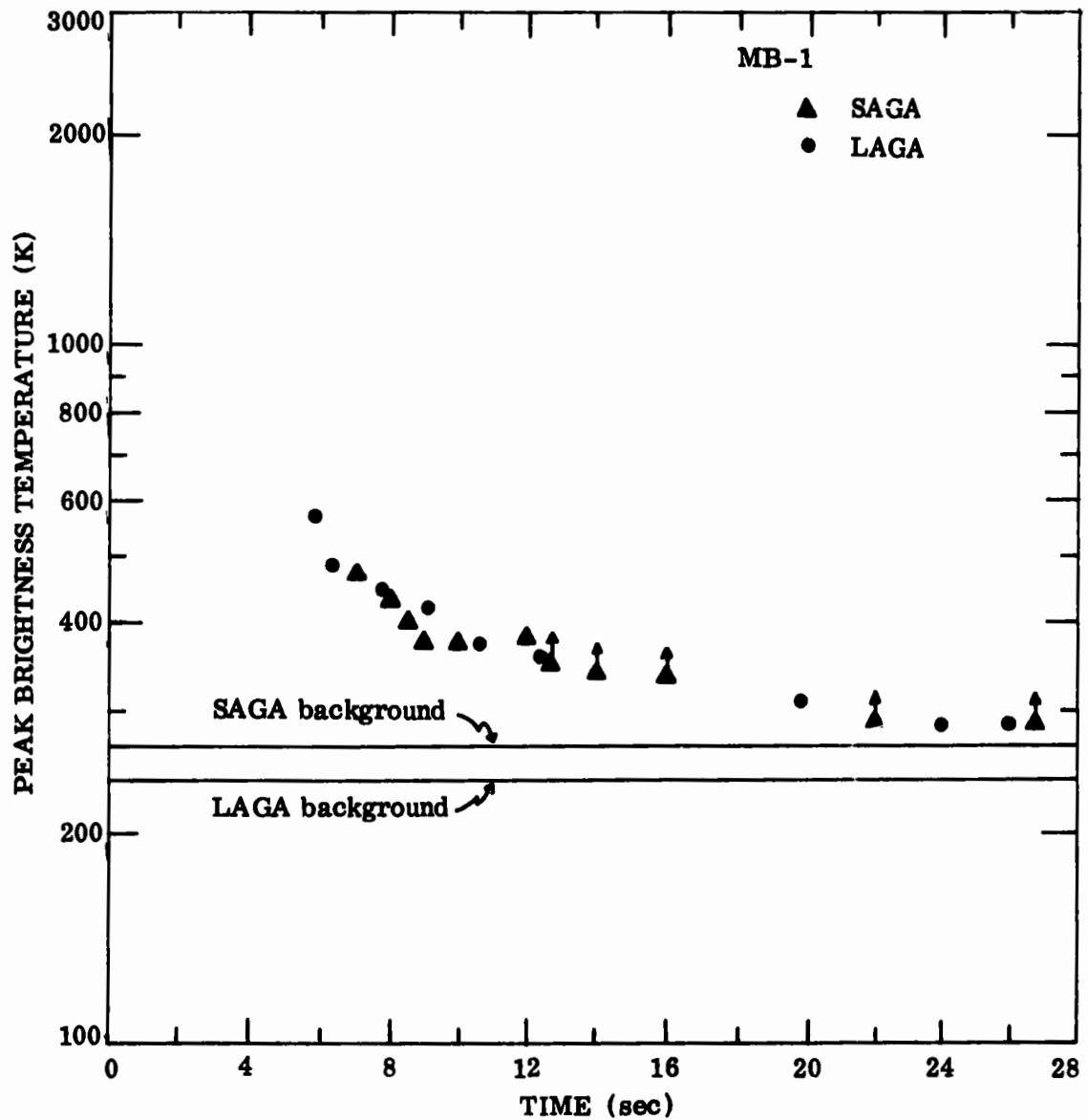


Figure 23. Peak Brightness Temperature versus Time-LASL AGA Measurements-Event MB-1

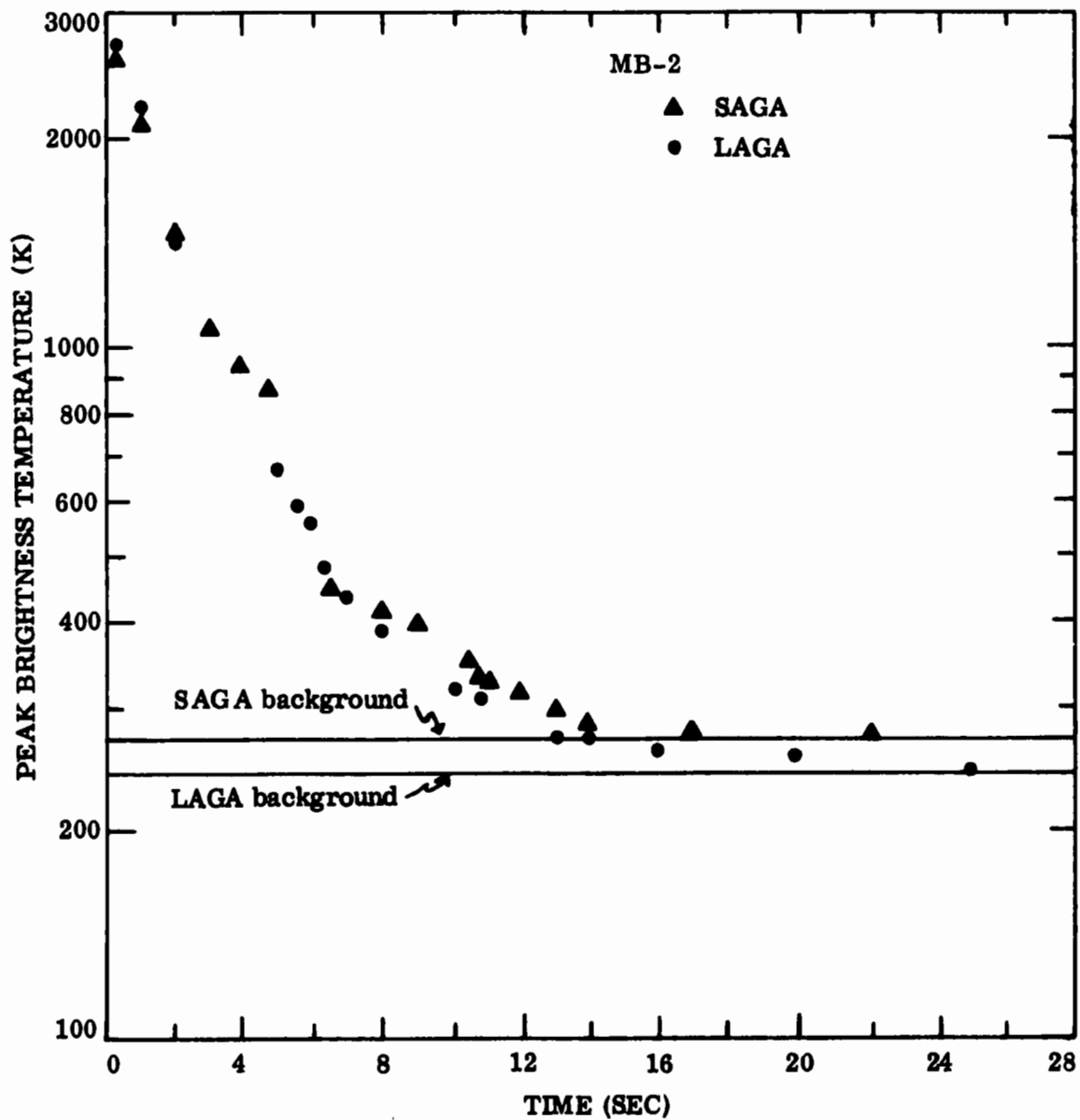


Figure 24. Peak Brightness Temperature versus Time-LASL AGA Measurements-Event MB-2

2. MEASUREMENTS OF INFRARED SPECTRA IN THE RANGE 1.56 to 4.67 MICRONS  
(Utah State University and Cambridge Research Laboratories - Reference 14)

Infrared spectral measurements of the five GEST events were made with a rapid scanning Michelson interferometer specially constructed, by Block Engineering, to AFCRL and USU specifications. The interferometer was coaligned with both a super 8 mm camera and a fixed spectral bandwidth radiometer, hand tracked on the target through a sighting telescope. The 8 mm camera confirmed tracking of the instruments, while the radiometer gave an absolute calibration check for the interferometer and also provided absolute emission levels in a specified bandwidth. Thermal pulse radiometers were also used for the final GEST explosion to give early time information. The ground range of the instrumentation was 3425 feet from ground zero in all cases.

The data from the interferometer is summarized in this report. The typical results which are presented are only a small portion of the extensive data obtained. These preliminary versions of the absolutely calibrated infrared spectra obtained with  $4\text{ cm}^{-1}$  resolution in the  $2140$  to  $6400\text{ cm}^{-1}$  (4.67-1.56 microns) region are subject to what will probably be small corrections arising from more detailed calibrations of the neutral density filters. Comparisons (not given here) between the interferometer and radiometer intensities confirm the absolute levels given in the interferometer data.

Each spectrum presented is the result of a single scan of the interferometer. Because the interferometer operates at a rate of 14 scans per second, each scan reduces to a spectrum which is the spectral irradiance integrated over a time interval of approximately 0.07 second. Since the instrument field of view was  $4.5^\circ$  (determined by its 50% response points), all the radiation from the fireball and debris cloud was included in the measurements.

In the data that follow, the calibrated spectral irradiance at the interferometer entrance aperture was determined in absolute units ( $\text{watts}\cdot\text{cm}^{-2}\cdot\text{wavenumber}^{-1}$ ) by employing field and laboratory calibrations with black body sources. In addition, for some of the data, temperature, pressure, and dew point measurements made at the test site were used as inputs to atmospheric transmission models (reference 8) to determine the test configuration atmospheric transmission. This transmission was used to convert from spectral irradiance values to absolute spectral radiant intensities ( $\text{watts}\cdot\text{steradian}^{-1}\cdot\text{wavenumber}^{-1}$ ) of the source. All of the data has background radiation

subtracted out, and the contribution of sunlight reflected from the fireball and debris cloud appears to be negligible.

In figure 25, the spectral irradiance of the double balloon explosion DMB-1 is shown at 0.2 seconds after ignition. The sharp dip at wavenumbers between 2200 and 2400  $\text{cm}^{-1}$  is due to atmospheric absorption by  $\text{CO}_2$ . The large dips between 3500 and 4000  $\text{cm}^{-1}$  are due to absorption by atmospheric water. The irradiance at that time is at least three orders of magnitude above background. The very noisy wings at wave numbers below 2200  $\text{cm}^{-1}$  and above 6000  $\text{cm}^{-1}$  arise because the interferometer spectral response had dropped to such a low value in those regions that the signal was primarily instrument noise. Currently the spectrum is interpreted to be that of radiation from hot  $\text{H}_2\text{O}$  bands centered near 1600, 3700 and 6250  $\text{cm}^{-1}$  (6.3, 2.7 and 1.6 microns).

In figure 26, the spectral irradiance from DMB-1 is shown at 1.59 seconds after ignition. The temperature of the radiating water has dropped significantly, causing the radiation to concentrate at the band centers. In the 2200 to 2400  $\text{cm}^{-1}$  region, hot  $\text{CO}_2$  emission from the 2300  $\text{cm}^{-1}$  (4.3 micron) band is now observable as it is transmitted through the sides of the atmospheric  $\text{CO}_2$  absorption band.

In figure 27, the spectrum from DMB-1 is shown 3.27 seconds after ignition. The water bands have cooled further and the  $\text{CO}_2$  radiation is now very prominent, decaying at a much slower rate than that from the water. The  $\text{CO}_2$  band irradiance peaks are off scale and appear as a weaker second trace at half scale in the 2140 to 2800  $\text{cm}^{-1}$  region.

The spectrum of DMB-1 is shown at 7.54 seconds after ignition in figure 28. A small amount of radiation from the 3700  $\text{cm}^{-1}$  (2.7 micron)  $\text{H}_2\text{O}$  band is still observable, and the  $\text{CO}_2$  band is still very prominent.

The overall time variation of the spectral irradiance at seven selected wavelengths in the spectrum is shown in figure 29. To aid in the interpretation of this figure, curves have been sketched through four of the seven sets of points. At times where points are missing, the data is not available because selective optical filters for other measurement requirements were being used.

In figures 30 and 31, the spectral irradiance observed from MB-3, the third single balloon explosion, is shown at 0.11 and 5.15 seconds after ignition. These spectra are very similar to those already described from DMB-1. In fact, all of the methane-oxygen balloon explosions exhibited similar behavior.

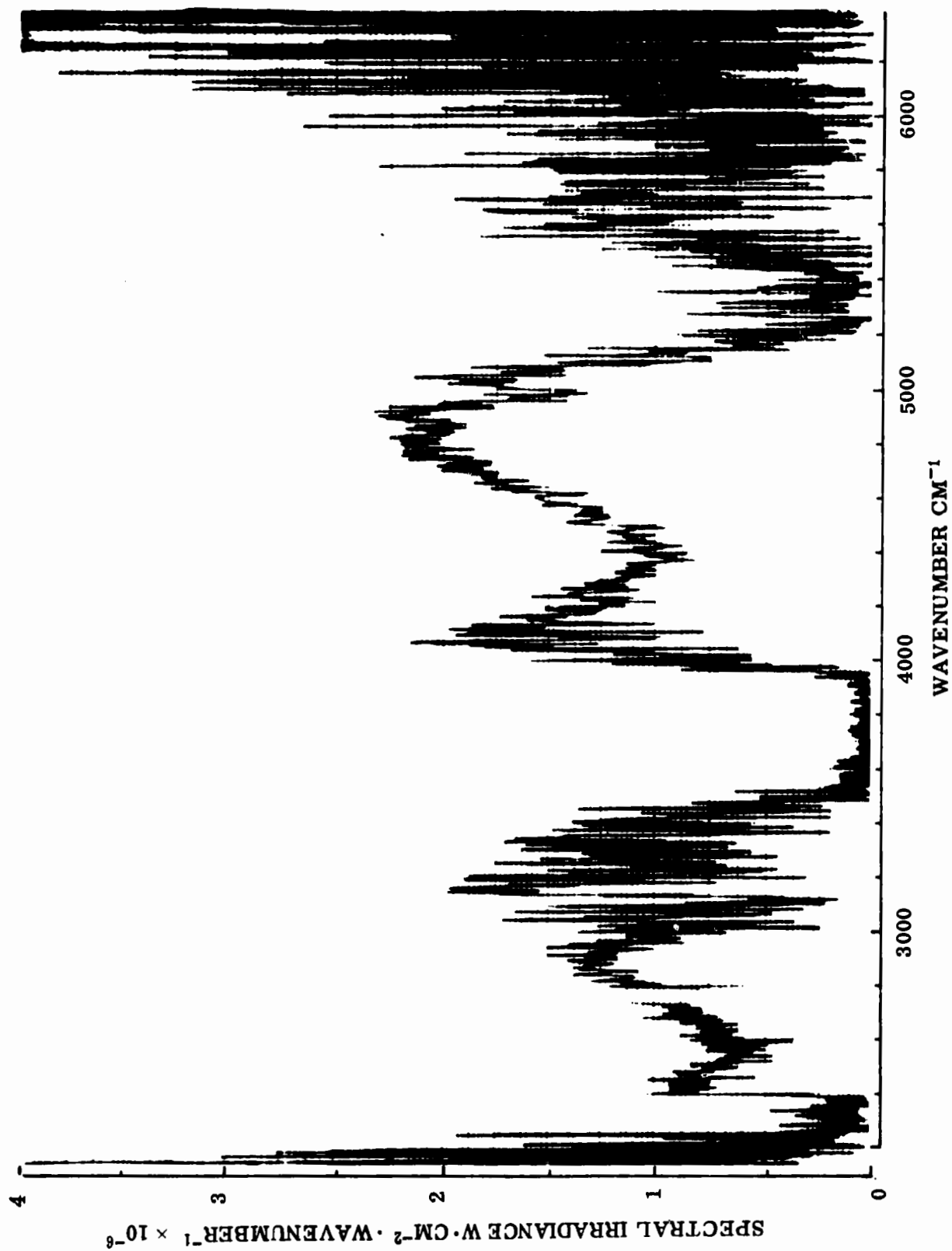


Figure 25. Spectral Irradiance for Event DMB-1 at 0.20 Seconds



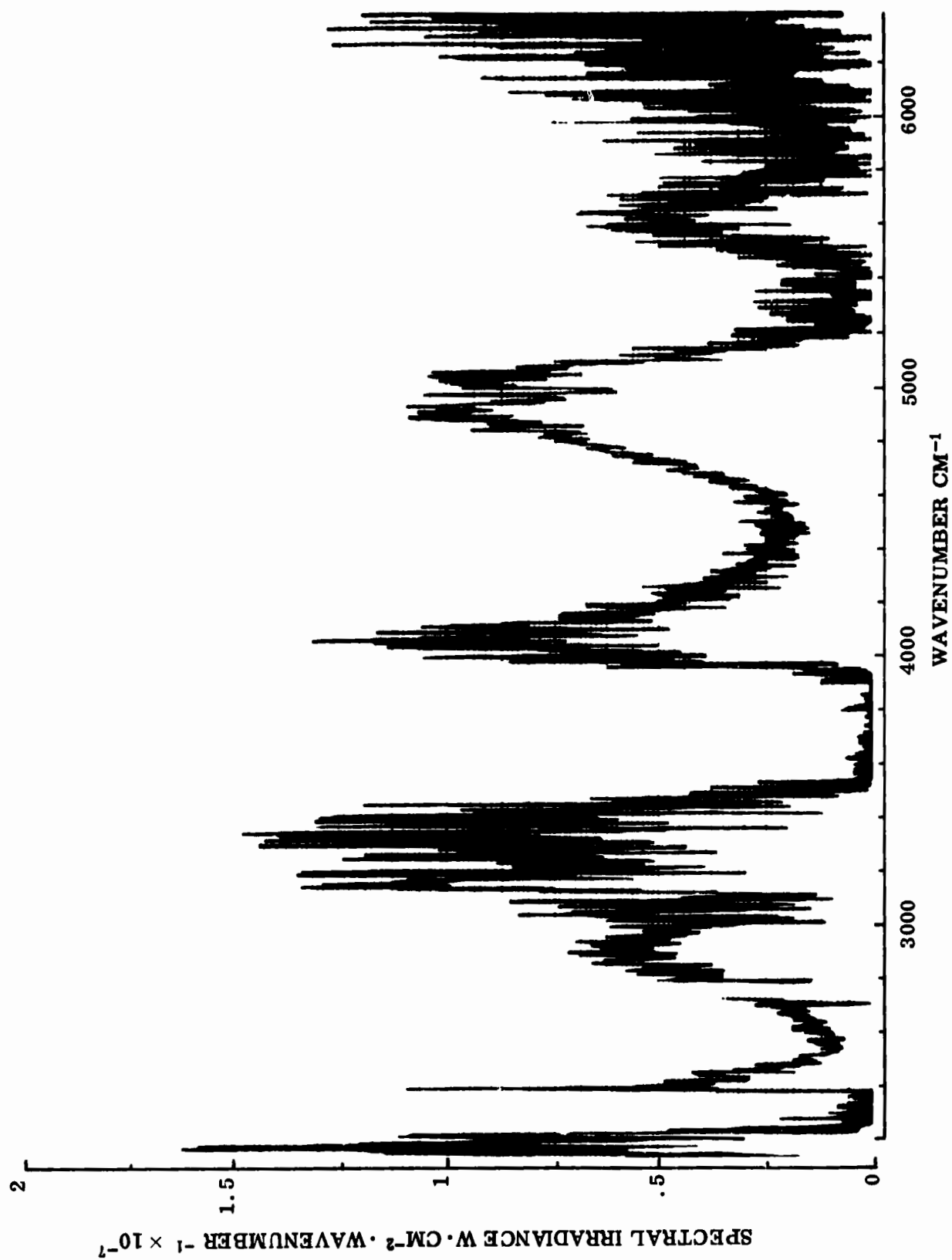


Figure 26. Spectral Irradiance for Event DMB-1 at 1.59 Seconds

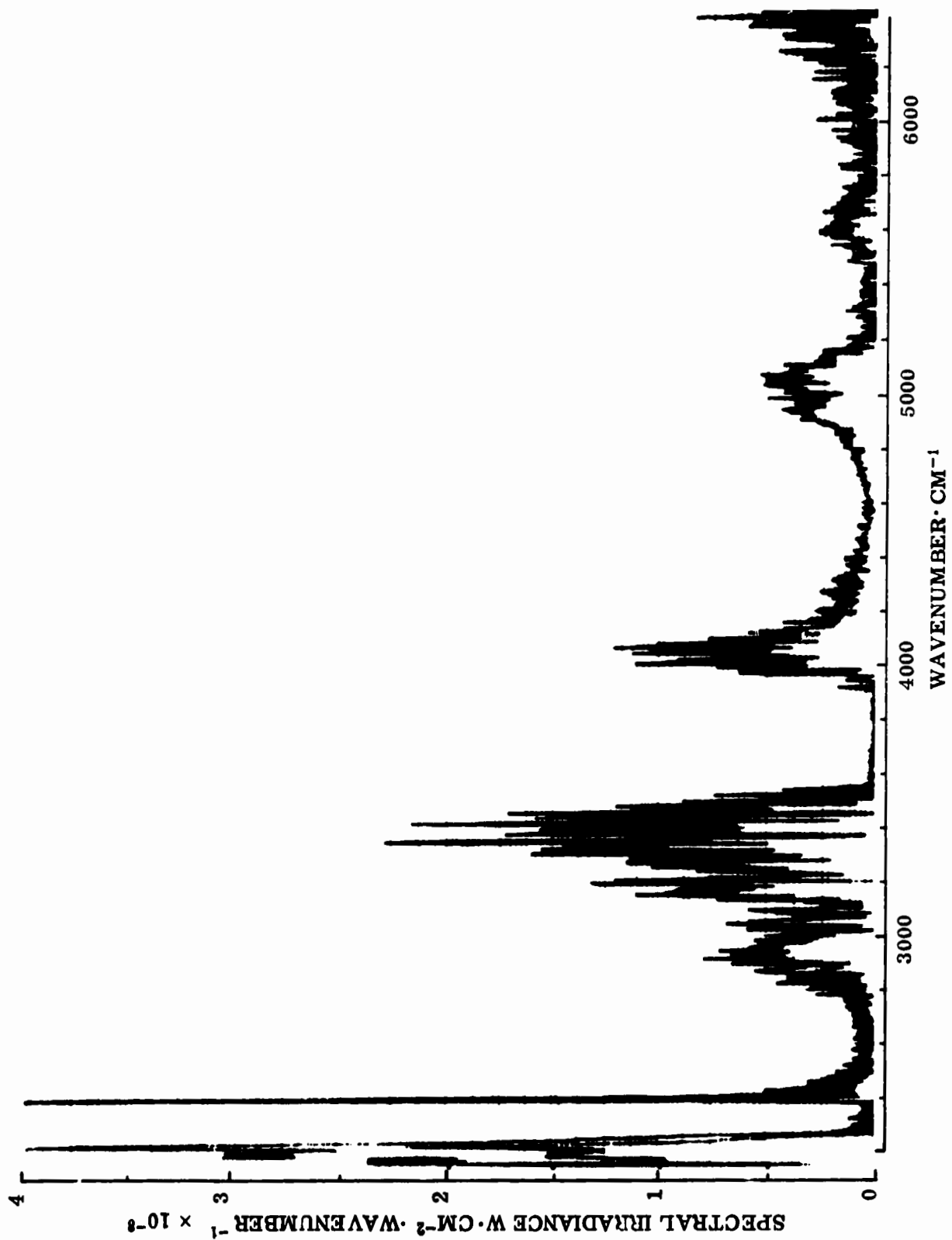


Figure 27. Spectral Irradiance for Event DMB-1 at 3.27 Seconds



Figure 28. Spectral Irradiance for Event DMB-1 at 7.54 Seconds

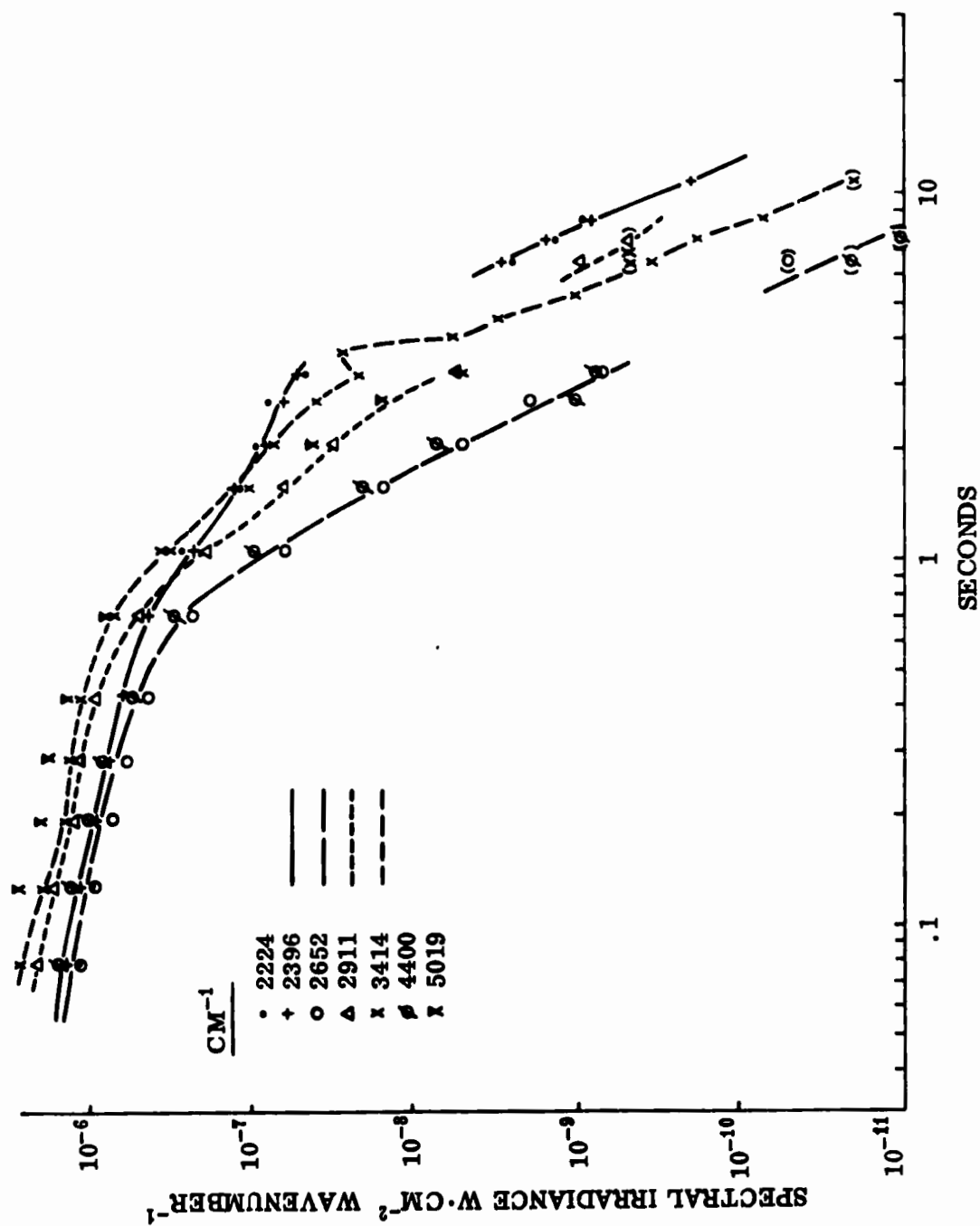


Figure 29. Spectral Irradiance versus Time for Event DMB-1

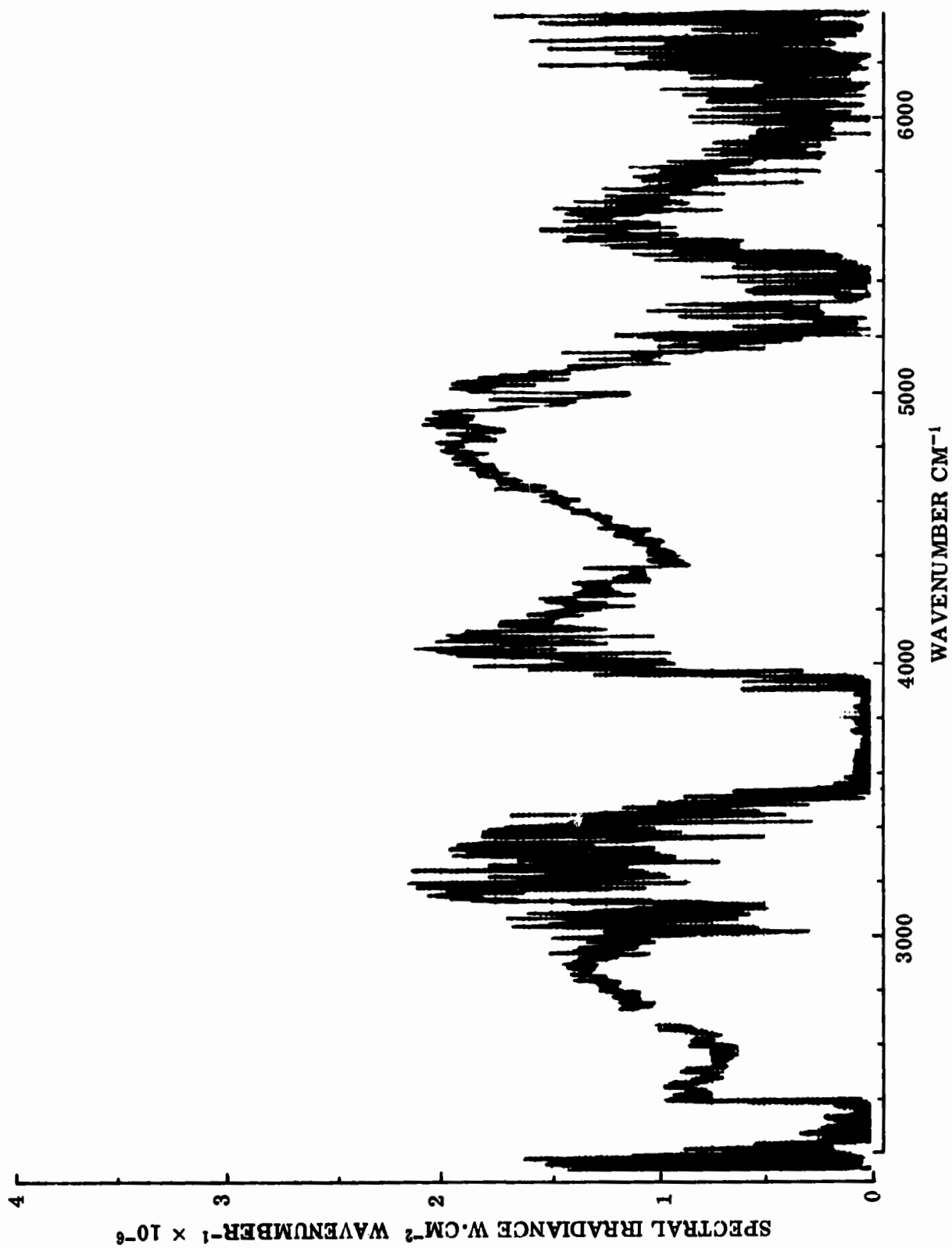


Figure 30. Spectral Irradiance for Event MB-3 at 0.11 Seconds

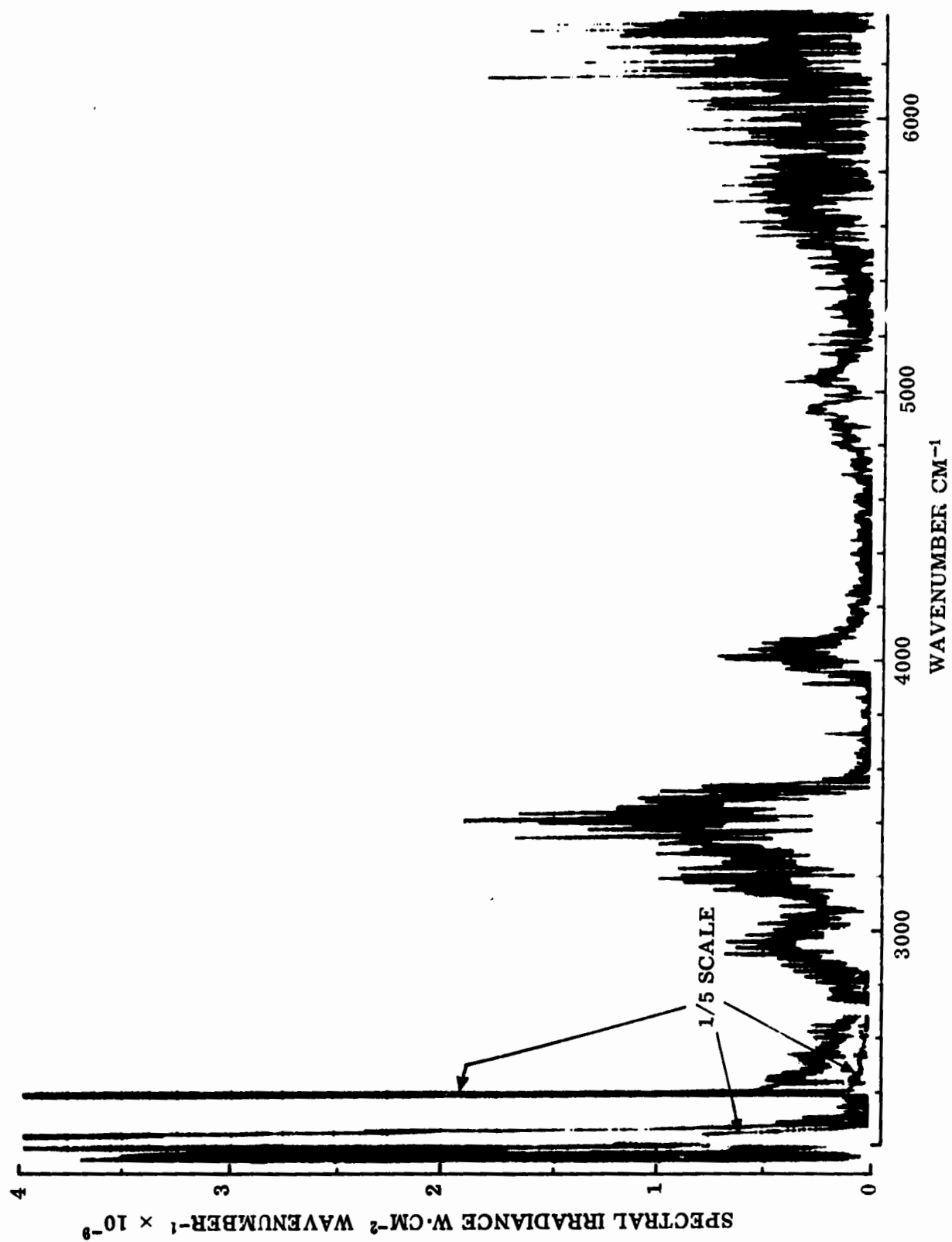


Figure 31. Spectral Irradiance for Event MB-3 at 5.15 Seconds

The time variations of the same seven spectral elements displayed in figure 29 for DMB-1 are shown in figure 32 for MB-3. Again, the behaviors of DMB-1 and MB-3 irradiances appear very similar. Although DMB-1 was a double shot, its irradiance was not significantly greater than that observed from MB-3 because of atmospheric attenuation in the water bands. This was due to the fact that there was twice as much water in the atmosphere when DMB-1 was fired (water density was 7.3 g/m at 830 mb and 4.0°C for DMB-1 as compared to 3.4 g/m at 830 mb and 5.0°C for MB-3). Also, since one of the balloons on DMB-1 was not completely filled with CH<sub>4</sub>, the explosion produced a smaller signature than had been anticipated.

For all events, the CO<sub>2</sub> radiation (solid line in figures 29 and 32) was visible for the longest time. Water emissions at wave numbers nearest the band heads (short dashed lines) persisted significantly longer than those at wave numbers far from the band heads (long dashed lines). This is to be expected since the source temperature falls rapidly as a function of time.

The atmospheric transmission models of McClatchey and Selby (reference 8) were used to generate the spectral transmission data shown in figure 33 for the path between the explosion and the interferometer on MB-3. The data was then convolved with the interferometer instrument line shape to give a spectrum directly comparable to the spectra measured by the interferometer. The transmission spectrum, along with the range data, was used to determine the spectral radiant intensity of event MB-3 at 0.11 and 5.15 seconds and the results are shown in figures 34 and 35, respectively. At the absorption band centers, where the atmospheric transmission is very small, the radiant intensity has great uncertainty. For this reason the 2300 cm<sup>-1</sup> (4.3 micron) and 3700 cm<sup>-1</sup> (.27 micron) regions have been masked out.

The relative behaviors of the spectral irradiances of the five GEST events at 3414 cm<sup>-1</sup>, a strong H<sub>2</sub>O emission region, are shown in figure 36. All of the irradiances at this wave number are similar up to one second. (It should be remembered that corrections for atmospheric transmission would increase the relative levels for DMB-1 to a little above those for the single balloon explosions.) Considerable variations occur after 1 second. For instances, the MB-4 irradiance decayed much more slowly than that from the other event; probably because this shot occurred in very calm conditions. It is possible that the variations and different decay rates were due to the effects of wind and turbulence.

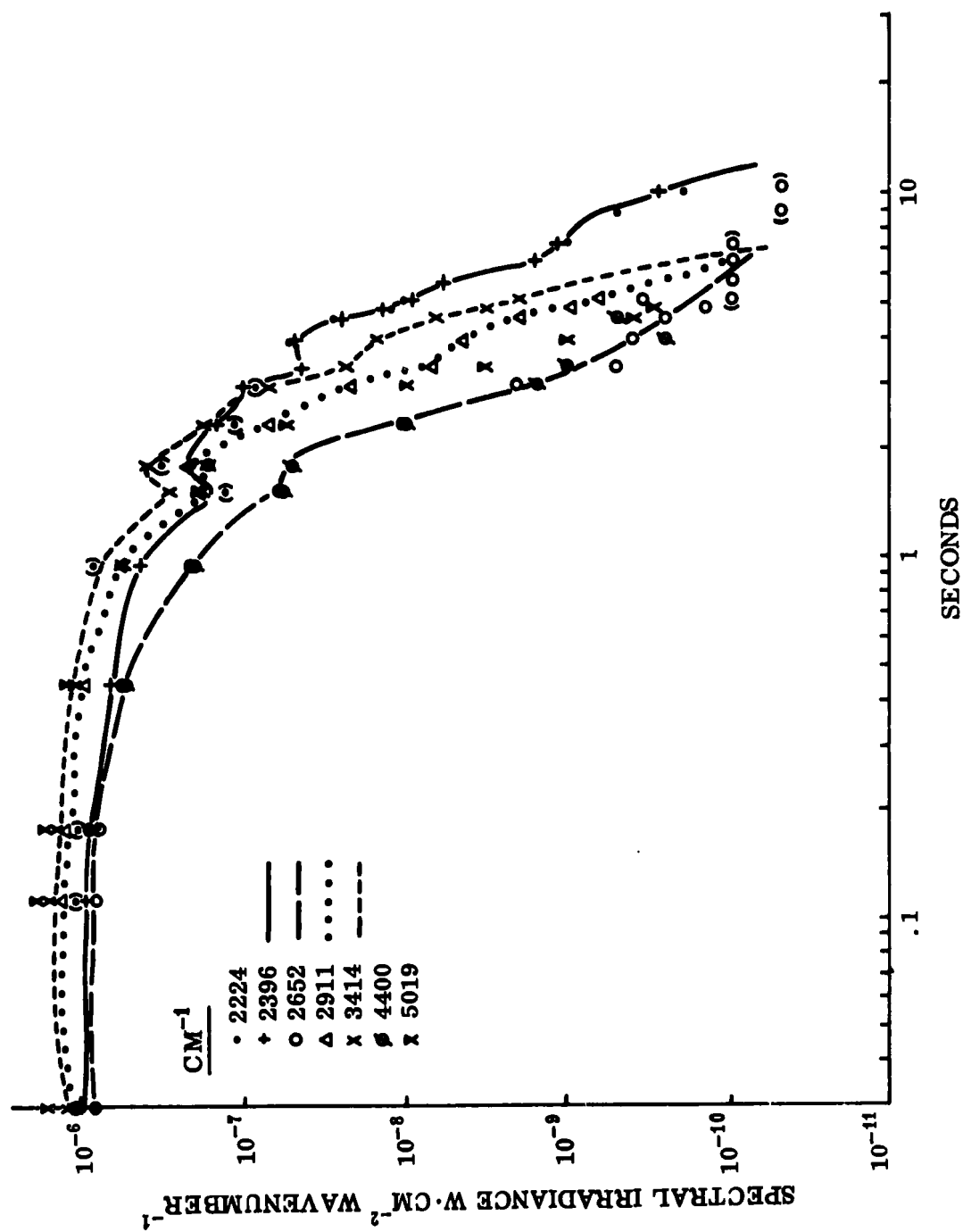


Figure 32. Spectral Irradiance versus Time for Event MB-3



MB-3 ATMOSPHERIC TRANSMISSION (Model at 4 CM<sup>-1</sup> Resolution)

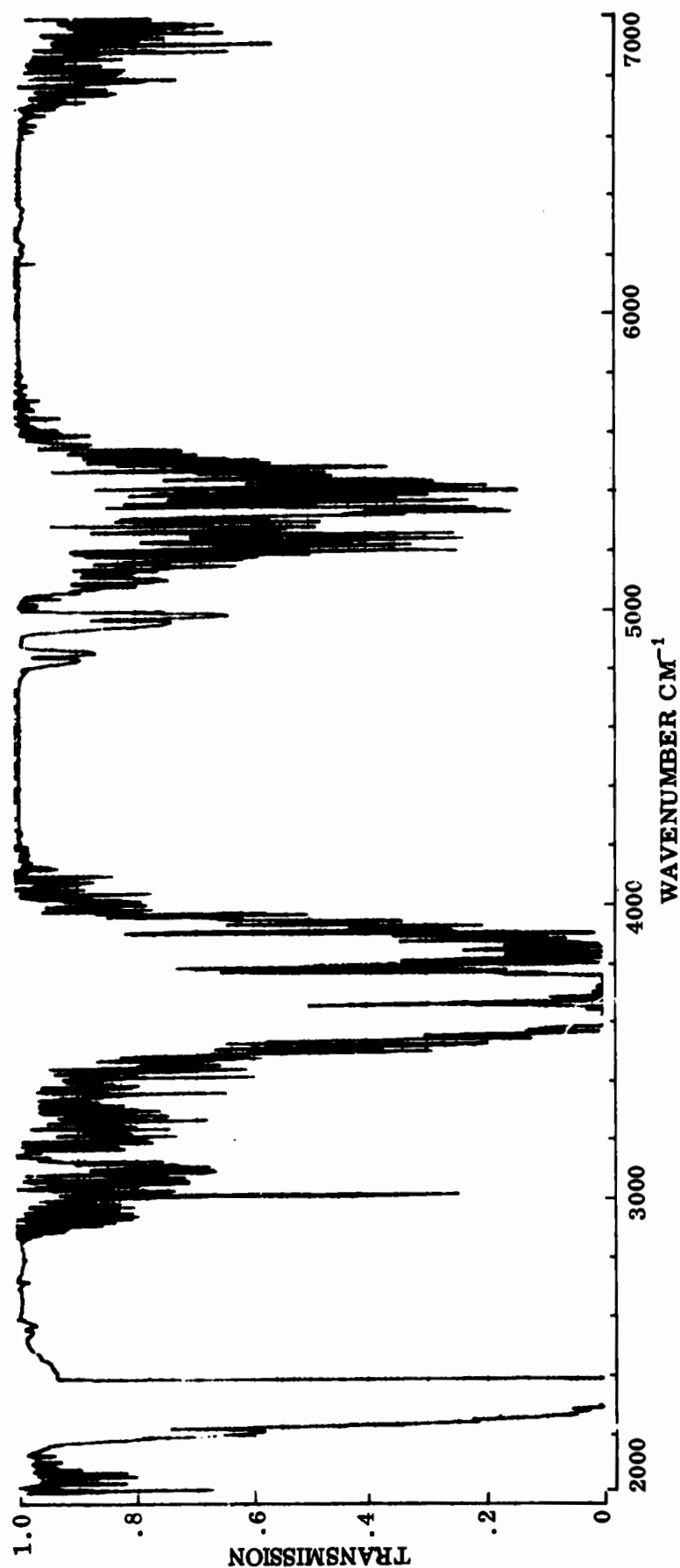


Figure 33. Atmospheric Spectral Transmission for Event MB-3

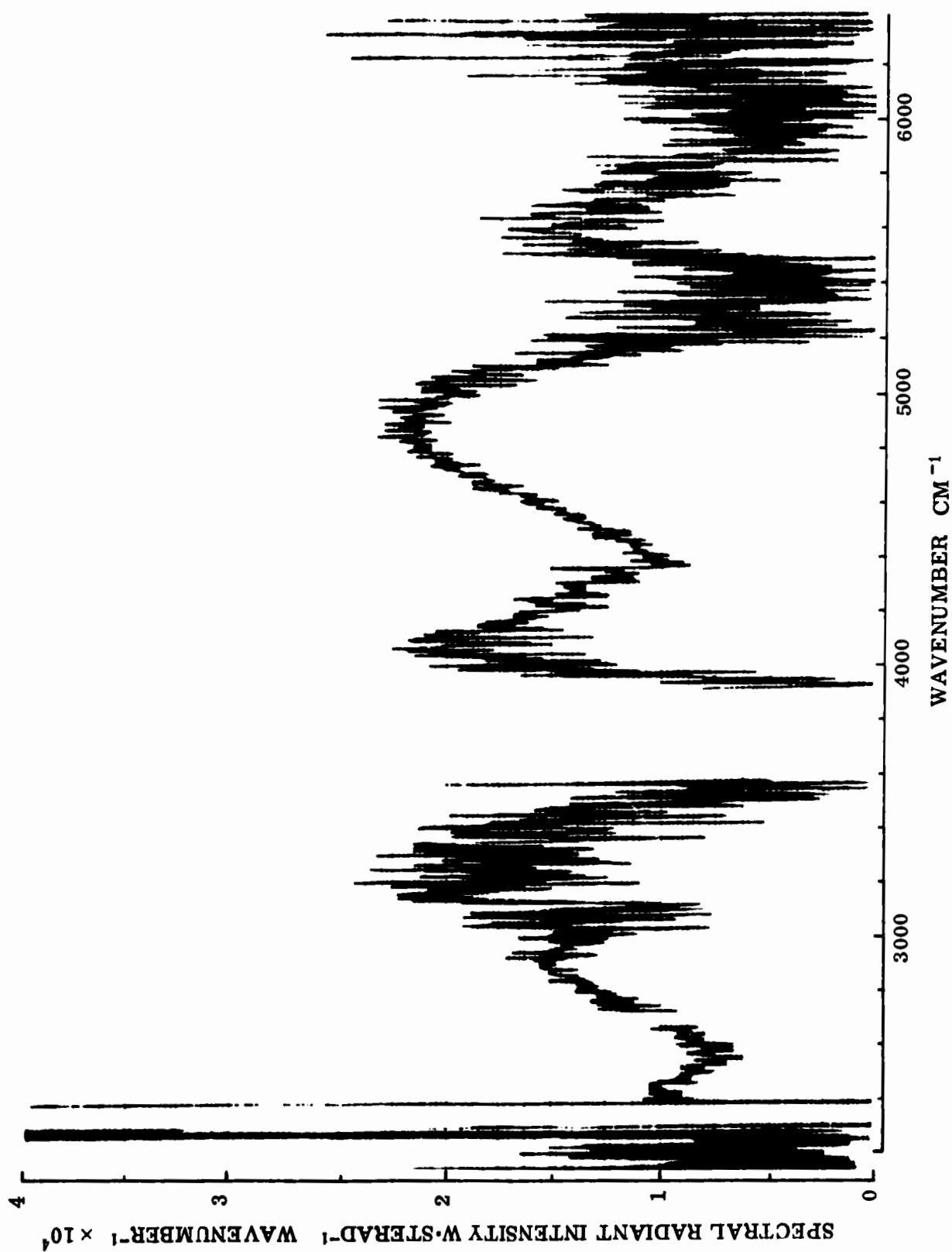


Figure 34. Spectral Radiant Intensity for Event MB-3 at 0.11 Seconds

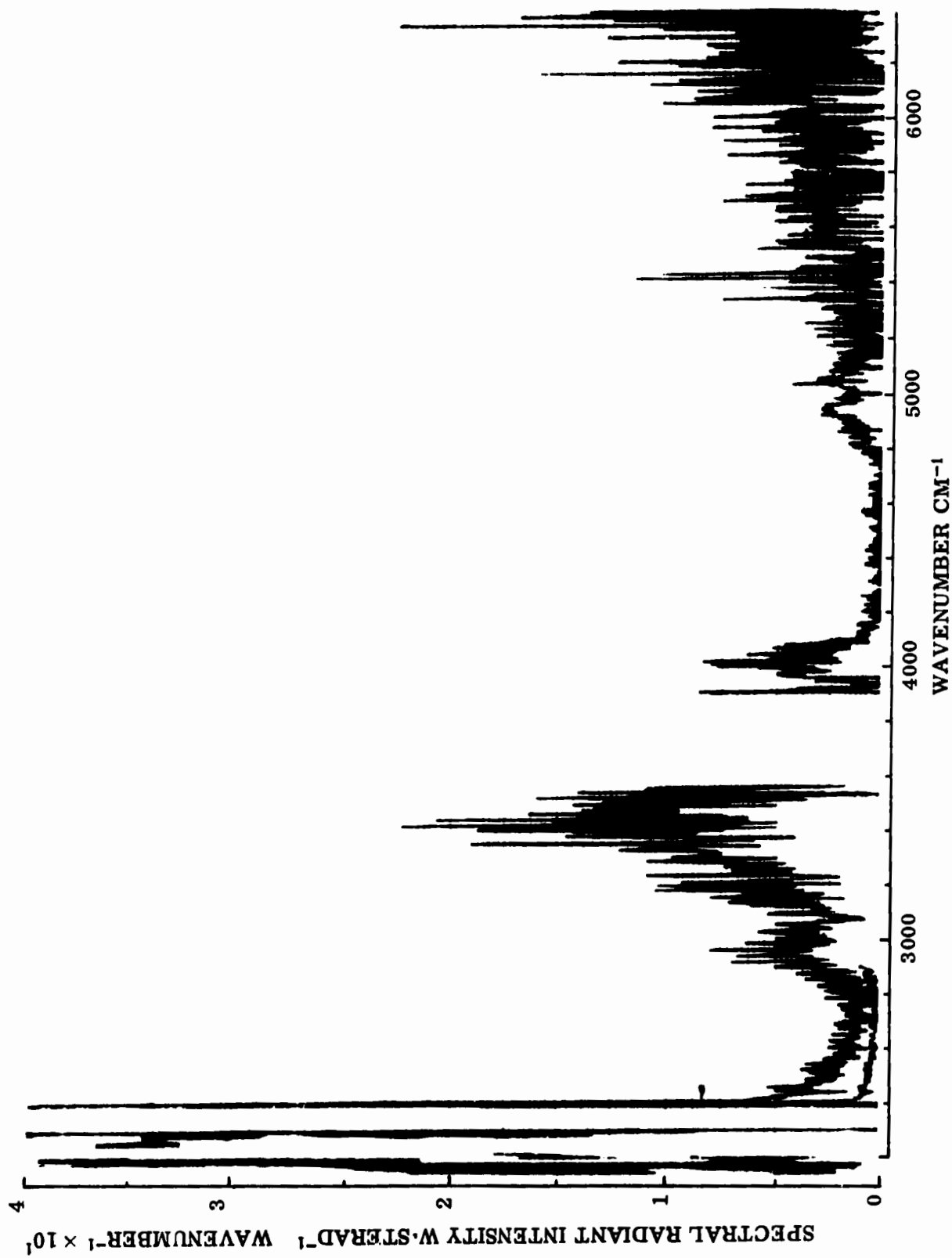


Figure 35. Spectral Radiant Intensity for Event MB-3 at 5.15 Seconds

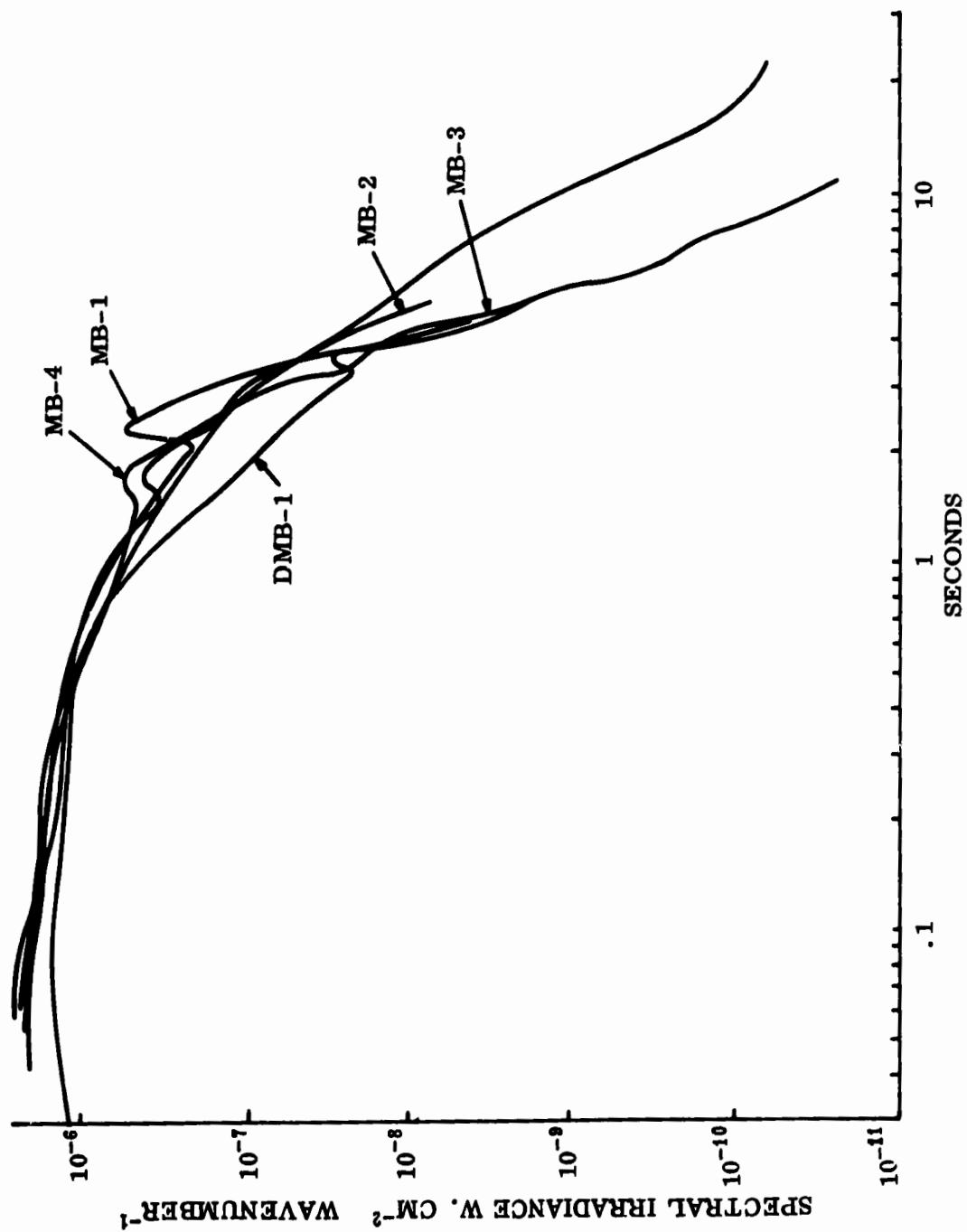


Figure 36. Relative Spectral Irradiances at 3414 cm<sup>-1</sup> - GEST Events

The behavior of the sharp  $\text{CO}_2$  spike at  $2396\text{ cm}^{-1}$  is shown in figure 37 for all events except MB-4, for which it was not measured. Again, all of the explosions produced similar results with the small fluctuations matching closely those shown in figure 36.

It is felt that the fireballs and debris clouds are optically thick during most of the observation period. Therefore, the data correspond to the radiation characteristics of the outer shell.

The  $\text{CH}_4\text{-O}_2$  spectra presented here appear to be in general accord with that predicted by F. N. Alyea (reference 9) although detailed comparisons have not yet been made. Water and carbon dioxide are apparently the predominant radiators.

The spectra have good resolution, which will allow good temperature information to be determined. This will provide an excellent base against which model predictions of fireball radiation can be compared. The spectral data indicate that the bulk of the radiation is from molecular radiators ( $\text{CO}_2$ ,  $\text{H}_2\text{O}$ ) rather than from a blackbody-like continuum. Modeling of the spectral radiation as originating from these molecules will allow the temperatures of the  $\text{CO}_2$  and  $\text{H}_2\text{O}$  to be determined.

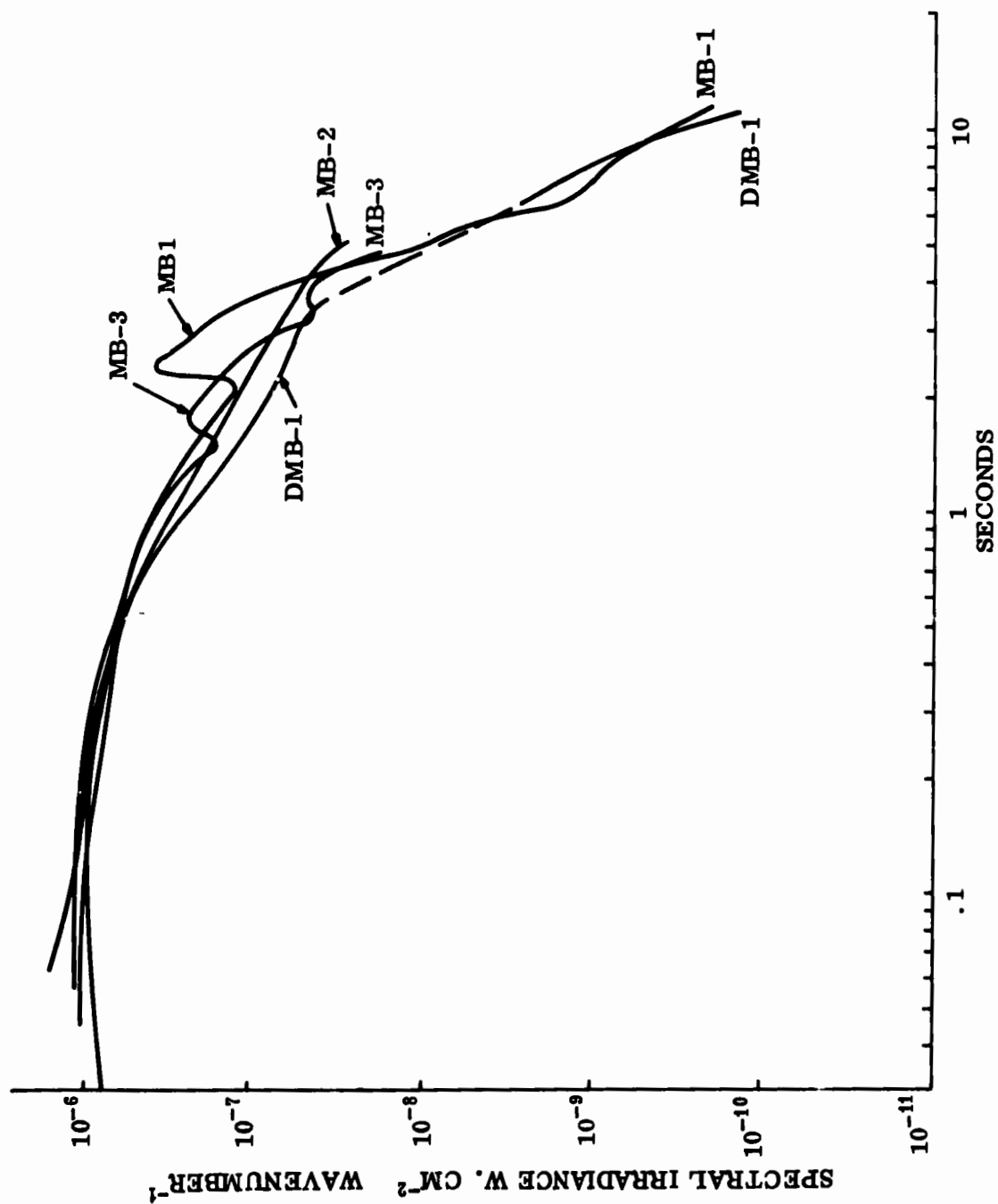


Figure 37. Relative Spectral Irradiance at 2396 cm<sup>-1</sup> - GEST Events

### 3. RAMAN SCATTERING EXPERIMENT TO DETERMINE AIR ENTRAINMENT RATES (Air Force Weapons Laboratory - Reference 15)

One of the experimental objectives of GEST was to determine the rate of air entrainment into the turbulent mixture of hot gases formed after the explosion. Laboratory experiments indicated that it would be feasible to determine this rate by measuring Raman scattering. An experiment was prepared for the double balloon event DMB-1; however, difficulties were experienced with the equipment prior to shot time and the experiment was aborted.

Raman scattering is a form of inelastic light scattering. When a photon of frequency  $\nu$  interacts with a molecule, a shift in frequency ( $\Delta\nu$ ) characteristic of the scattering molecule can result. The probability of the interaction taking place, while quite small, is directly proportional to the number of molecules or scattering centers available. Thus, for a given initial light intensity of known wavelength the intensity of Raman scattered light is directly proportional to the concentration of the scattering molecules.

Based on this effect the concentration of a given gas or gases in the turbulent atmosphere resulting from an explosion can be determined. If the concentration is determined as a function of time the rate of air entrainment can be deduced.

In order to demonstrate feasibility, a high-power, pulsed ruby laser (Space Rays Model OA-100) was used in a laboratory experiment. Although this particular laser could not be pulsed rapidly enough to determine air entrainment rates it was felt that a satisfactory analysis of a single pulse would demonstrate the validity of the approach. The experimental plan was:

- (1) to optimize laser operation so that the laser consistently produced a single pulse of the order of  $10^9$  watts.
- (2) to demonstrate, in the laboratory, an ability to detect the Raman scattered light.
- (3) to field the experiment on a GEST shot.

The optical pickup system consisted of a f1.5 cassegrainian telescope, an RCA 4526 (111 spectral response) photomultiplier tube (PMT), a Fluke 413B power supply, a Tektronix 454 oscilloscope and optical filters.

The optical filters were designed to transmit Raman scattered light from  $O_2$  and  $CO_2$  as follows:

- (i) The shifted line for 6943Å incident light is at 7783Å for O<sub>2</sub>.  
The filter used was a Heliotek #8874-19 spiked filter, centered at 7780Å with a 79.5% peak transmission and a 68Å half band width.
- (ii) The shifted line for 6943Å incident light is at 7683Å for CO<sub>2</sub>.  
The filter used was a Heliotek #8874-19 spiked filter, centered at 7694Å with a 73.5% transmission and a 32Å half band width.
- (iii) In order to insure suppression of wavelengths outside the desired band an additional 0.8μ filter was used in combination with each of the above. The combined filter system had a transmittance of 20% for 7683Å and 36% for 7783Å. The attenuation outside of the desired band was of the order of 10<sup>-7</sup> to 10<sup>-8</sup>.

The oscilloscope monitoring the PMT output was delay triggered using the output pulse of the Pockel cell supply of the OA-100 laser. A Pacific Photometric Instrument model 2A32 amplifier with a Lambda Model LT2095 AM power supply was added to the system when it was discovered that system rise time was too slow. The amplifier has a 1 ns rise time and a factor of 10 amplification. With this modification, the form of the detected pulse was similar to that of the laser pulse.

With the detector placed at various distances from the laser beam the Raman signal from O<sub>2</sub> in air was found to be a constant seven millivolts for a 400 Mw incident pulse. This observation was consistent with the low divergence of the Cassegrainian telescope used to collect the signal. Optical filters were interchanged to verify that it was, indeed, the Raman and not the Raleigh component which was being observed.

The system was fielded on DMB-1. The laser was placed approximately 1000 feet from one of the balloons. The optical pickup system was placed 328 feet from the balloon at right angles to the laser beam. The time delay adjustment was accomplished by looking at the integrated signal when the laser beam passed within a few feet of the telescope. Then with the amplifier in the PMT circuit, the Raman pulse was observed. The system was aligned so that the laser beam would intercept the hot turbulent gases from the balloon.

During alignment, a malfunction in the laser power generator apparently caused damage to the Pockel cell driver associated with the OA-100. Although the generator was repaired the laser would not then function correctly. Attempts to correct the difficulty failed and the experiment was aborted.



Although external difficulties prevented demonstration on the GEST experiment, laboratory experiments indicate that Raman scattering is a potentially successful remote analysis tool. Whether Raman scattering can be used to investigate the rate of air entrainment in an explosion thus, has not yet been determined. It is hoped that the opportunity to perform the experiment with another GEST type event will arise, and the results will be favorable, as expected.

#### 4. FAST RESPONSE TEMPERATURE MEASUREMENTS (TRW Systems Group - Reference 16)

The purpose of this task was to conduct flow field temperature measurements within the rising fireballs of the GEST methane-oxygen detonations. Measurements were obtained on the single balloon events MB-1 through MB-4 and on the double balloon event DMB-1. These measurements were made using an array of fast response hot wire probes.

Twelve sensors were used for each event, nine of them being operated as heat transfer gages (constant temperature) and three as constant current resistance thermometers (T<sub>ve</sub>). The two types of hot wire probes used are shown in figure 38. In all cases the platinum-iridium wire sensors were 0.00025 inches in diameter. In the constant temperature mode the wire sensors were maintained at a temperature of approximately 900°C by the anemometer feedback bridge. All data were recorded on a VR-3700B Magnetic Tape Recorder in the FM mode (DC to 10 kHz).

In the time span over which shock front temperatures were measured (0-0.5 seconds after time zero) all of the sensors performed satisfactorily on events MB-1, MB-3, and MB-4. Nine returned good data on event MB-2, and seven on DMB-1. Fireball temperature data was not obtained on MB-1, and three sensors recorded the temperature of the fireball leading edge only on MB-2. The entire fireball time span was covered for events MB-3, MB-4, and DMB-1. For this data interval (1.8 to 4.1 seconds for MB-3 and MB-4 and 1.6 to 4.6 seconds for DMB-1) nine, ten, and seven of the sensors performed satisfactorily for the three events respectively. The portion of the fireball time span covered on MB-2 was 0.7 to 1.2 seconds.

Ten of the sensors were mounted on a triangular framework called the main probe strut. The other two were mounted on an auxiliary strut. Figure 39 is a photograph of the main and auxiliary struts attached to the overhead cable. With the vertical leg of the main strut triangular framework positioned at approximately 40 feet from the fireball centerline, the two instrumented legs measure data both in the azimuthal and radial directions. The use of seven and three probes, spaced 18 inches apart on the azimuthal and radial legs, respectively, provided results spanning the expected dimensions of interest. All wire sensors were aligned in a direction orthogonal to the vertical plane through the overhead cable. The length of the probe stem mounts (10 inches)

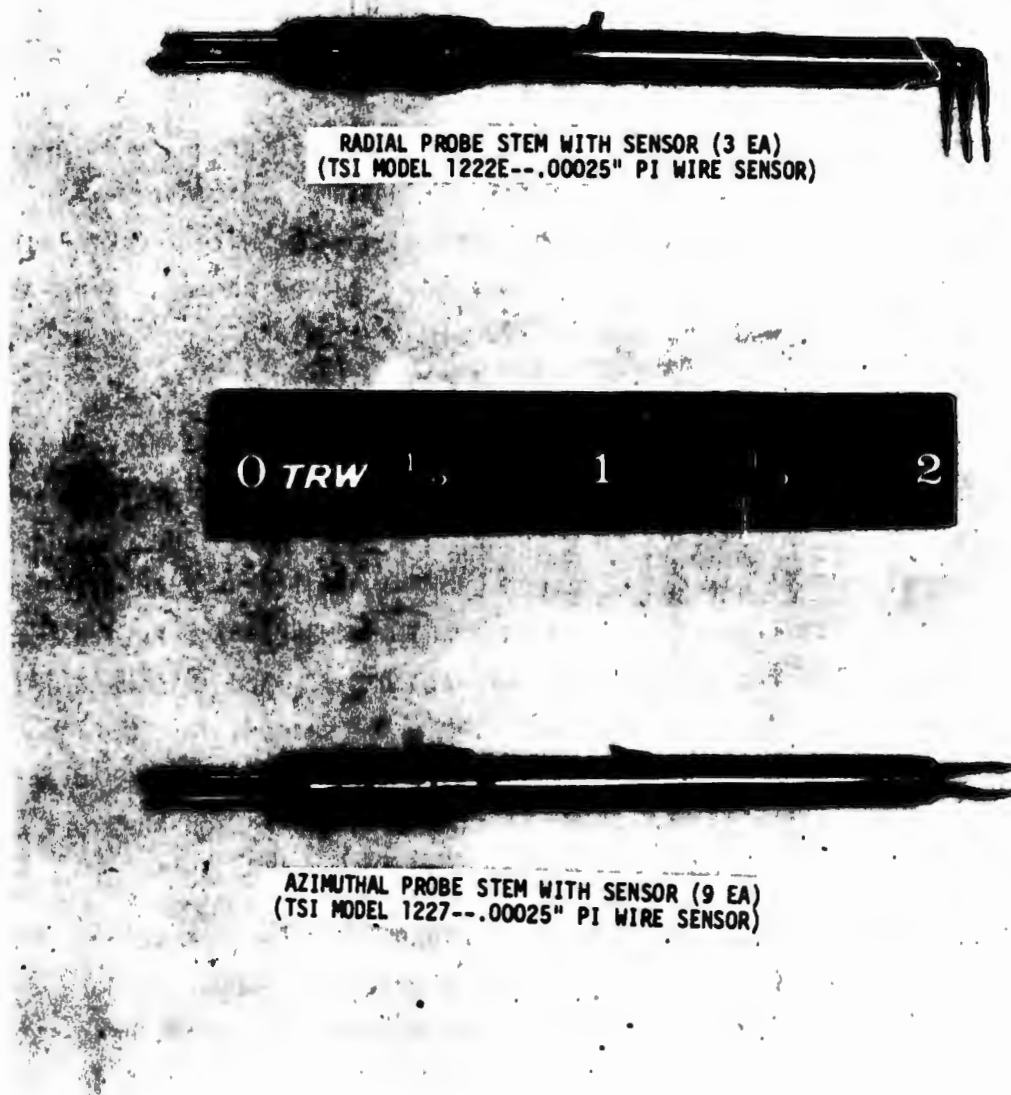


Figure 38. Hot Wire Probe Configurations for GEST Temperature Measurements



Figure 39. Probe Strut Installation - Event MB-4

and the orientation angle for the radial sensors ( $15^\circ$ ) were selected to minimize possible interference effects from the supports. Test configuration drawings for the single and double balloon GEST events showing positions of the temperature probes are given in figures 40 and 41.

Typical sensor time histories for the three radial sensors installed on MB-4 are presented in figure 42 and 43. Responses of the heat transfer gages (channels 1 and 3) and the temperature gages (channel 2) to shock front motion and fireball are distinctly different. This difference is a direct result of the heat loss equation for the constant temperature hot wire which, for a rising fireball, is given approximately by

$$e^2 \sim \dot{q} \sim (cT + \sqrt{u}) (T_w - T)$$

Here  $e$  is the bridge output voltage,  $\dot{q}$  is the sensor heat transfer rate,  $c$  is a constant,  $u$  is the local flow velocity,  $T_w$  is the wire temperature (constant  $\approx 800^\circ\text{C}$ ), and  $T$  is local flow temperature. Although the bridge power signal represents the combined effects of both the velocity and temperature fields within the fireball, its dependence on velocity is relatively small, both because of the square root dependence on flow velocity and because the heat transfer constant  $c$  is rather large. Velocities within the fireball can be determined approximately from optical data as well as from statistical analysis of turbulence data. As a result, the heat transfer measurements can be reduced to provide relatively accurate temperature data, with a 5 kHz frequency response as obtained from the anemometer feedback bridge. Such data complements the results obtained from the constant current sensors which, because of sensor thermal response characteristics, are limited to a frequency response of 1 kHz.

Additional fireball characteristics noted from the figures were:

- (1) the fireball was turbulent and non-homogeneous in nature at early times
- (2) temperature fluctuations were of the same order as the "mean temperature potential"
- (3) channel 2 temperatures approached  $1000^\circ\text{C}$
- (4) the mean temperature gradient at the fireball leading edge ( $d\bar{T}/dx$ ) was approximately equal to  $15^\circ\text{C}/\text{cm}$ . This is similar to the predicted value (10 to  $15^\circ\text{C}/\text{cm}$ ). Instantaneous temperature gradients at eddy interfaces were as high as 200 to  $300^\circ\text{C}/\text{cm}$

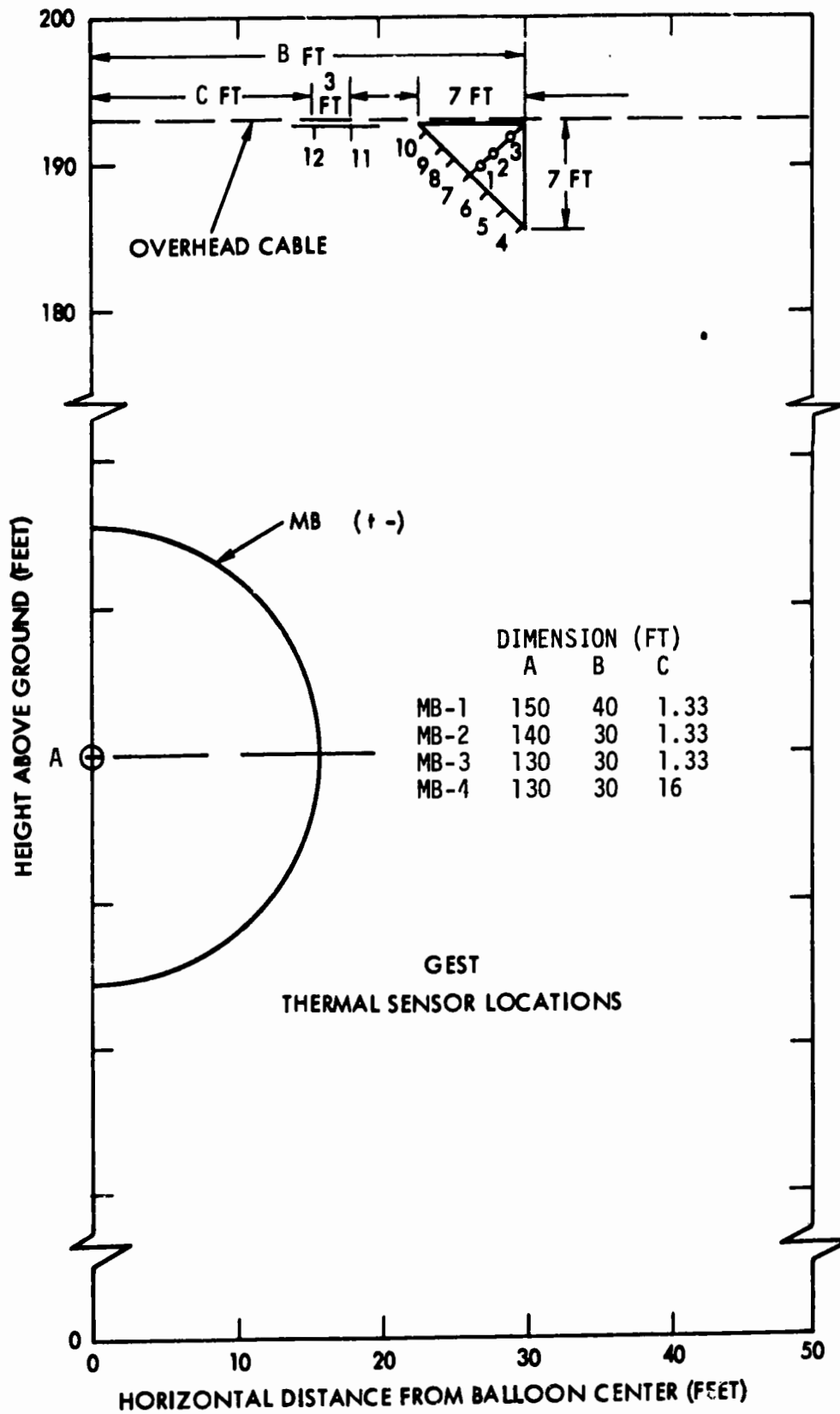


Figure 40. Thermal Sensor Locations - Events MB-1 through MB-4

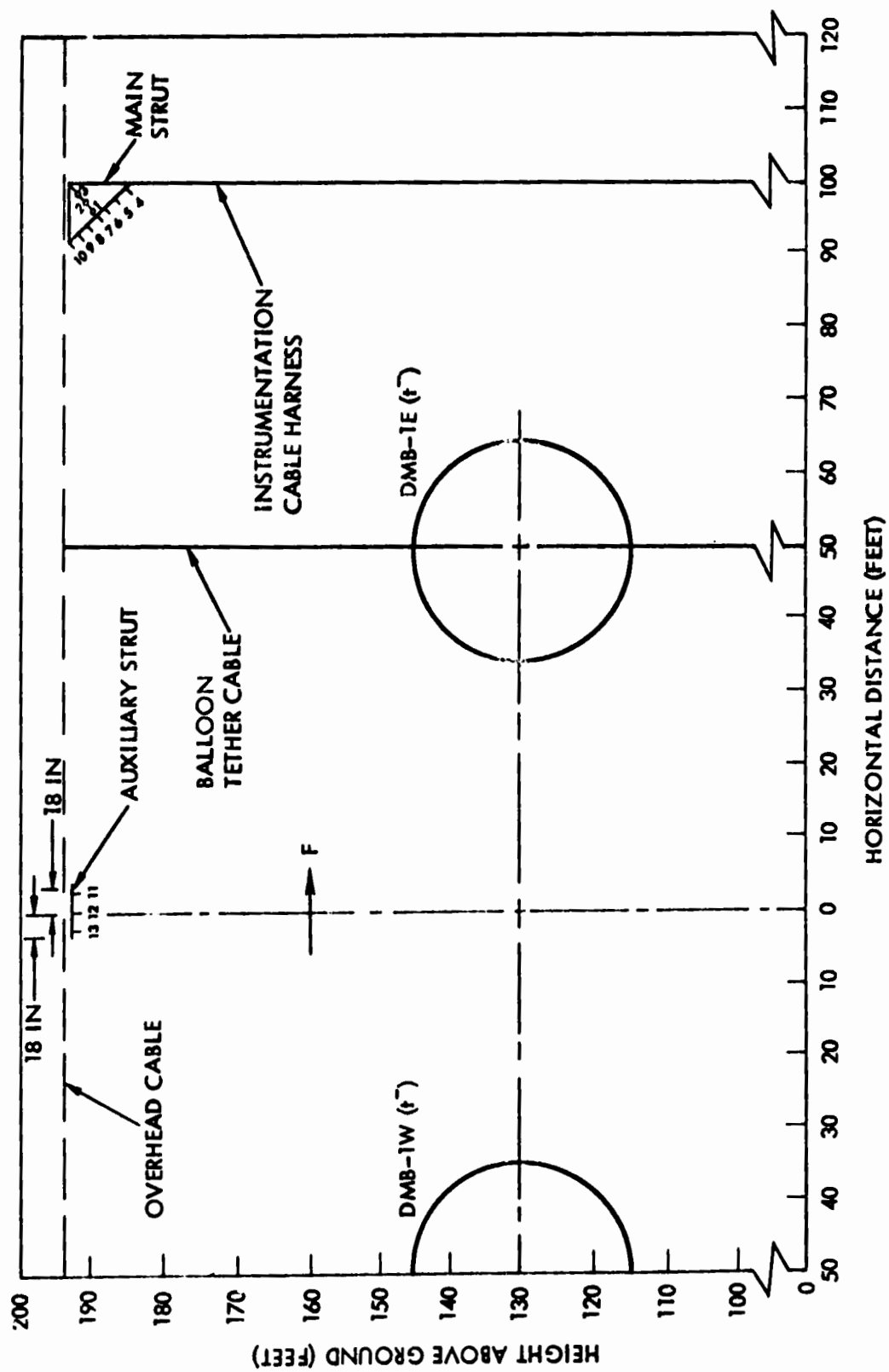


Figure 41. Thermal Sensor Locations - Event DMB-1

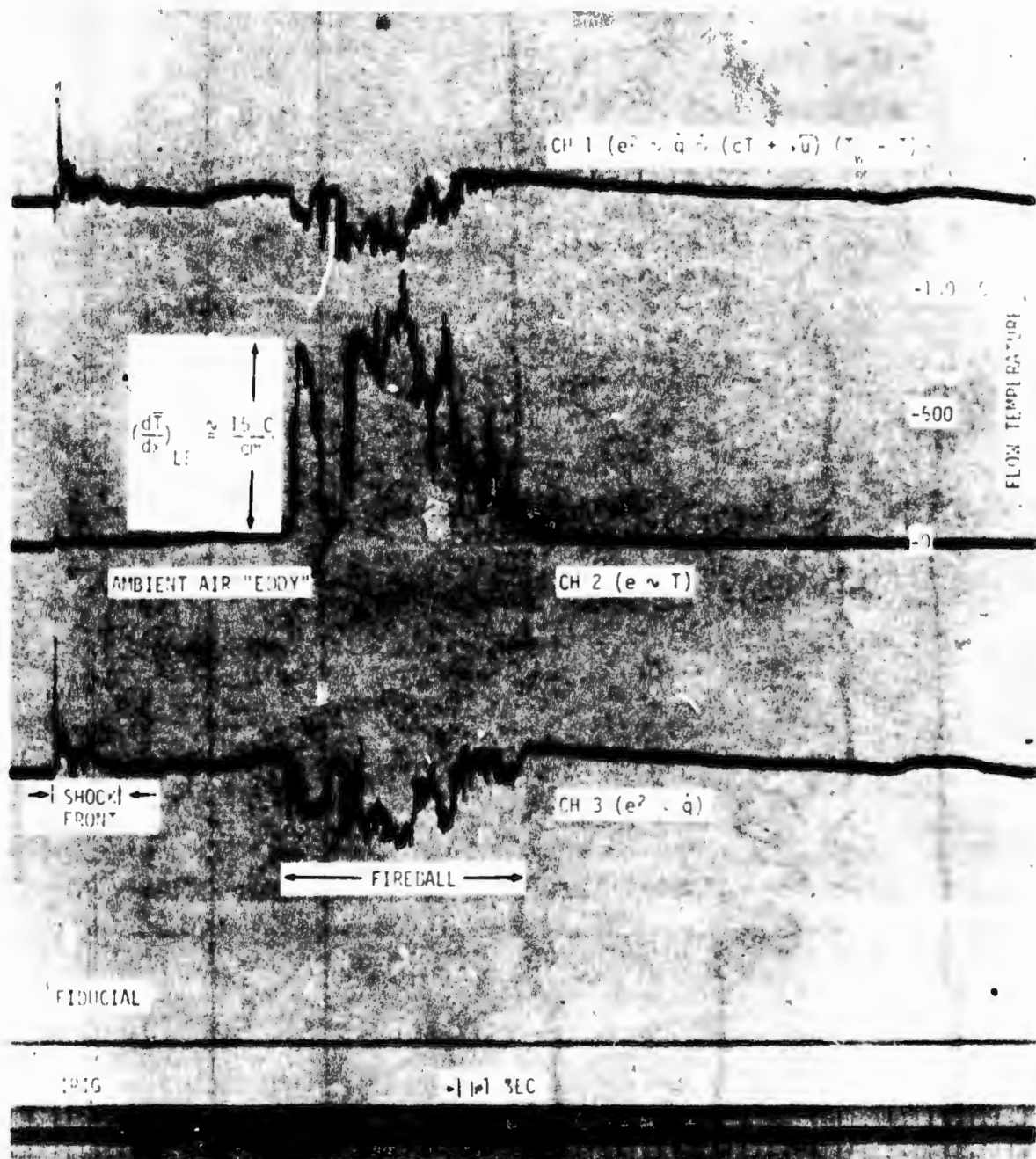


Figure 42. Thermal Time Traces - Event MB-4



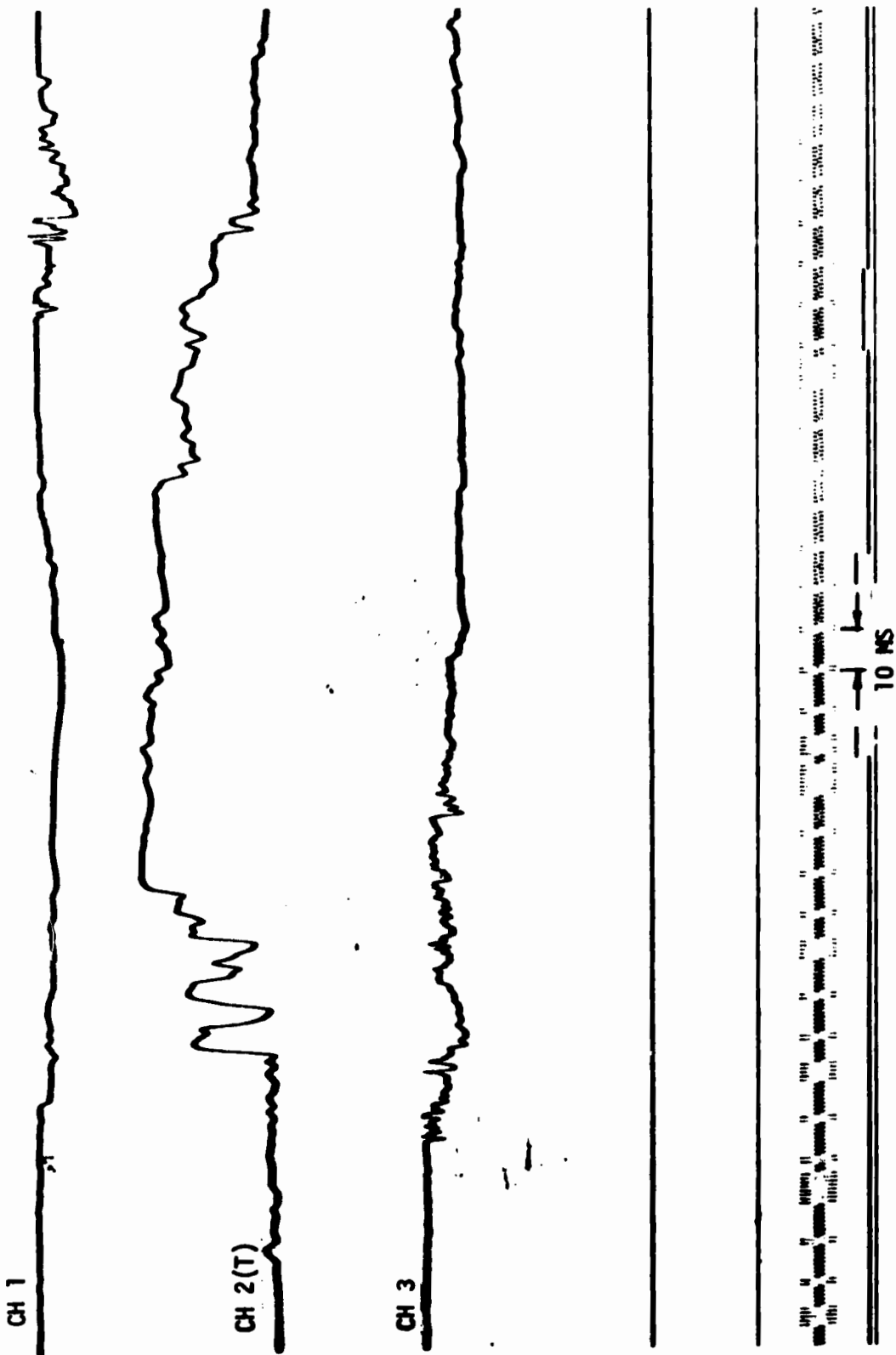


Figure 43. Expanded Thermal Time Traces - Event MB-4

- (5) ambient air eddies (pockets) were near the fireball leading edge
- (6) there was general agreement among records as to the large eddy structure
- (7) a substantial ambient air heat transfer rate (large stem velocity after fireball passage) was indicated.

5. INFRARED VIDICON OBSERVATIONS  
(General Electric Company - Reference 17)

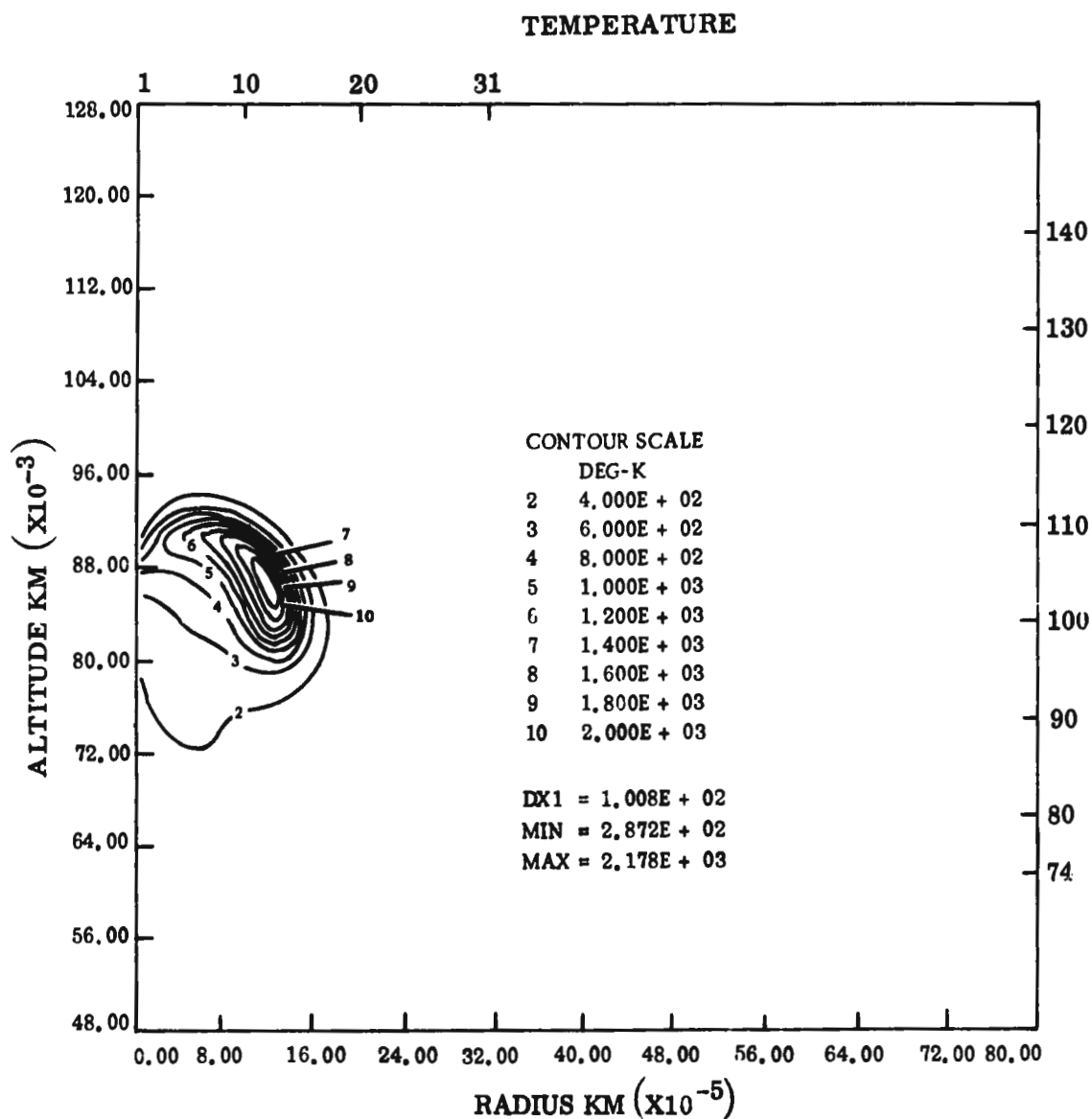
The General Electric Company Space Sciences Laboratory, under sponsorship of the Defense Advanced Research Projects Agency (DARPA), deployed two infrared vidicon camera systems to observe GEST events MB-3 and MB-4. These vidicon systems were equipped with narrow band spectral bandpass filters centered at 3.3 microns to provide infrared diagnostic data. Purpose of the observations was to aid in evaluation of the flow characteristics of fireballs. Of particular interest were the characteristics of torus formation, including formation rate and torus size and rate of rise. Temperature profiles across the torus were also of interest.

The predicted properties of the flow field associated with the debris of the balloon explosion were obtained from HULL hydrocode computations. These computations are described in reference 3. The major products of the explosion,  $\text{CO}_2$  and  $\text{H}_2\text{O}$ , exhibit strong infrared signatures at wavelengths between 2.5 and 3.5 microns. In order to obtain spectral radiant intensity predictions, the temperature, pressure, and concentration profiles provided by the calculation were used to solve the radiative transfer equation. These predictions, for the center of the bright regions, are shown in figures 44 and 45 for 2 seconds and 6 seconds after detonation.

Two infrared vidicon cameras were employed for the measurements. The cameras had identical spectral bandpass characteristics, but had predicted dynamic intensity ranges which were arranged in such a way as to maximize the total range of source intensities which could be observed.

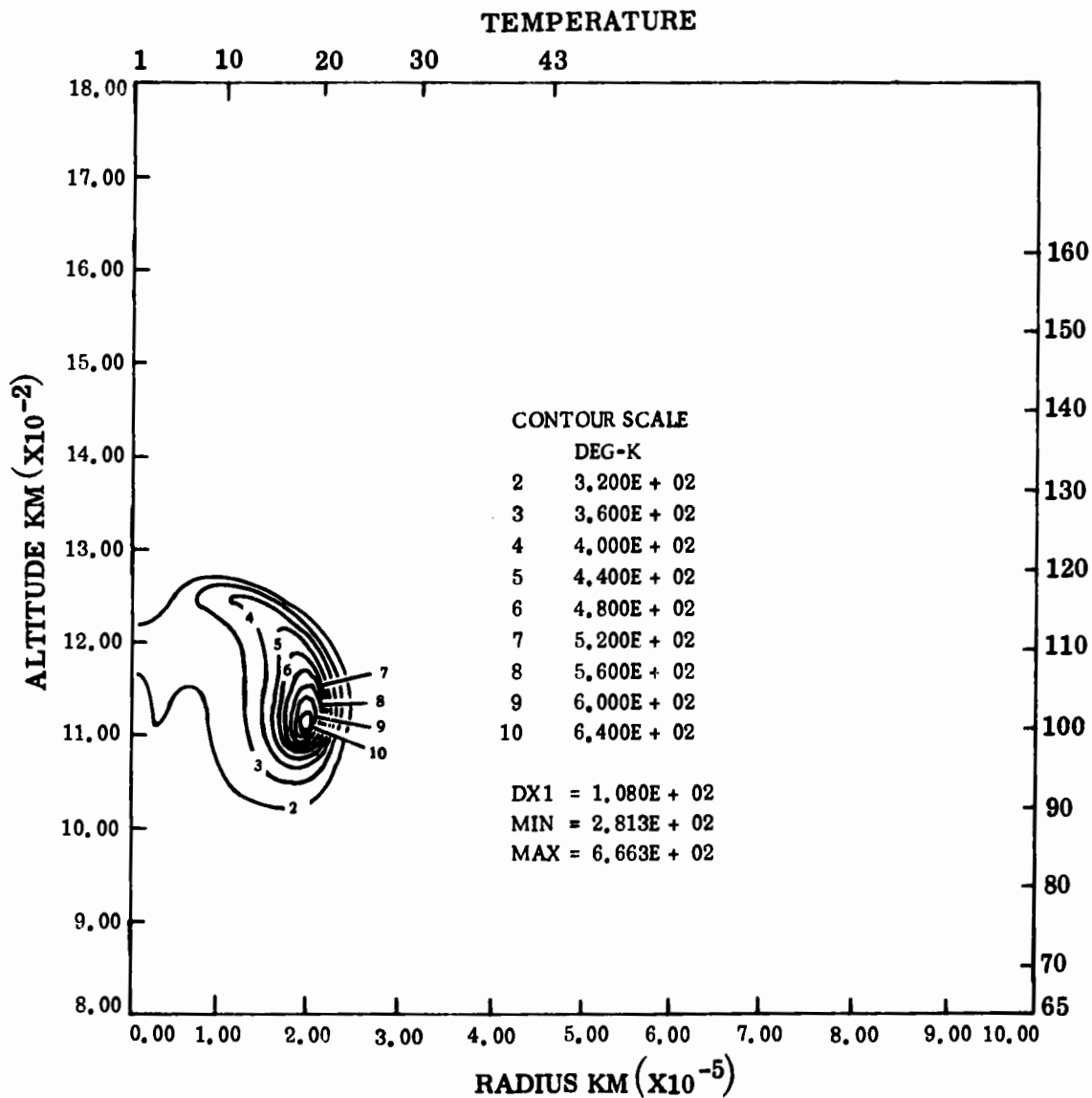
System 1, the "Belvoir" camera, was borrowed from the Army Night Vision Laboratory at Fort Belvoir, Virginia. It is a General Electric 27934R reticulated Ge:Cu vidicon. Optics consisted of a 10-inch focal length f/2 lens. The cryogenic system was a pressure Dewar with controlled  $\text{LN}_2$  feed to the sensor. The unvignetted field of view was  $4.1^\circ \times 4.1^\circ$ .

System 2, the "NRL" camera, was supplied by the Naval Research Laboratory. It is a General Electric Z7876 Ge:Cu vidicon with a 4-inch focal length f/1 lens. The cryogenic system required hand filling the  $\text{LN}_2$  supply to the vidicon tube. Unvignetted field of view was  $5.0^\circ \times 5.0^\circ$ .



AFWL HULL CALCULATION OF 5 M CH<sub>4</sub> BALLOON AT 70 M SAP INPUT 19 OCT 72  
 TIME 2.000 SEC                      CYCLE 6233.                      PROBLEM 50.0000

Figure 44. Predicted Event Temperature Profile at T = 2.0 Seconds



AFWL HULL CALCULATION OF 5 M CH4 BALLOON AT 70 M SAP INPUT 19 OCT 72  
 TIME 6.000 SEC                      CYCLE 13666.                      PROBLEM 50.0000

Figure 45. Predicted Event Temperature Profile at T=6.0 Seconds

Both systems used standard 30 frame per second television rasters. Data was recorded on Ampex VR7000 video recorders. The calibration source in each case was a Barnes Engineering Company Model LL-140T Blackbody with a 12 x 12-inch radiating area.

Both cameras had identical spectral bandpass filters with the transmission curve given in figure 46. This spectral bandpass was determined as a trade-off between optical thickness effects, atmospheric transmission, required dynamic range and the spectral response of the vidicon. The vidicon spectral response, from reference 10, is shown in figure 47.

An observation wavelength of 3.3 microns was chosen for both cameras in order to observe hot H<sub>2</sub>O bands while minimizing the complicating effects of radiation from other debris species. At this wavelength, the predicted radiant intensities (figures 44 and 45) are about 3 watts/cm<sup>2</sup> ster micron at two and six seconds after detonation respectively. The requirement for the overall dynamic range of the instrumentation for the measurements of interest was, thus, about 3000. Normally, the maximum achievable dynamic range of the cameras is about 60 to 100.

The predicted noise equivalent spectral radiances for the Belvoir and NRL cameras were determined to be  $3.6 \times 10^{-5}$  and  $2.45 \times 10^{-5}$  watts/cm<sup>2</sup>-ster-micron, respectively, under the measurement conditions of the GEST tests (reference 3). These levels denote the minimum signal intensities that can be resolved. Thus, while the cameras had sufficient sensitivity to observe the event at late times (around 6 seconds), they did not have adequate dynamic range to encompass the full range of event radiance variation from early to late times.

To extend the useful dynamic range of the cameras, each was fitted with a removable aperture stop consisting of a metal plate with a small hole drilled in it. These aperture stops were held in front of the camera optics by hand so that they could be quickly removed when the event spectral radiance fell beneath the sensitivity limit of the stopped-down camera, as evidenced by a fading of the TV image. The Belvoir camera stop consisted of a plate with a 0.138-inch diameter hole, which, when placed over the five-inch diameter optics allowed a net transmission of 0.076%, forming an f/72 optical system. Similarly, the four-inch NRL lens was stopped with a 0.66-inch aperture, giving a transmission of 2.7%, or an f/6 optic. In this manner, the camera dynamic ranges were extended to cover the entire region of interest, as shown in figure 48.

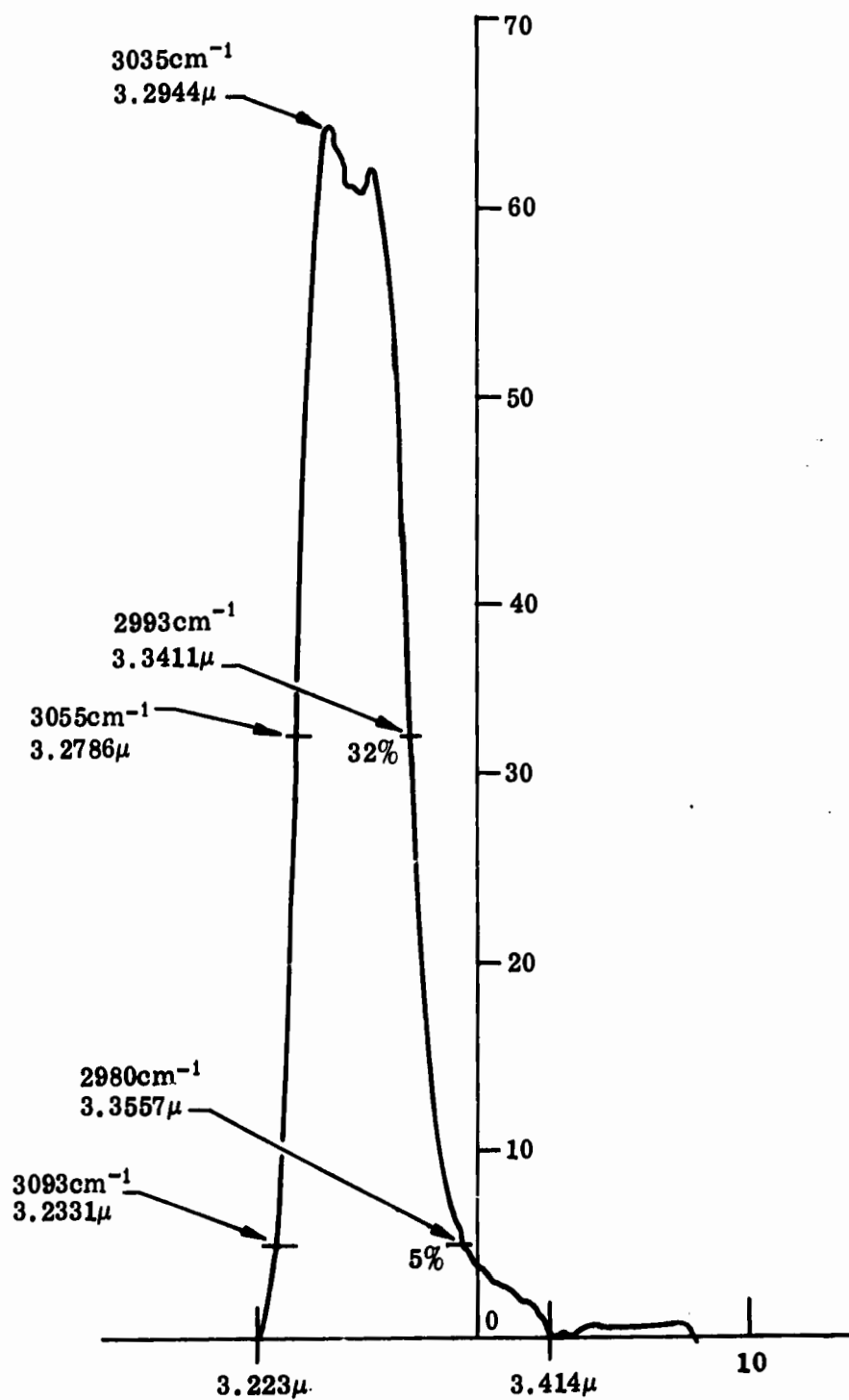


Figure 46. Vidicon Spectral Filter Transmission Calibration Curve

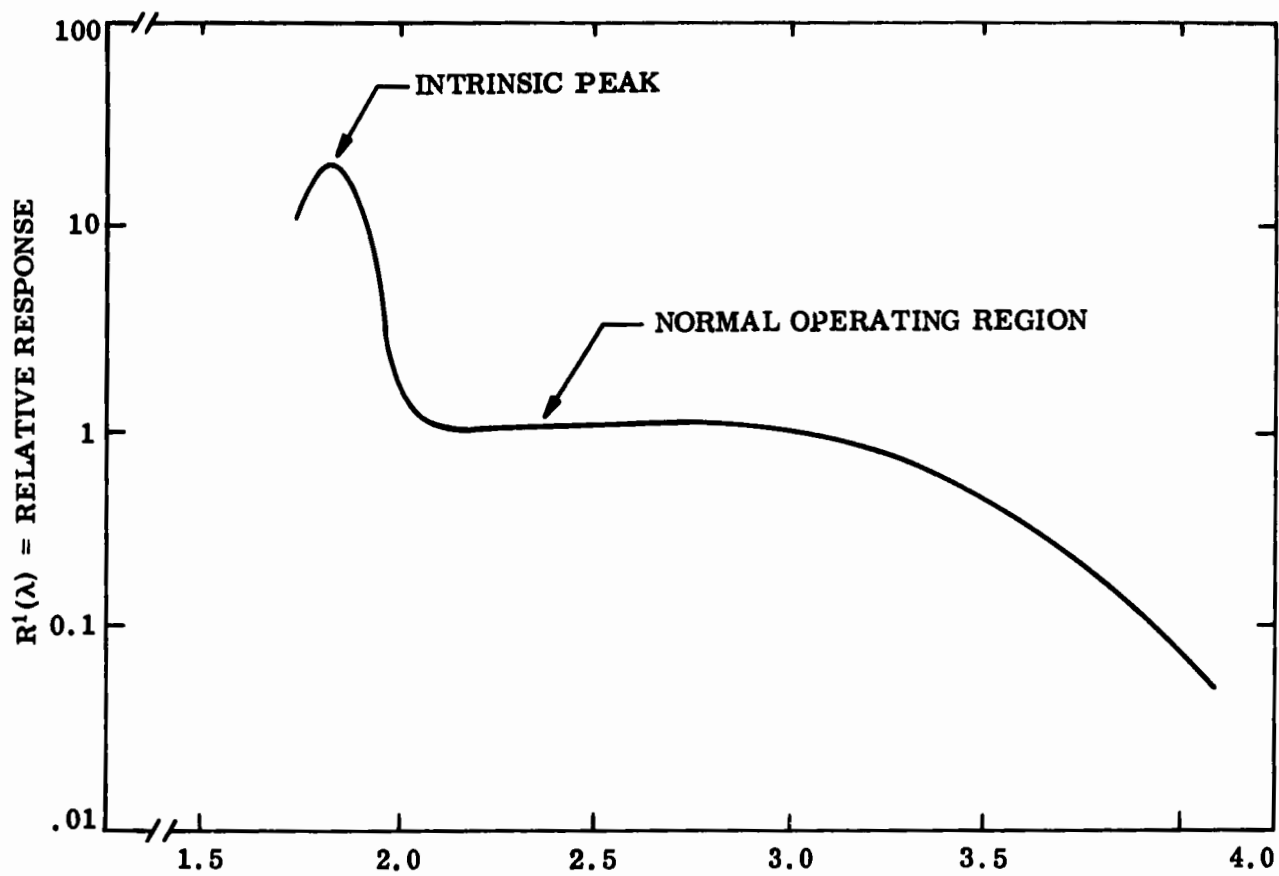


Figure 47. Ge:Cu Vidicon Spectral Response



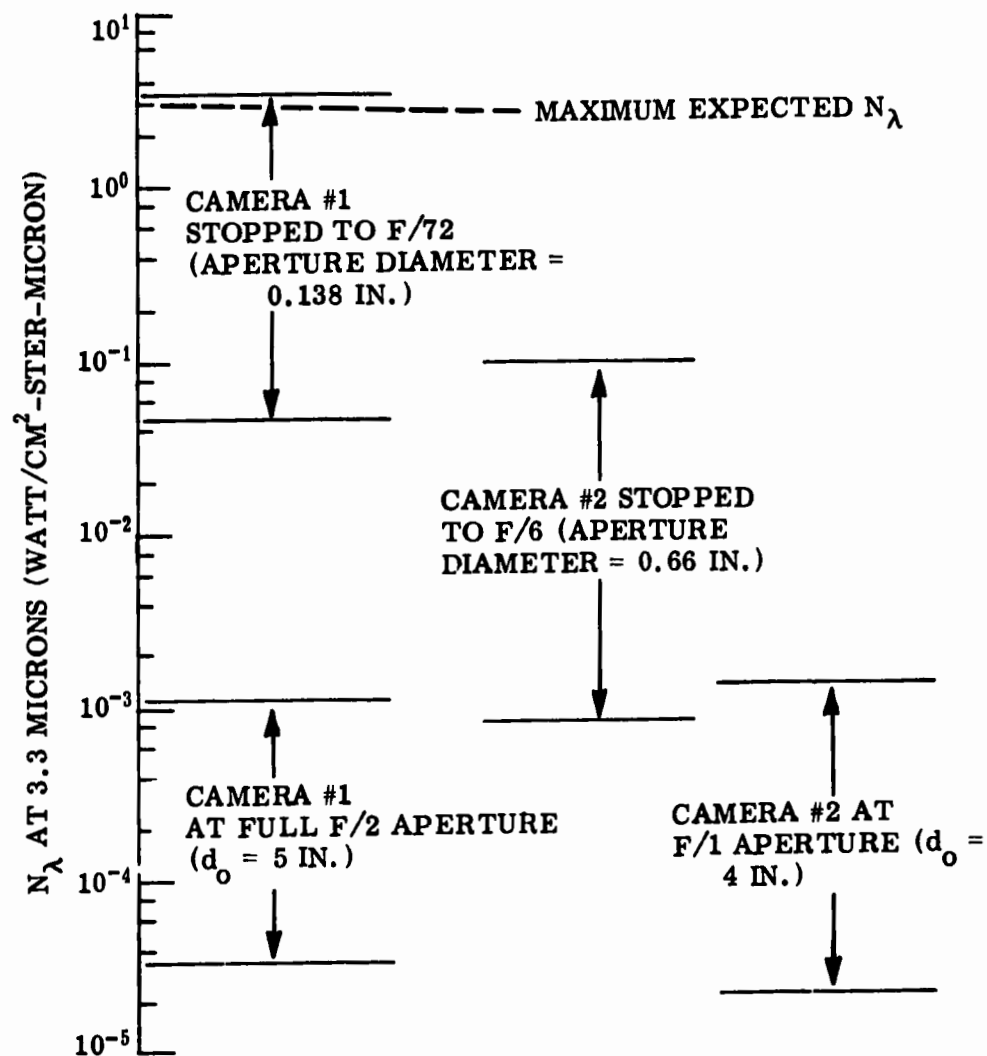


Figure 48. Vidicon Measurement Dynamic Range

The event spectral radiances were expected to be within the dynamic range of at least one of the cameras over the entire period of observation.

The camera systems were calibrated using the vidicon radiometric transfer function

$$S/N = C \int \Delta N_{\lambda(c)} R^1(\lambda) T_a(\lambda)_c T_o^1(\lambda) T_f^1(\lambda) d\lambda$$

where

$S/N$  = ratio of peak signal to peak-to-peak noise amplitude

$\Delta N_{\lambda(c)}$  = differential spectral radiance of calibration source above that of adjacent background in watt-cm<sup>2</sup>-ster-micron<sup>-1</sup>. At the source temperatures typically used in these calibrations,  $\Delta N_{\lambda(c)} \approx N_{\lambda(c)}$ ; that is, the background radiance is negligible.

$R^1(\lambda)$  = vidicon relative spectral responsivity normalized to the absolute value of vidicon responsivity at  $\lambda_{ref}$ , the center of the effective system passband.

$T_a(\lambda)_c$  = atmospheric spectral transmission over the calibration path.

and

$T_o^1(\lambda)$  and  $T_f^1(\lambda)$  = relative optics and filter transmission normalized to their absolute values at  $\lambda_{ref}$ .

The radiometric calibration process consists of measuring the calibration constant  $C$  in terms of observed values of  $S/N$ , given values of  $\Delta N_{\lambda(c)}$ , and the calculated value of the integral in the preceding equation. The calibration was performed at the instrument settings at which the data was obtained.

A posttest calibration was also performed, which consisted of observing the radiance of a 12 x 12-inch blackbody source at a distance of approximately 50 feet from the vidicon cameras. Five source temperatures were used. The calibration integrals were evaluated using atmospheric transmission over a 50-foot horizontal path length at atmospheric pressure and a temperature of 25°F. Altitude was taken to be 6000 feet and relative humidity 25%. A light haze (slight scattering loss) was assumed. From reference 11, an atmospheric transmission ( $T_a(\lambda)_c$ ) of 0.995 at  $\lambda = 3.3$  microns was assumed.

The results from posttest calibration of the Belvoir camera are shown in figure 49. This calibration differed from predicted performance and

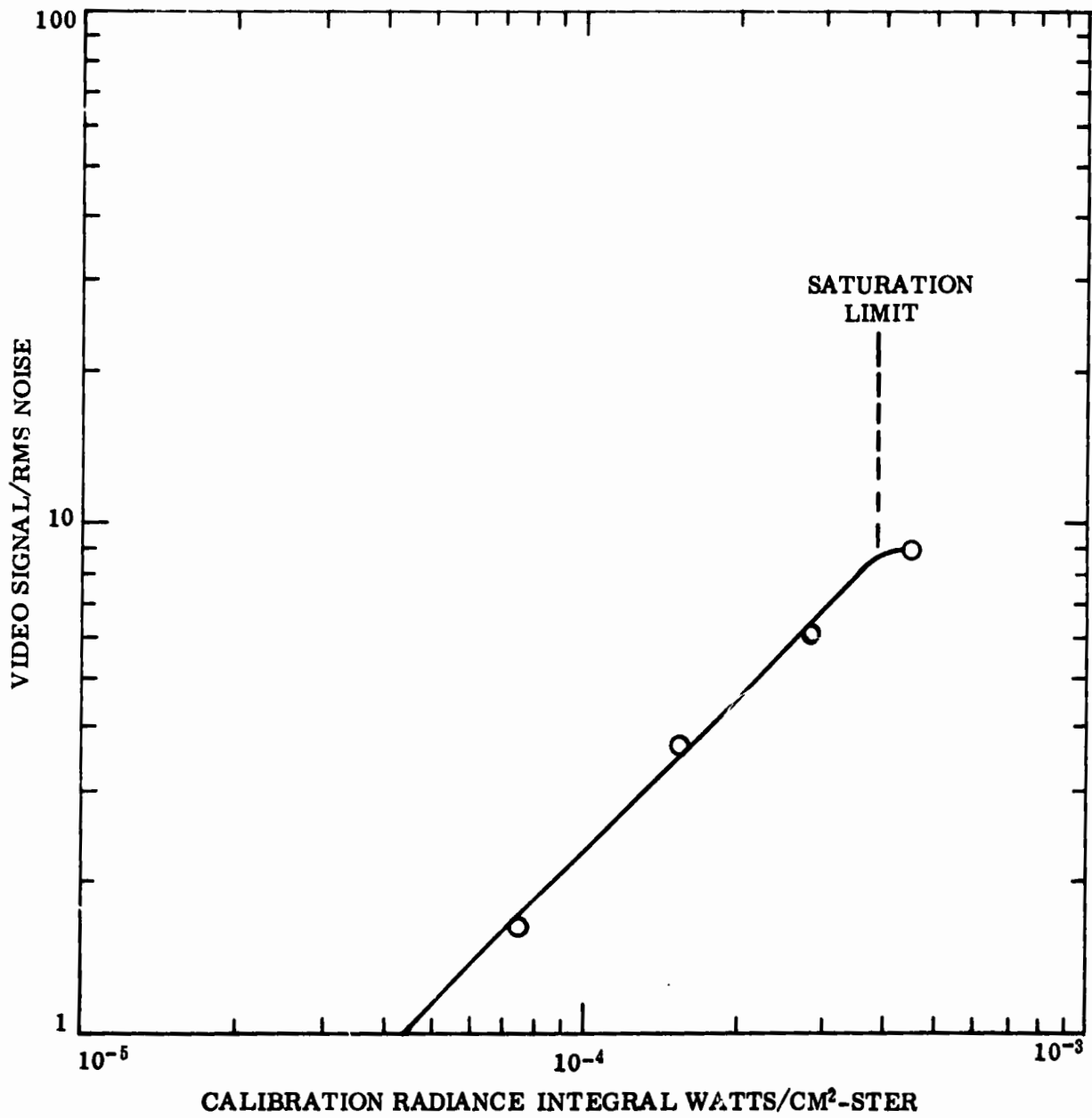


Figure 49. Belvoir Camera Post-Mission Calibration

pretest laboratory calibration in that the observed threshold at  $S/N = 1$  was approximately three times that previously noted. Dynamic range was similarly decreased. This was probably due to increased noise in the video recordings taken at the field site.

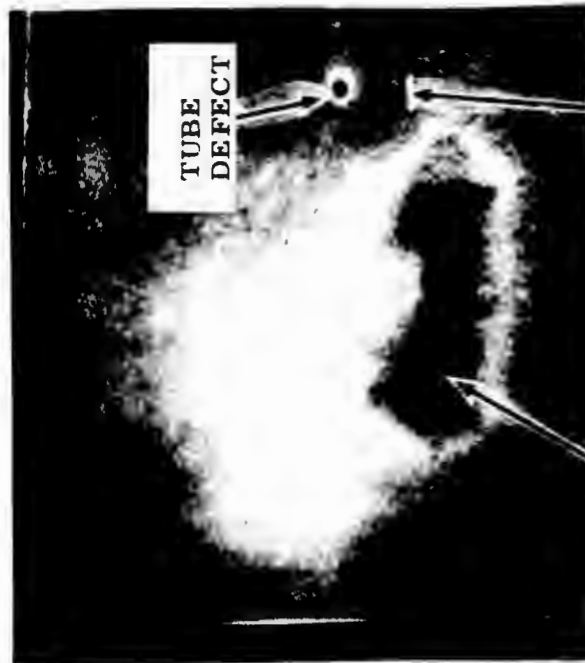
The NRL camera vidicon tube was quite old and began to "go soft" after arrival at the field site. A replacement was not available in time for the tests. As a result, noise equivalent source radiance was an order of magnitude higher than expected and dynamic range was drastically reduced. A noise-equivalent source radiance of  $1.62 \times 10^{-4}$  watt/cm<sup>2</sup>-ster was determined from the posttest calibration data.

The best data was obtained by the Belvoir camera on MB-4. Because the absence of a boresite lamp on the cable made optical alignment impossible, no data was obtained by this camera on event MB-3. On MB-4, the Belvoir camera observed the event from detonation to about  $T + 9.5$  seconds. The system was saturated over part of the middle region as predicted by the experiment plan (reference 12).

The NRL camera obtained 5 seconds of data on both MB-3 and MB-4. This camera was successfully aligned for MB-3 even without the boresite lamp. Despite the vidicon degradation discussed previously, the NRL data is of adequate quality to allow identification of source characteristics at the threshold intensity, which for this camera was about equivalent to a 465°K blackbody.

A sample data frame is given in figure 50. The data is displayed and analyzed on a video tape display station which permits a single video frame to be shown on a TV monitor, or C-scope, and also permits a single video amplitude of a single TV scan line to be displayed on an oscilloscope, or A-scope. The TV scan line which has been selected for display on the A-scope is indicated by a white marker pulse on the C-scope. The position of the marker pulse on the scan line is shown as a pulse on the lower trace of the A-scope. The vidicon tube in the Belvoir camera had a major blemish on its retina, which shows up as a constant spot to the right of the frame center in the C-scope photograph. The sample data frame of figure 50 shows the rising cloud at a time when part of the signal is above the saturation limit of the vidicon. At saturation, the vidicon exhibits a reversal effect, so that the saturated portion of the image appears black on the C-scope. The black areas on the C-scope correspond to the minima in the A-scope video signal level.

VIDEO SIGNAL OF TV  
LINE INDICATED BY  
MARKER PULSE



BLACK REGION  
INDICATES SENSOR  
SATURATION

MARKER  
PULSE

C-SCOPE



INDICATES POSITION  
OF MARKER PULSE  
ALONG SELECTED  
TV LINE

A-SCOPE

Figure 50. Sample Vidicon Data Frame

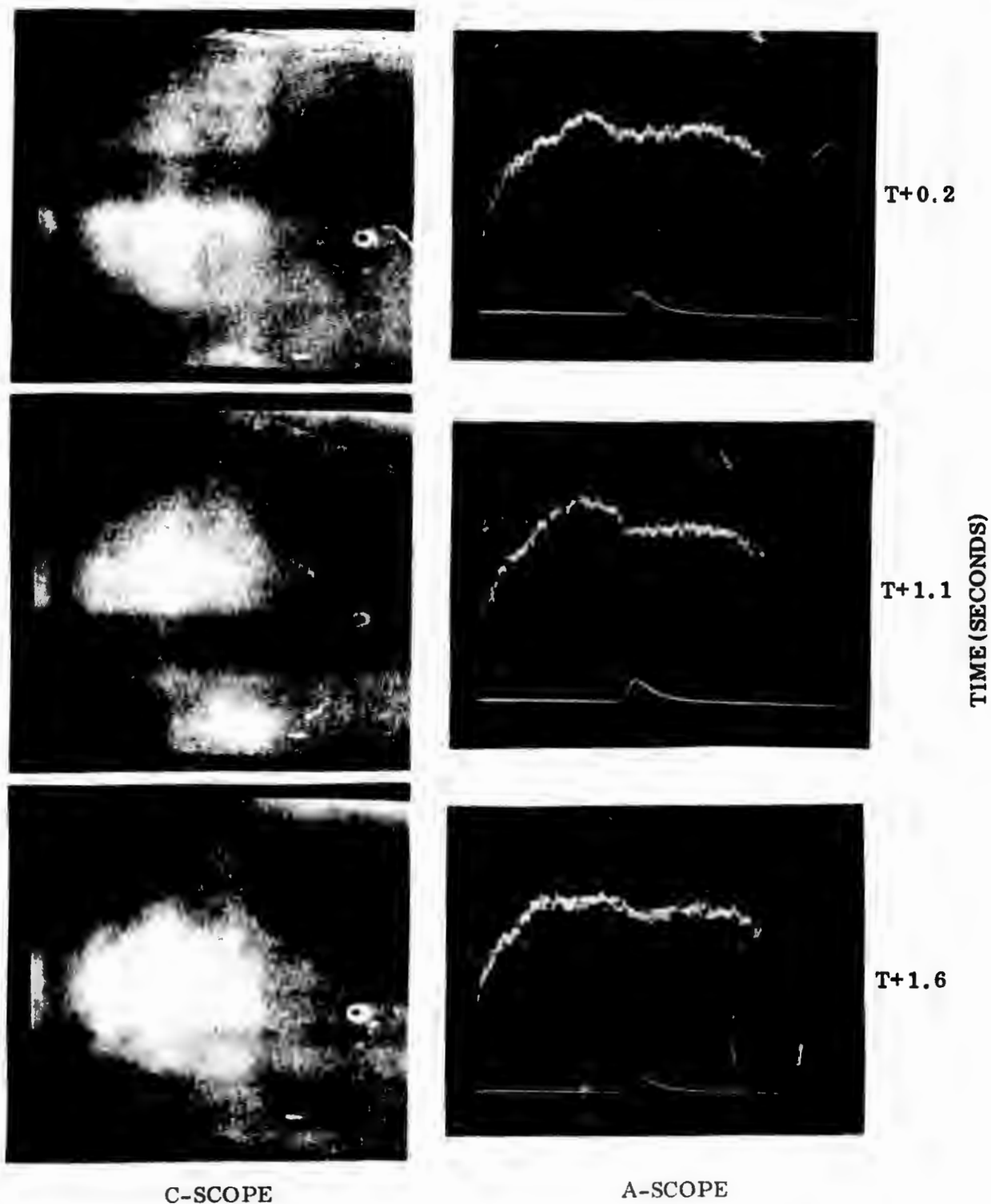
Typical data frames from the exploding balloon event MB-4 are shown in figure 51. The first frame, corresponding to time of  $T + 0.2$  seconds, shows the cloud entering the bottom of the camera field-of-view. Because the aperture stop was in place at detonation, the observed intensity is actually attenuated by a factor of  $7.6 \times 10^{-4}$ . The next two frames, at time  $T + 1.1$  and  $T + 1.6$  seconds, show the rise of the roughly spherical cloud. During this period the radiant intensity of the cloud is falling rapidly, and shortly after the  $T + 1.6$  second frame intensity falls below the threshold of the vidicon.

At this point in time, the aperture stop was removed from the camera lens. The results are shown in part 2 of figure 51. The frame at  $T + 2.8$  seconds and the next frame are interesting in that they show the cloud while the aperture stop was being removed. The dynamic range distribution shown in figure 48 indicates that, for the Belvoir camera, there is an interval of time in which the radiant intensity is below threshold for the stopped vidicon but above the saturation limit for the unstopped vidicon. The aperture stop was removed manually, and therefore complete removal required a finite time. These two data frames were obtained when the aperture stop was only partially removed. The cloud radiant intensity, however, falls within the dynamic range of the partially stopped vidicon. These frames clearly show the flattening of the cloud and the beginning of torus formation.

When the aperture stop is completely removed, at  $T + 3.1$  seconds, saturation obscures the details of the central cloud structure.

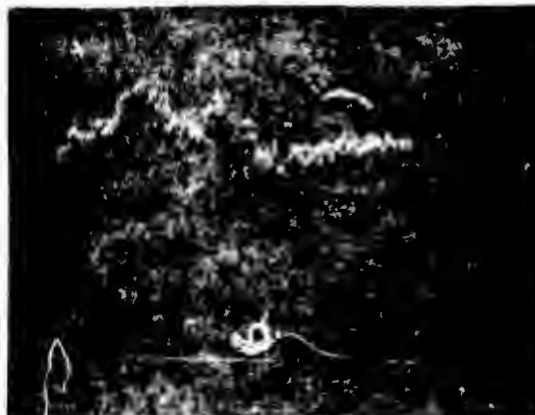
The next series of data frames, part 3 of figure 51, shows further flattening of the cloud and much clearer definition of the torus. By  $T + 5.0$  seconds, the torus is well defined with a very conspicuous size and intensity imbalance between its right and left sides. The early stages of this imbalance can be seen in the  $T + 2.8$  frame.

The final series of data frames, part 4 of figure 51, shows the fade-out of the fully developed torus. The frames at  $T + 7.5$  and  $T + 8.5$  seconds show the fully developed torus and a cross-section of the much brighter left side. A feature of the data, not apparent in the still frames but readily discernable in the video data, is a rotating or "churning" motion about the circular axis. At  $T + 9.5$  seconds, the torus simultaneously rises out of the vidicon field-of-view and falls below the instrument sensitivity threshold.

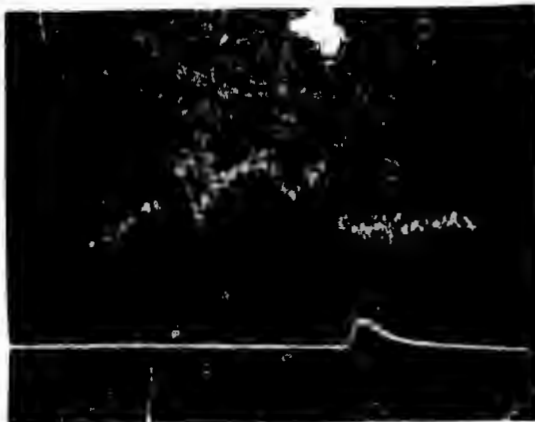


APERTURE STOP IN PLACE

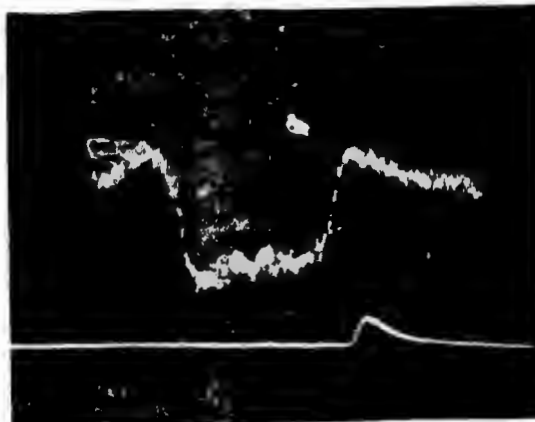
Figure 51. (Part 1) MB-1 Vidicon Data Frames



T+2.8



T+2.8  
+ ONE FRAME



T+3.1

TIME (SECONDS)

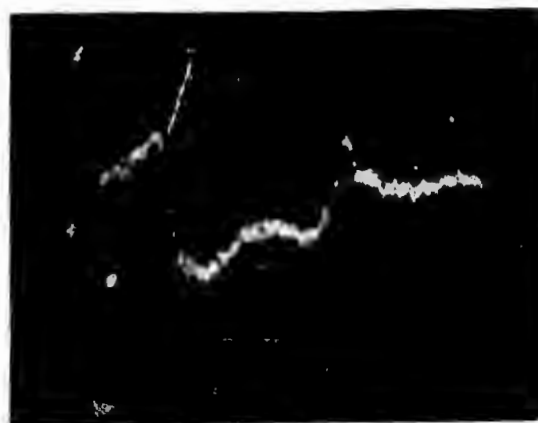
C-SCOPE

A-SCOPE

APERTURE STOP BEING REMOVED

Figure 51. (Part 2) MB-4 Video Data Frames (Continued)

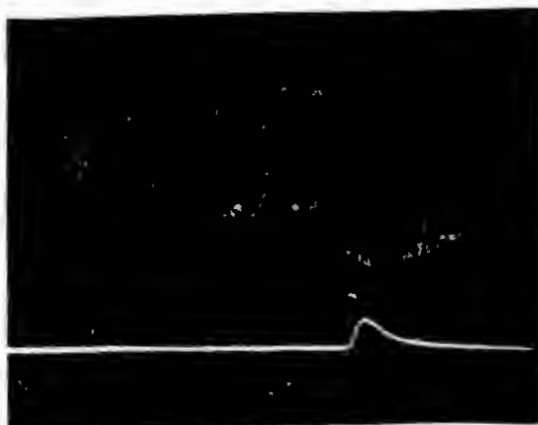




T+4.0



T+5.0



T+6.0

TIME (SECONDS)

C-SCOPE

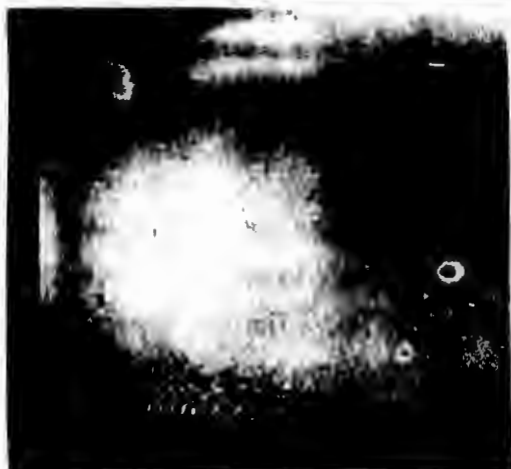
A-SCOPE

APEKTURE STOP FULLY REMOVED

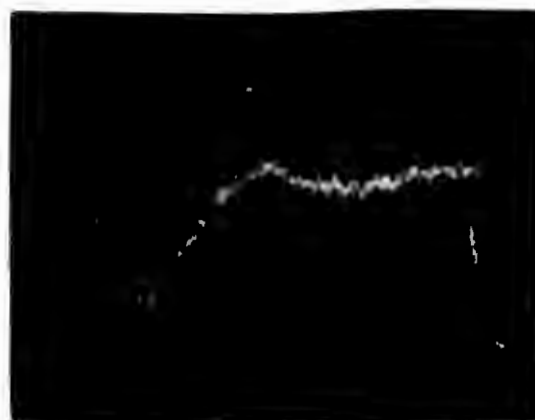
Figure 51. (Part 3) MB-4 Vidicon Data Frames (Continued)



T+7.5



T+8.5



T+9.5

TIME (SECONDS)

C-SCOPE

A-SCOPE

Reproduced from  
best available copy.



APERTURE STOP FULLY REMOVED

Figure 51. (Part 4) MB-4 Vidicon Data Frames (Continued)

Additional analysis of the data from MB-4 has produced the results shown in figures 52 through 62. Orientation of the left hand torus image outline at vidicon threshold as a function of time is given in figure 52. Data points from both the Belvoir (#1) and NRL (#2) cameras are included. Data from the two cameras are in good agreement and indicate how the image flattens out as the torus rises.

Figures 53 and 54 give the vertical dimension of each side of the torus as a function of time. The image outline is obtained from both cameras as a contour through vidicon threshold intensity. Imbalance between right and left sides of the torus is very apparent in figure 53. Horizontal torus dimensions as functions of time are given in figures 55 and 56. Torus separation, total image width, and cloud mean altitude as functions of time, as obtained from the Belvoir camera data, are given in figures 57, 58, and 59. Definitions of all of these quantities may be obtained from the small diagrams included with each figure.

Spectral radiant intensities across the horizontal field of view of the camera are presented in figures 60 and 61. Each line in the figures represents a single TV scan line, as might be displayed on the A-scope. The distance in meters of each scan line from the top of the image (threshold intensity) at the image plane is given in the figure key. All of the data in both figures 60 and 61 is taken from a frame at  $T + 5.9$  seconds.

Finally, the iso-intensity contour at  $2.5 \times 10^{-3}$  watt/cm<sup>2</sup>-ster-micron is plotted in figure 62. This contour is taken directly from the curves of figures 60 and 61 at  $T + 5.9$  seconds.

The data obtained by the Belvoir camera on MB-4 is of excellent quality and in general the experiment is considered to have been successful. Additional analysis is planned and will be available in the final report. A 16 mm film of the vidicon data can be obtained by contacting Rome Air Development Center/OCSE, Attention: Mr. Joseph J. Simons, Griffiss Air Force Base, Rome, New York 13441 (Refer to Contract F3602-73-C-0102).

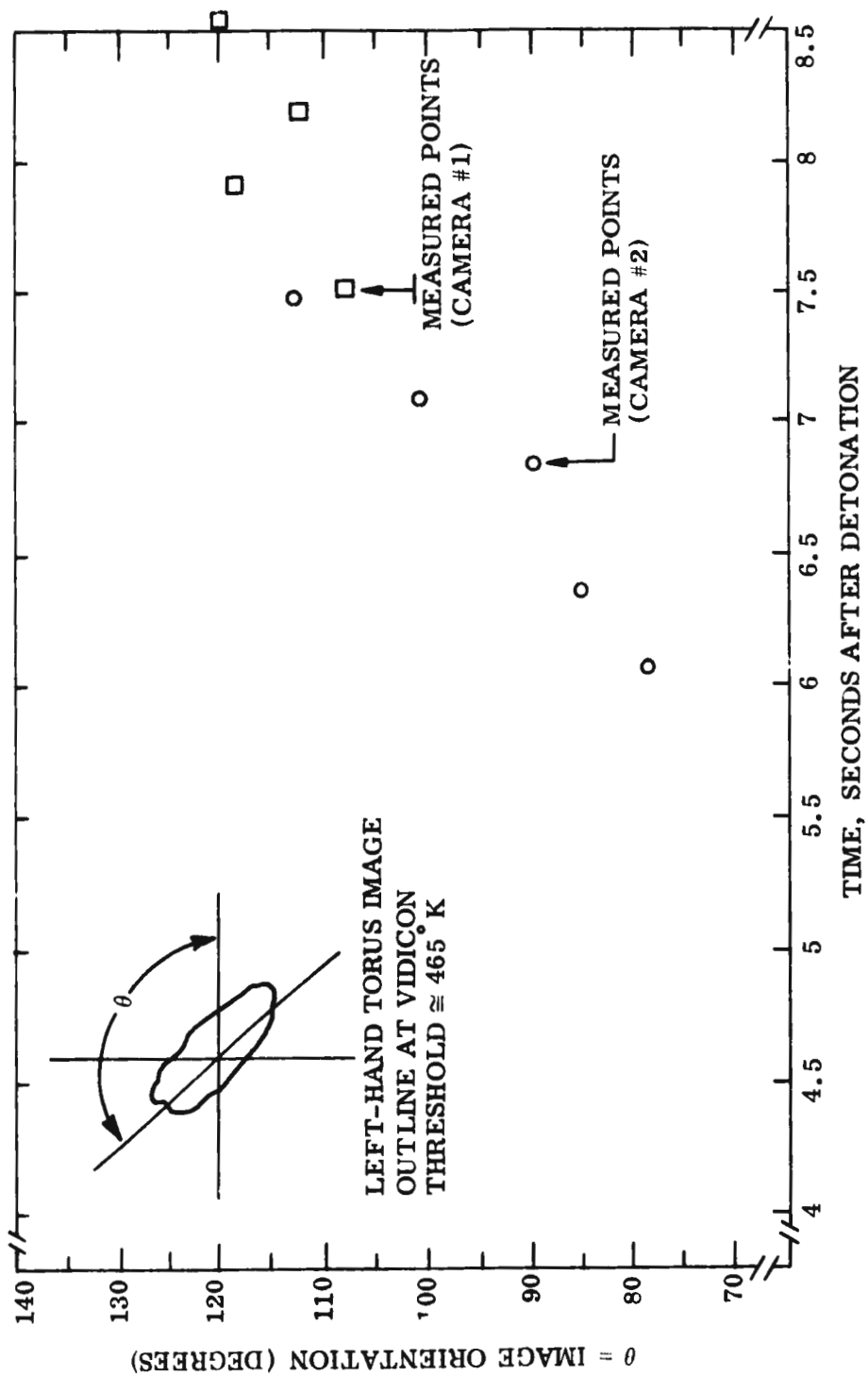


Figure 52. Torus Orientation versus Time - Event MB-4

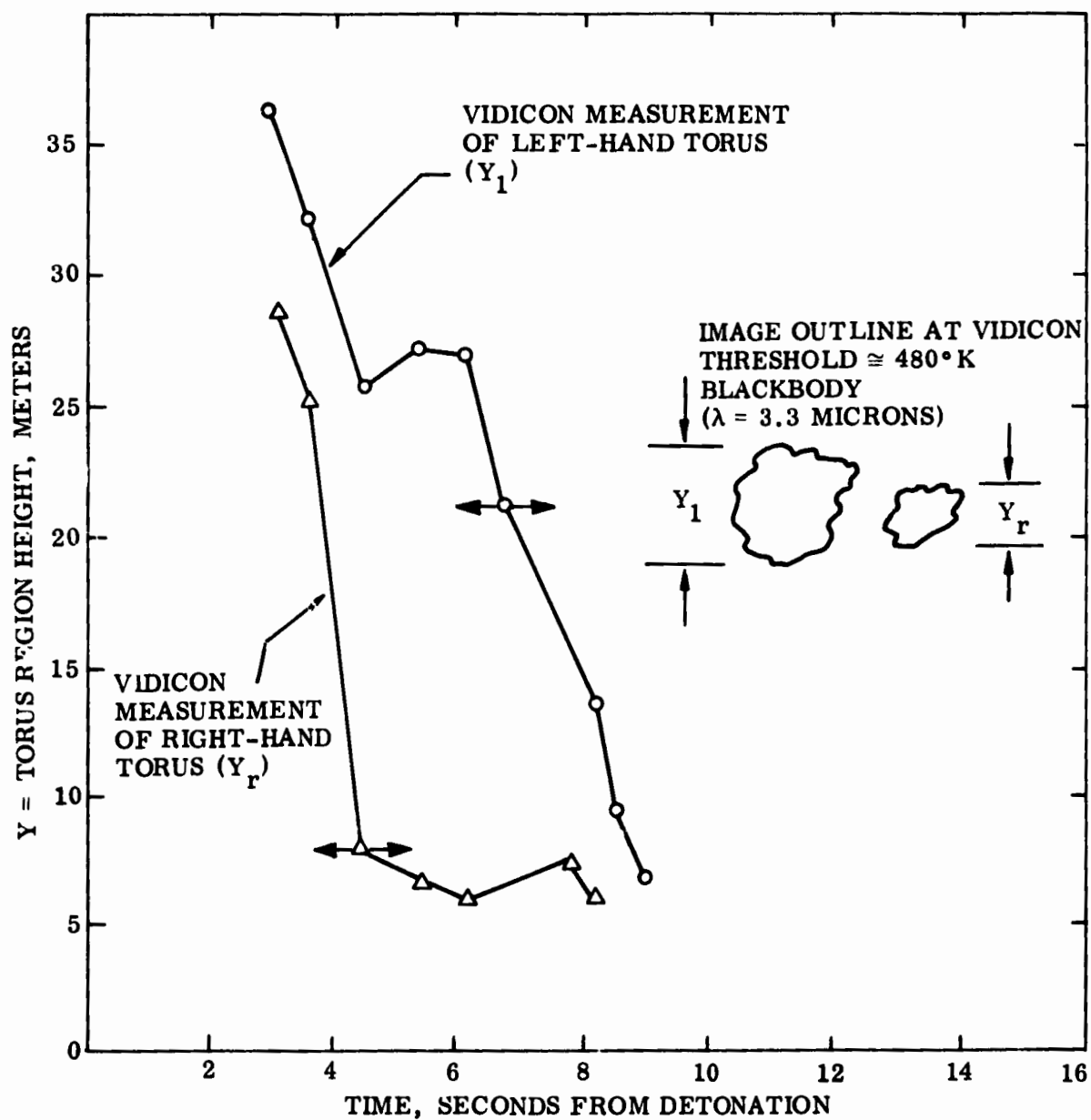


Figure 53. Torus Region Height versus Time - Event MB-4 - Camera 1

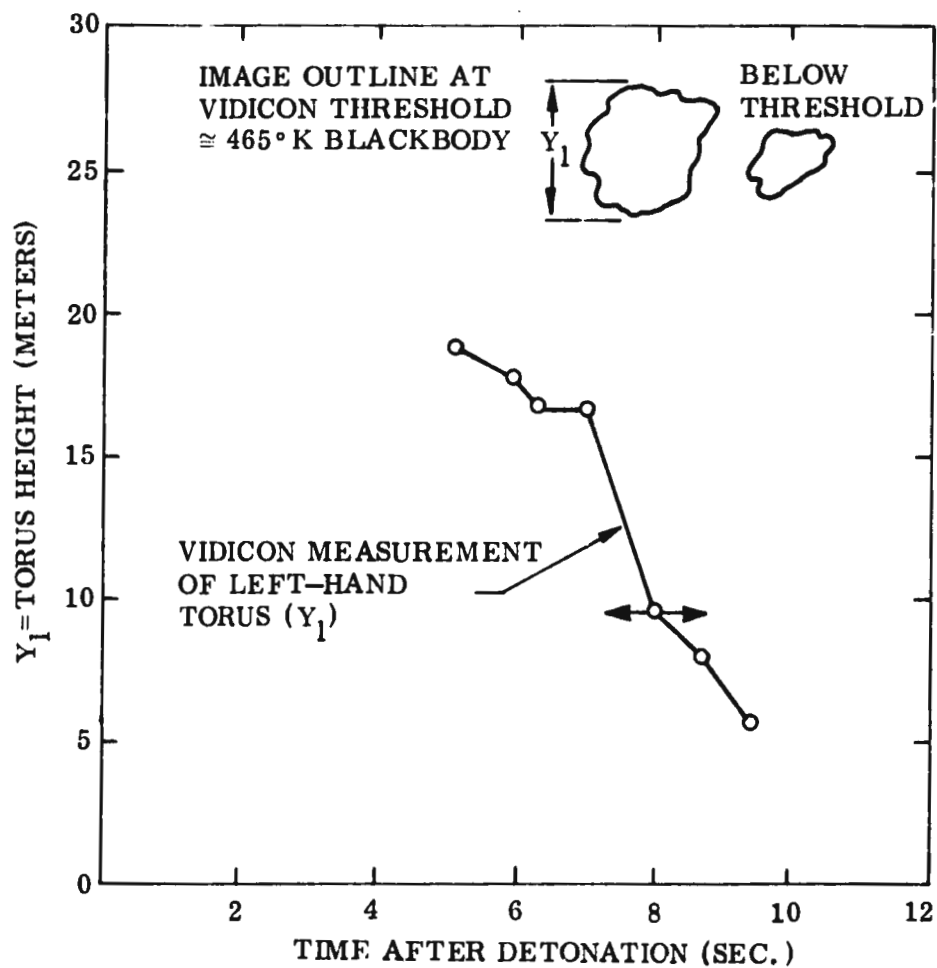


Figure 54. Torus Region Height versus Time - Event MB-4 - Camera 2

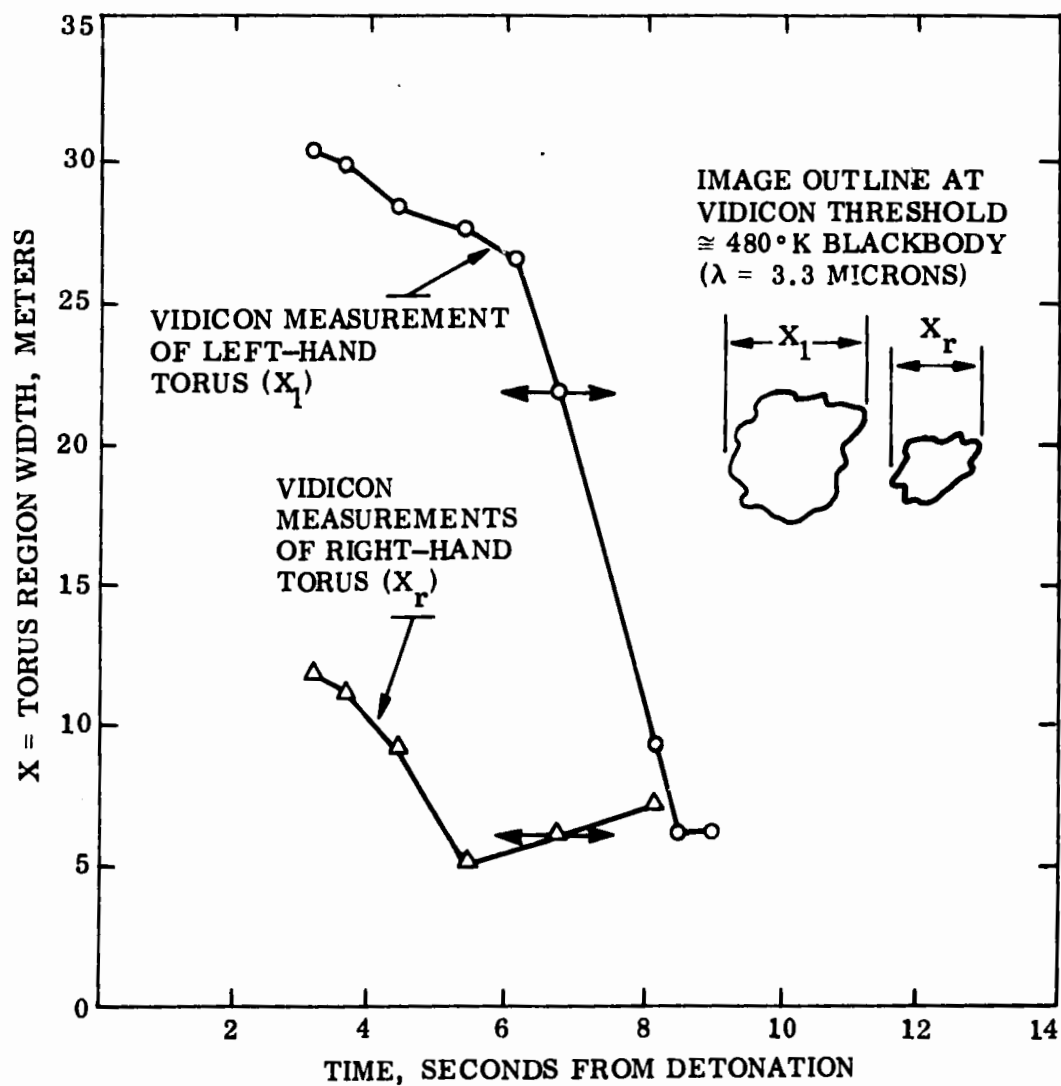


Figure 55. Torus Region Width versus Time - Event MB-4 - Camera 1

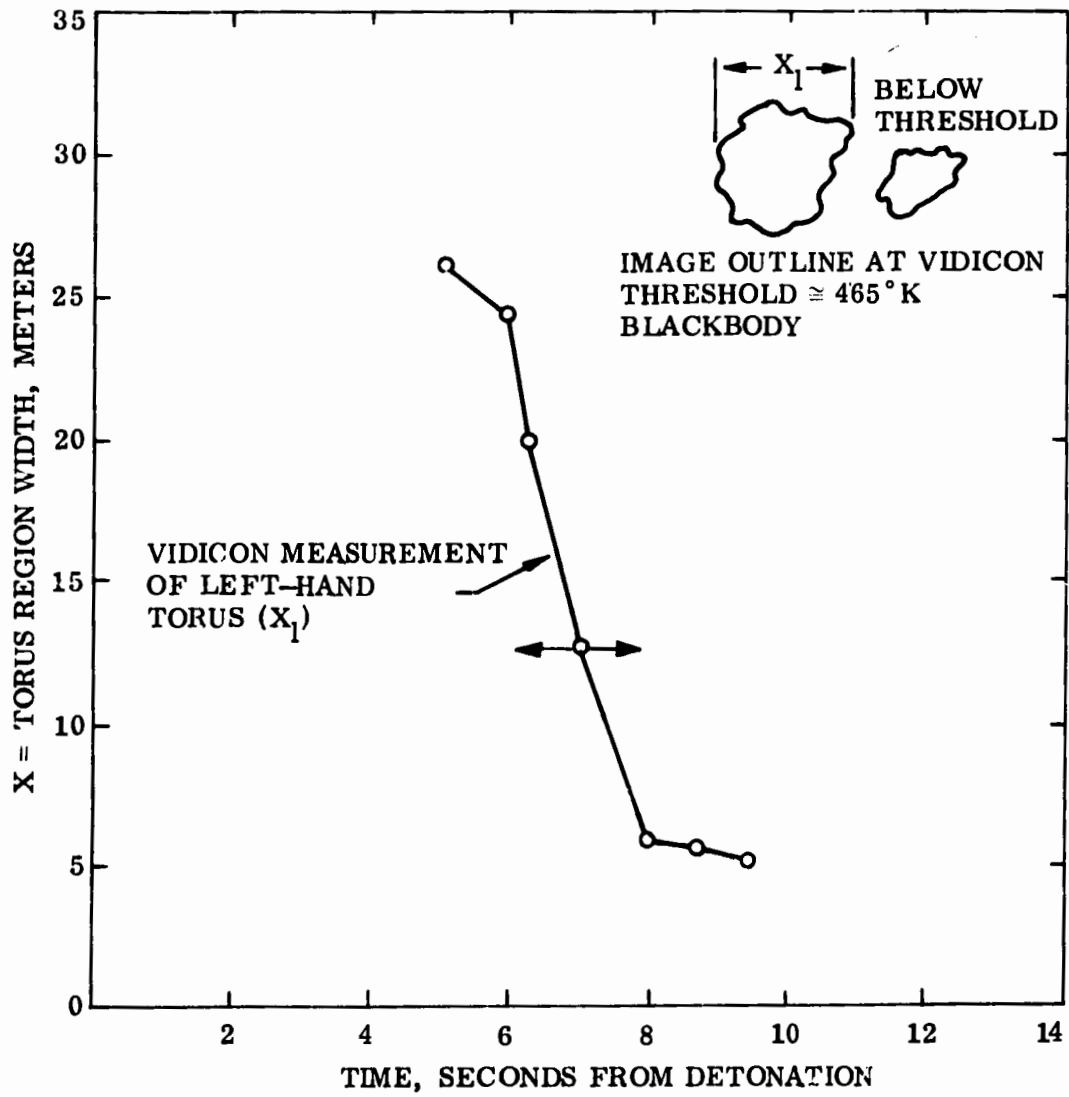


Figure 56. Torus Region Width versus Time - Event MB-4 - Camera 2



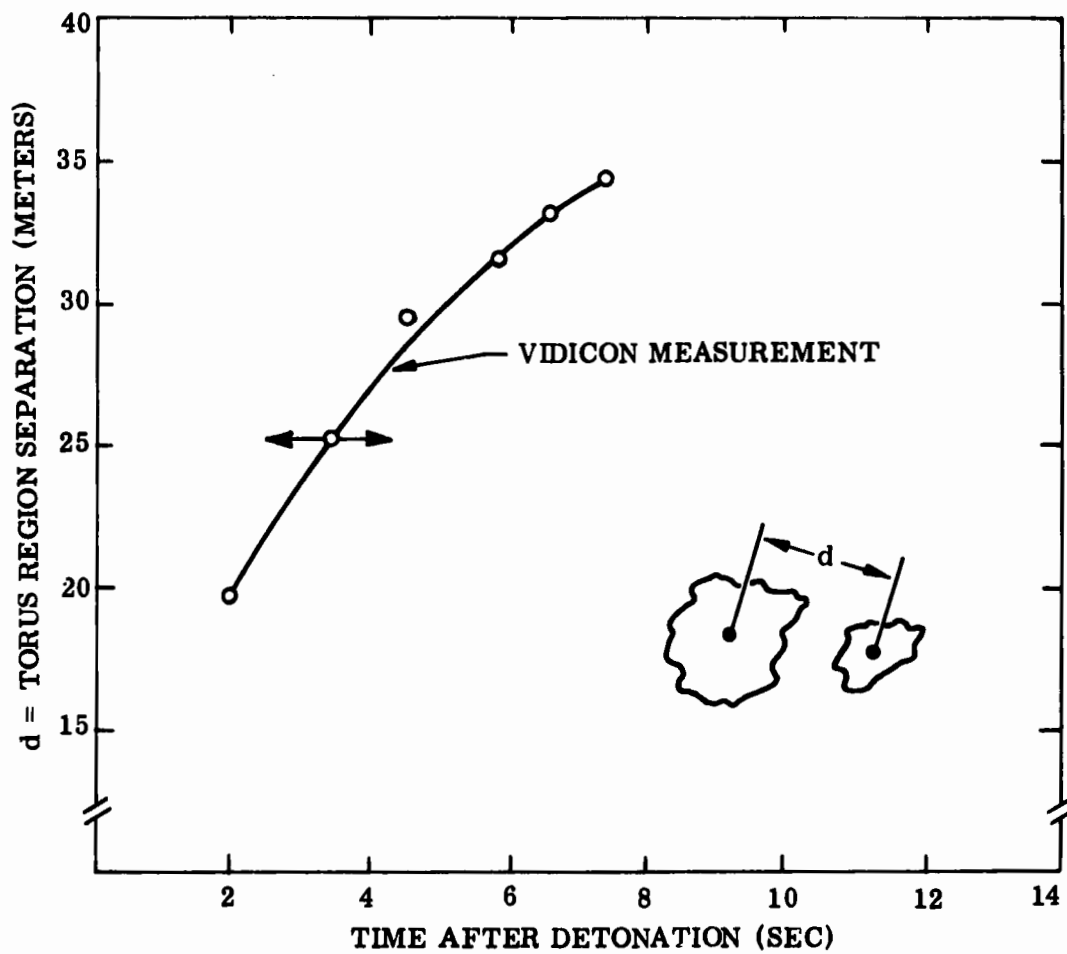


Figure 57. Torus Region Separation versus Time - Event MB-4 - Camera 1

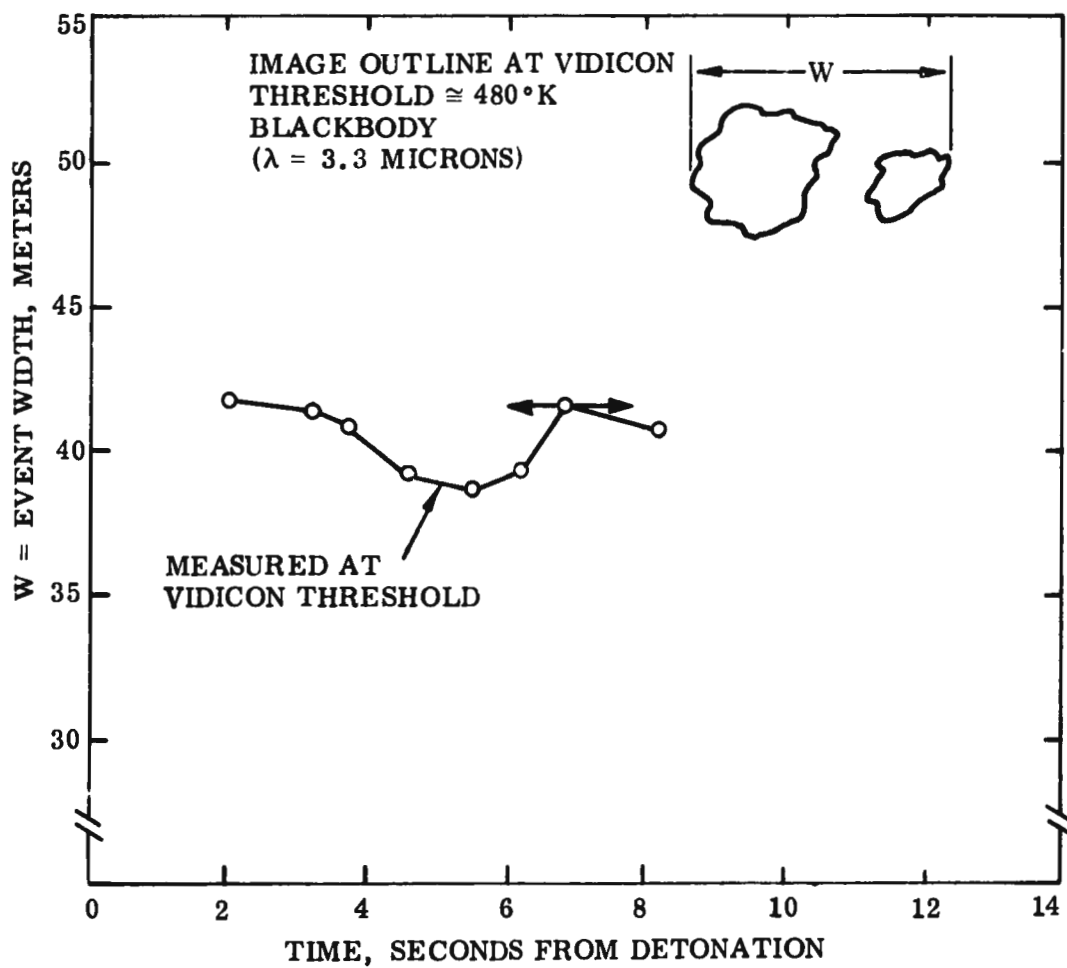


Figure 58. Image Width versus Time - Event MB-4 - Camera 1

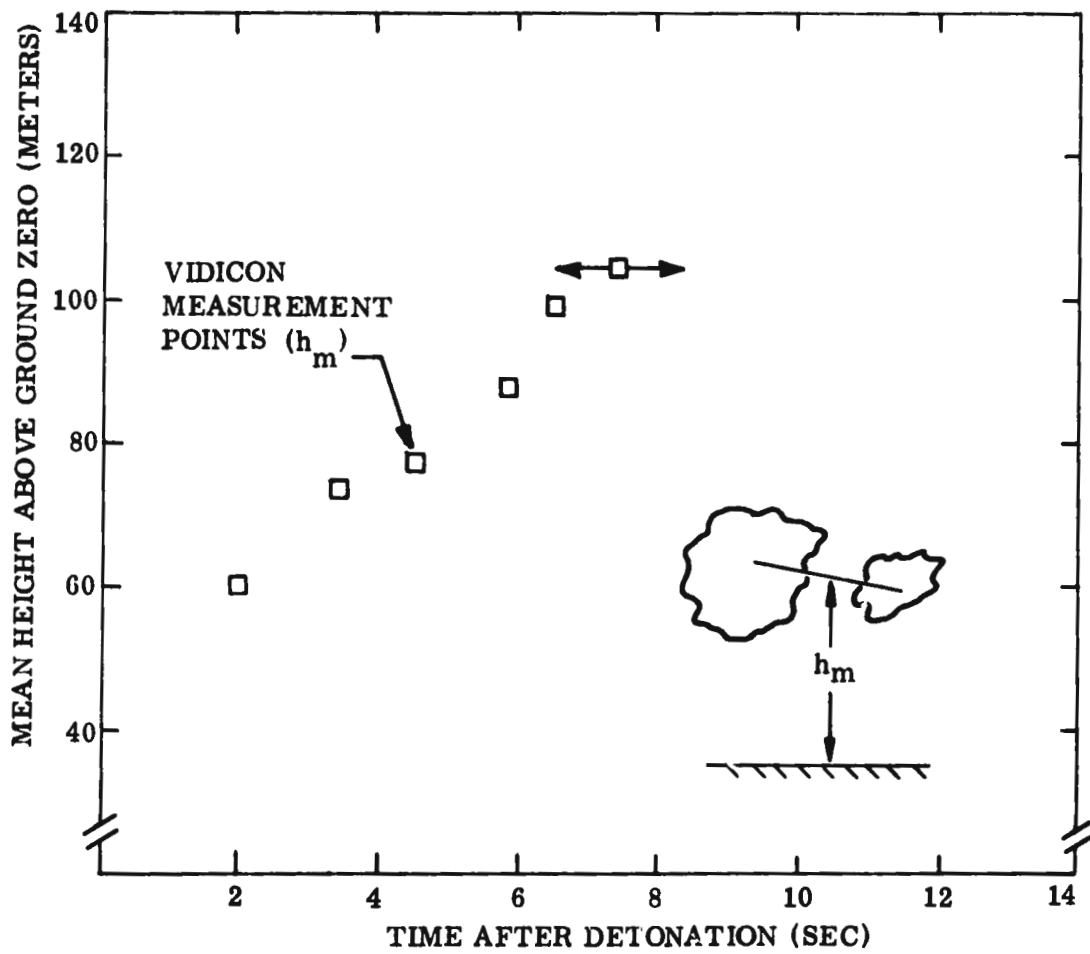


Figure 59. Cloud Mean Altitude versus Time - Event MB-4 - Camera 1

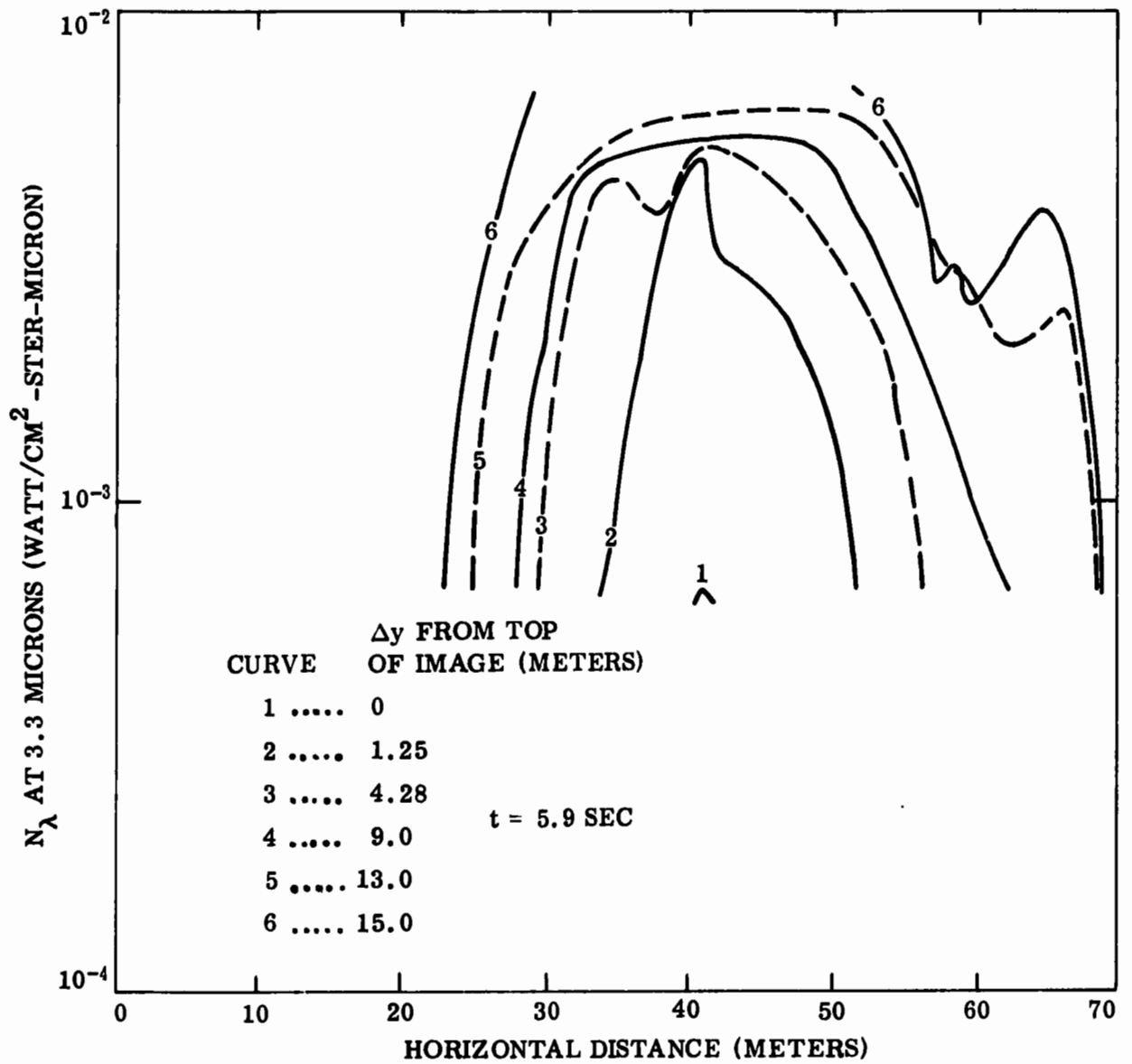


Figure 60. Spectral Radiant Intensity versus Horizontal Distance - Upper Portion of Image - Event MB-4

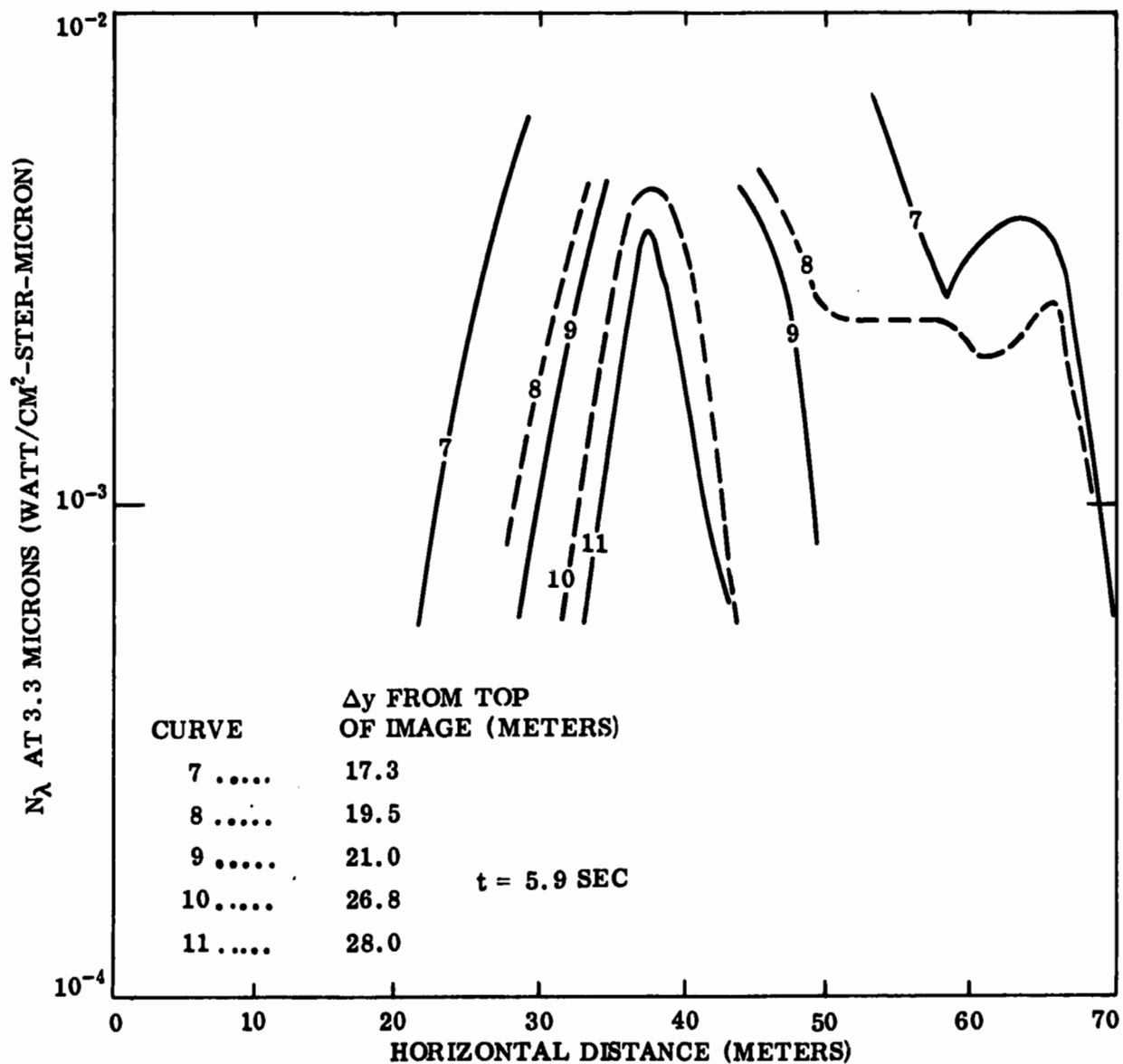


Figure 61. Spectral Radiant Intensity versus Horizontal Distance - Lower Portion of Image - Event MB-4

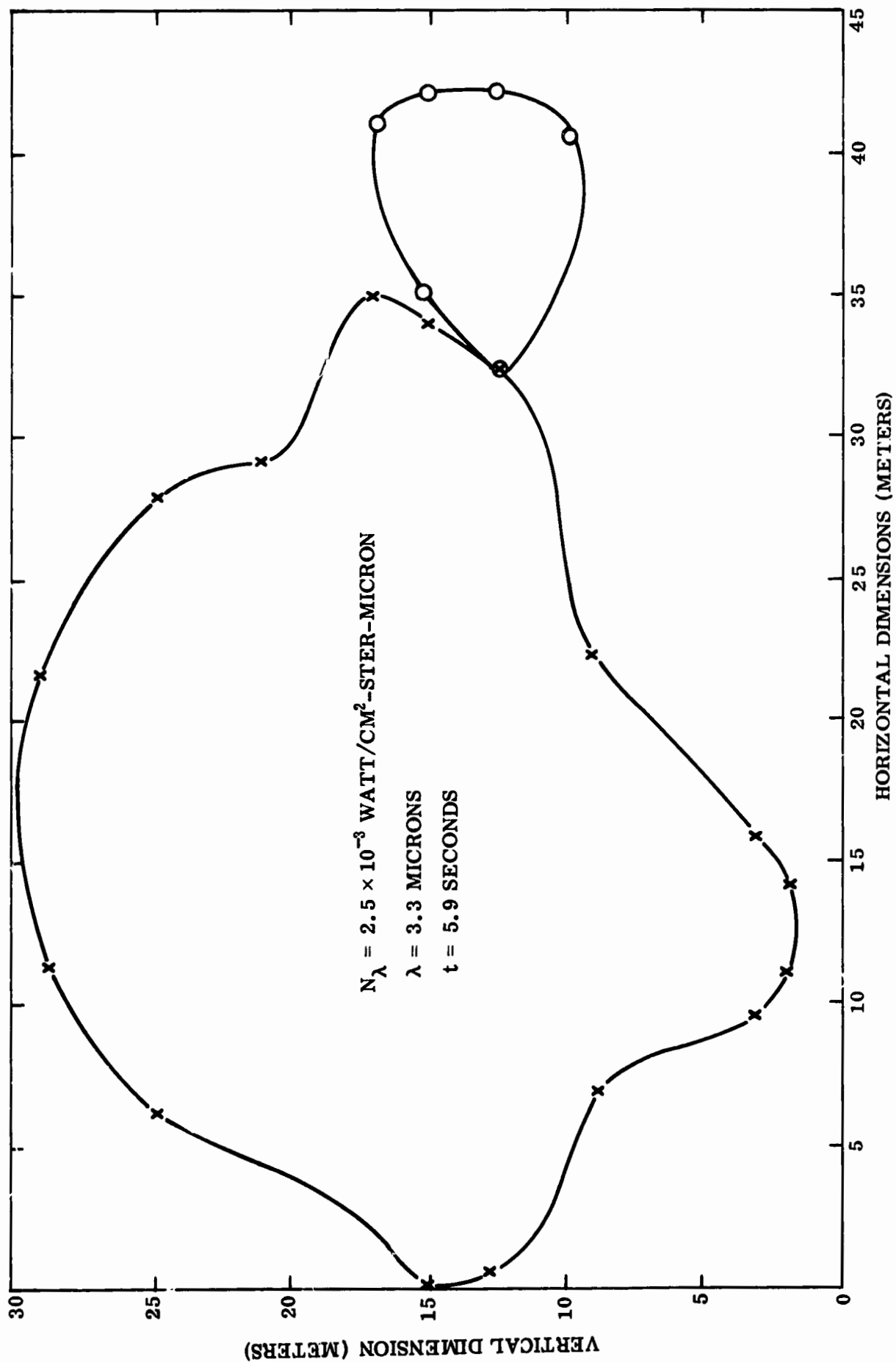


Figure 62. Iso-Intensity Contour - Event MB-4

## 6. AFWL TEST MEASUREMENT RESULTS

In addition to the contractor conducted experiments described above, measurements of air blast time of arrival and pressure history were made by AFWL/DEX.

### a. Time of Arrival Measurements

For each of the MB shots 22 PZT crystals were fielded to obtain the time of arrival of the shock front. Four of these crystals were placed in pockets on the balloon envelope and six were mounted on each of three cables as shown in figure 63.

Balloon Time of Arrival (BTOA) gages were mounted to the surface of the balloon with BTOA-1 being 3 feet, BTOA-2 27 feet 6-3/4 inches, and BTOA-3 and -4 32 feet 0-3/8 inches from the balloon top end fitting. The gages were arranged to be at the apices of a tetrahedron. They were thus 5 meters from the balloon center.

Cable Time of Arrival (CTOA) gages were cable mounted with positions along the cables so determined that distances from the gages to the balloon center were as follows:

CTOA-X.1	12 meters
-X.2	14 meters
-X.3	16 meters
-X.4	18 meters
-X.5	20 meters
-X.6	22 meters

where X = 1, 2, 3 denotes the cable number. These dimensions are valid for shot MB-1 only where the HOB was 150 feet. For shot MB-2 the HOB was 140 feet and for MB-3 and -4 it was 130 feet. The gages were mounted at the same locations on the cables for all of the MB series. Figure 2 lists the locations of the ground ends of the TOA cables with respect to SGZ.

For event DMB-1 four crystals were mounted on each of the two balloons. There were no cable mounted transducers for this event.

Table 4 lists the measured times of arrival of the shock front at each of the TOA crystals. The results of these measurements were, in general, not very satisfactory because of the choice of sensor (PZT ceramic crystal)

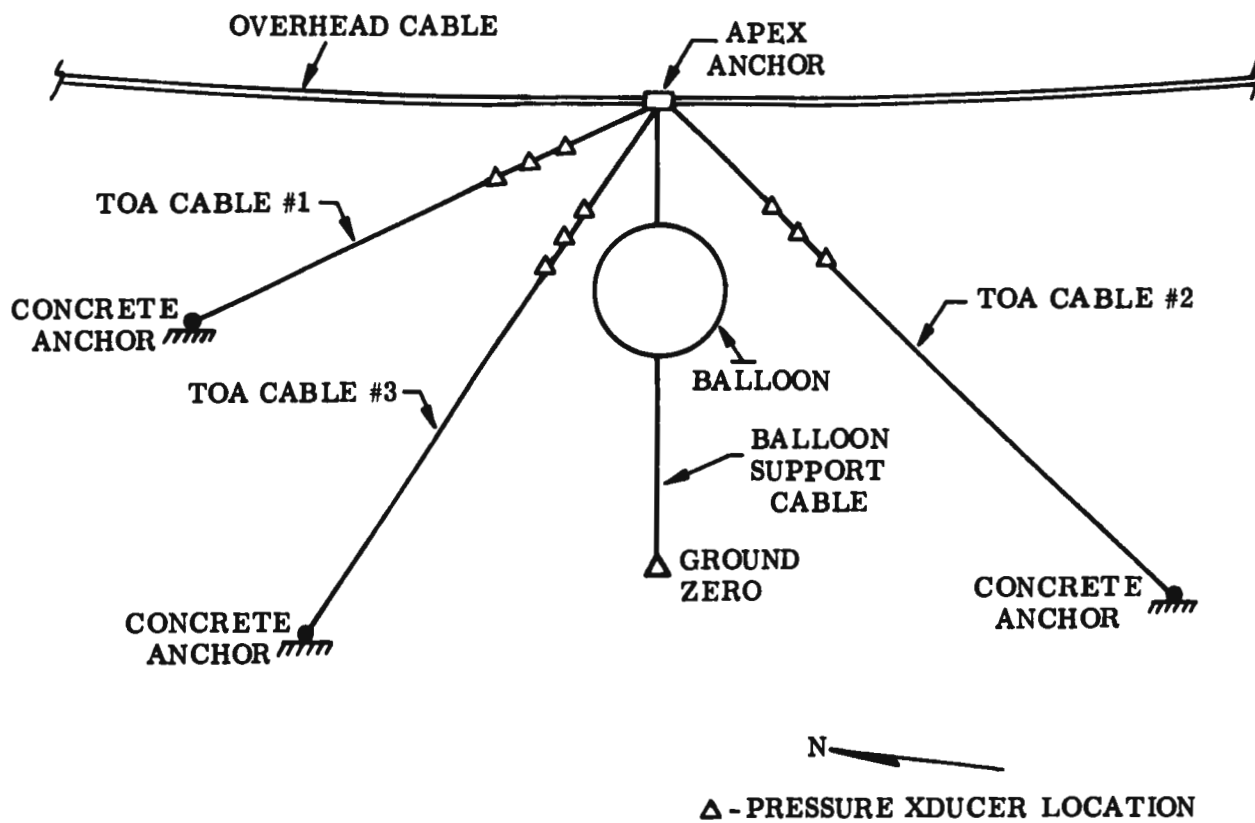


Figure 63. GEST TOA Crystal Deployment Configuration



TABLE 4. GEST TOA DATA

<u>EVENT</u>						
<u>XTAL</u>	<u>MB-1</u>	<u>MB-2</u>	<u>MB-3</u>	<u>MS-4</u>	<u>DMB-1.1</u>	<u>DMB-1.2</u>
BTOA-1	1.993	-	1.773	1.968	-	-
-2	1.938	-	-	1.996	-	1.969
-3	1.912	-	-	-	2.175	-
-4	-	1.890	2.098	1.997	-	1.938
CTOA-1.1	-	-	-	-	NOT INSTRUMENTED	
-1.2	-	-	16.951	17.175		
-1.3	-	-	19.035	19.460		
-1.4	-	-	21.979	-		
-1.5	-	-	25.245	25.358		
-1.6	-	-	29.096	29.071		
CTOA-2.1	-	-	-	-		
-2.2	-	16.130	14.685	13.631		
-2.3	-	19.130	17.046	15.761		
-2.4	-	22.726	19.691	18.280		
-2.5	-	26.410	22.868	24.322		
-2.6	-	30.762	26.743	25.134		
CTOA-3.1	9.55	-	-	-		
-3.2	13.78	-	14.691	-		
-3.3	-	-	17.525	-		
-3.4	-	-	20.883	-		
-3.5	-	-	24.466	-		
-3.6	-	-	-	-	NOT INSTRUMENTED	

and its mounting arrangement. Crystal outputs tended to be lower than desirable for accurate measurement. The times presented are time intervals between FIDU pulse and TOA pulse in milliseconds.

b. Air Blast Pressure Measurements

Ten Kulite XT Series, integrated-sensor, Q type pressure transducers were fielded on each of the MB events. Nine of these were mounted on the TOA cables as shown in figure 64; one was located at surface ground zero.

For the DMB-1 event twelve pressure transducers were mounted at ground level in the configuration shown in figure 65. Pressure-time histories from these gages are shown in figures 66 through 77.

At this writing the pressure measurement data has not been analyzed.

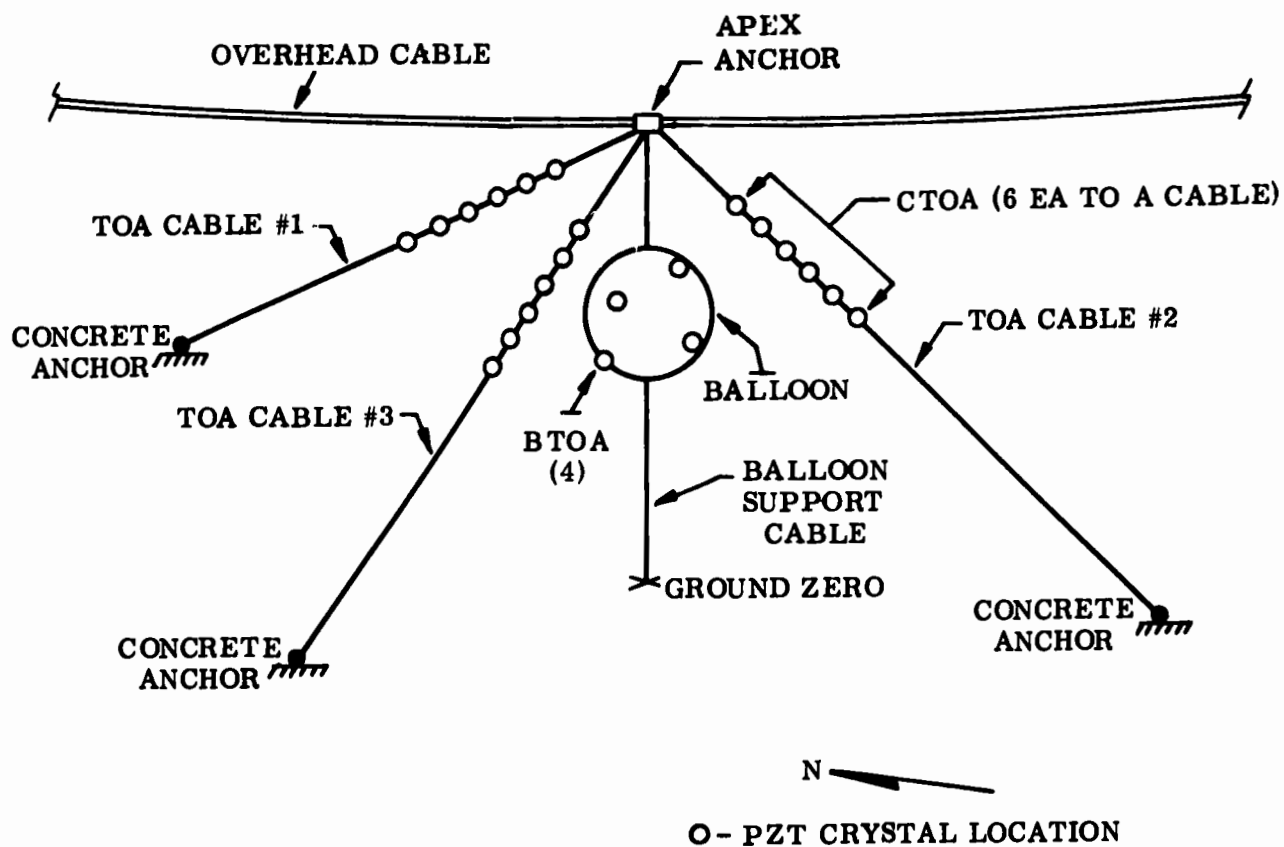
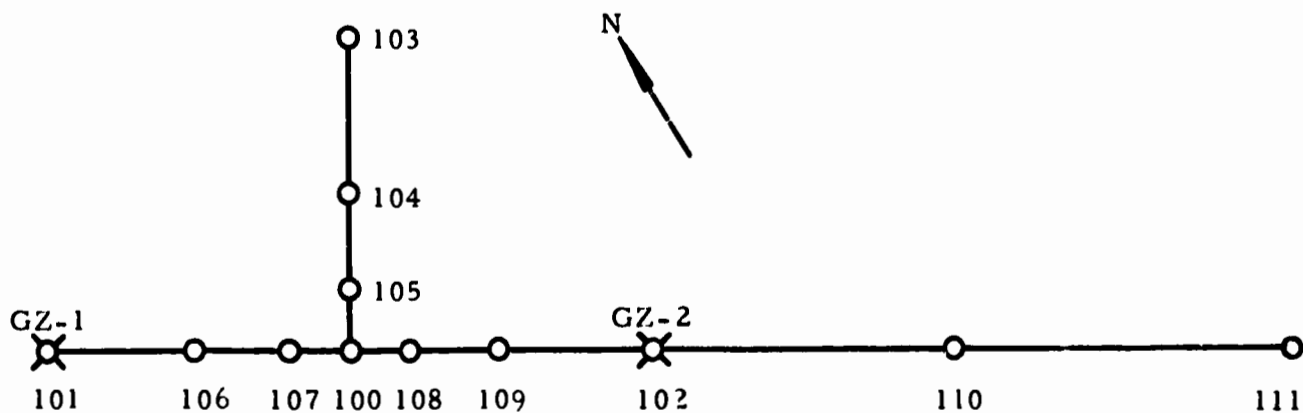


Figure 64. GEST Pressure Gage Deployment Configuration - MB Series



MEASUREMENT NO.	RANGE (FT)	GAGE RANGE (PSI)
100	0	100
101	50	50
102	50	50
103	50 ⊥	10
104	25 ⊥	100
105	10 ⊥	100
106	25	50
107	10	100
108	10	100
109	25	50
110	100	10
111	200	10

Figure 65. GEST Event DMB-1 Blast Pressure Gage Layout

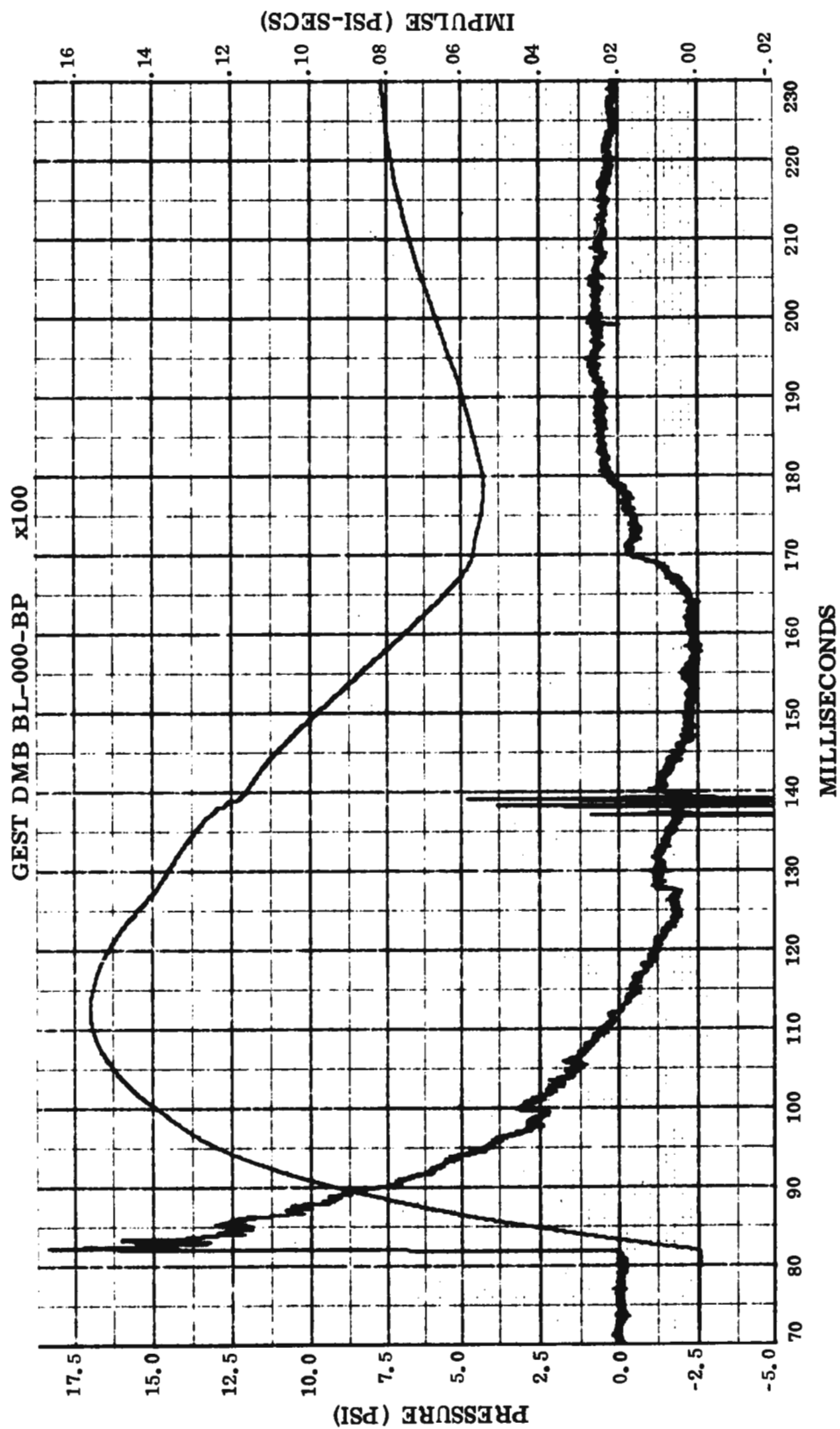


Figure 66. GEST DMB-1 Pressure Measurement 100

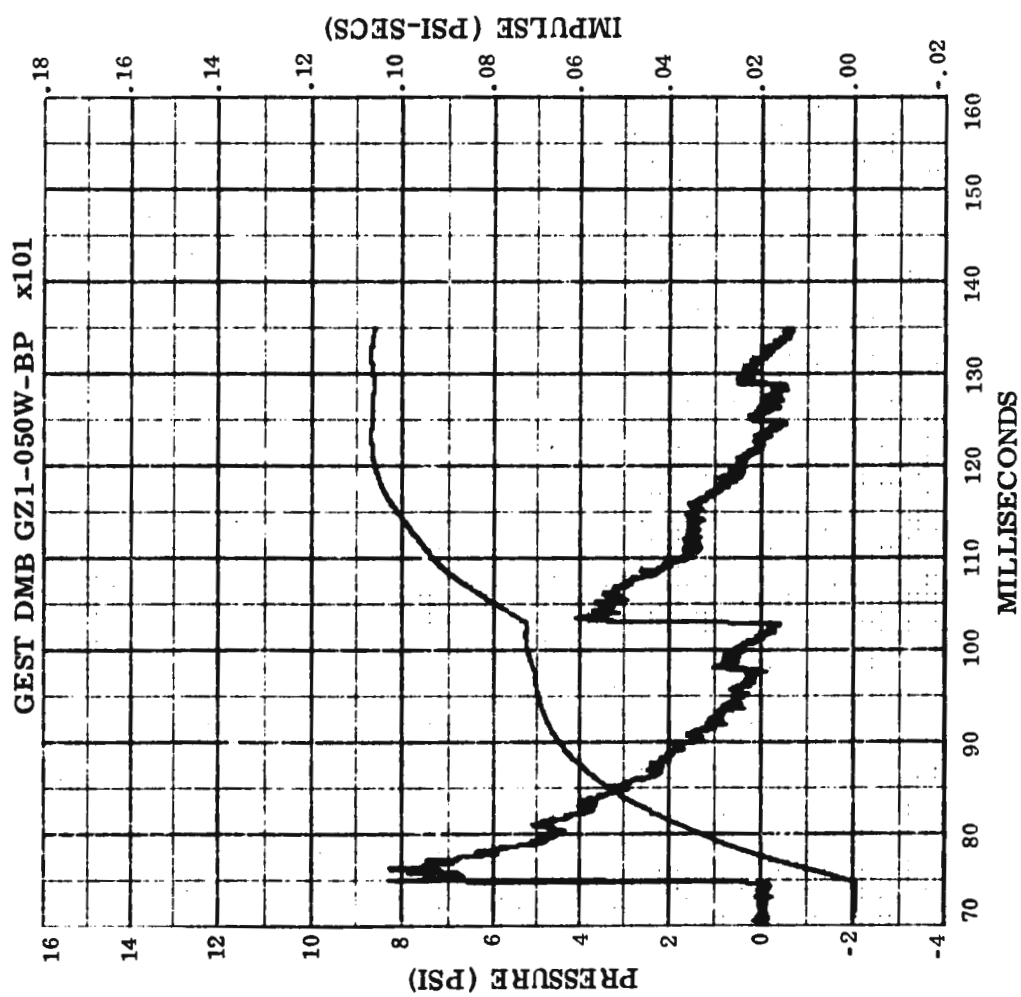


Figure 67. GEST DMB-1 Pressure Measurement 101

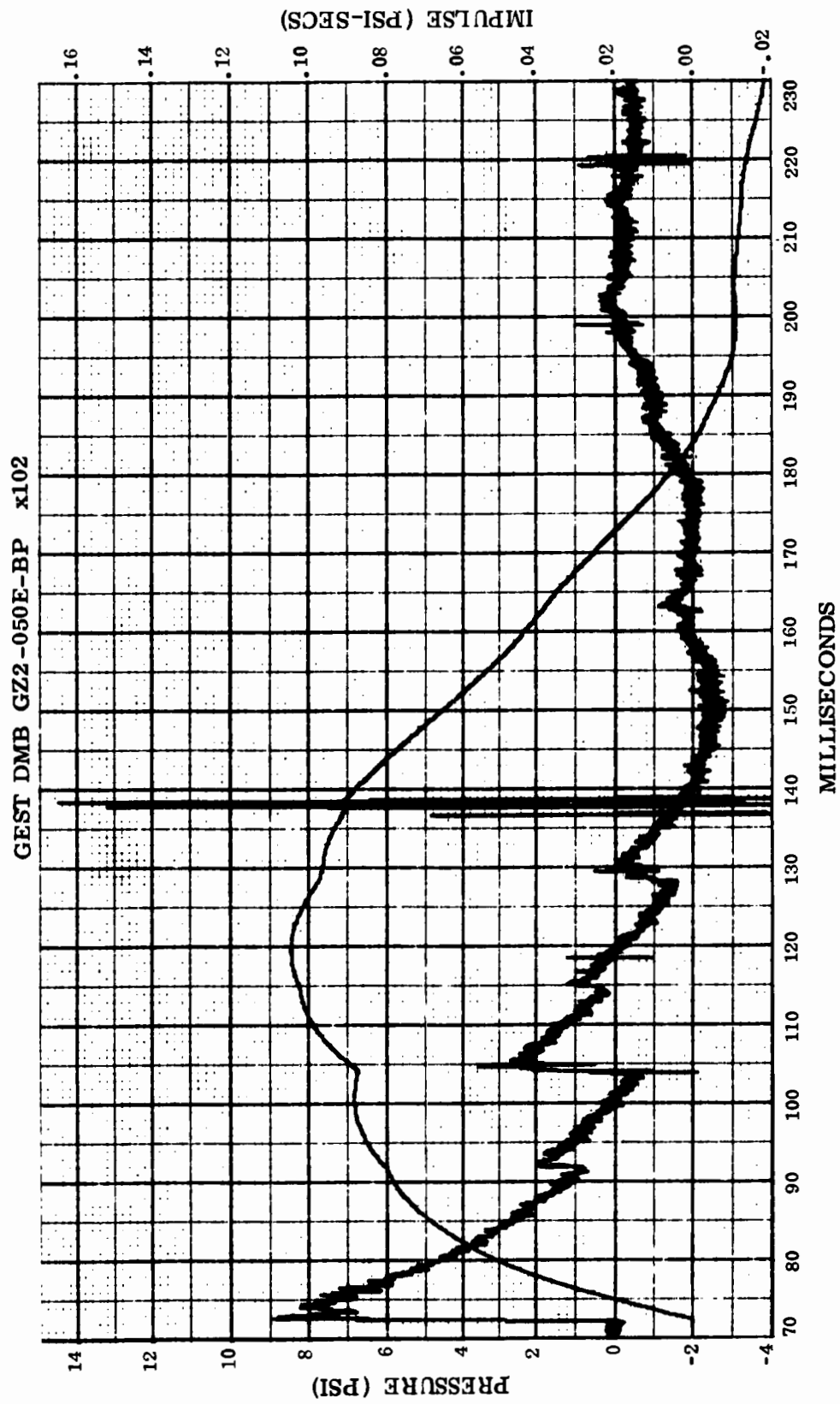


Figure 68. GEST DMB-1 Pressure Measurement 102

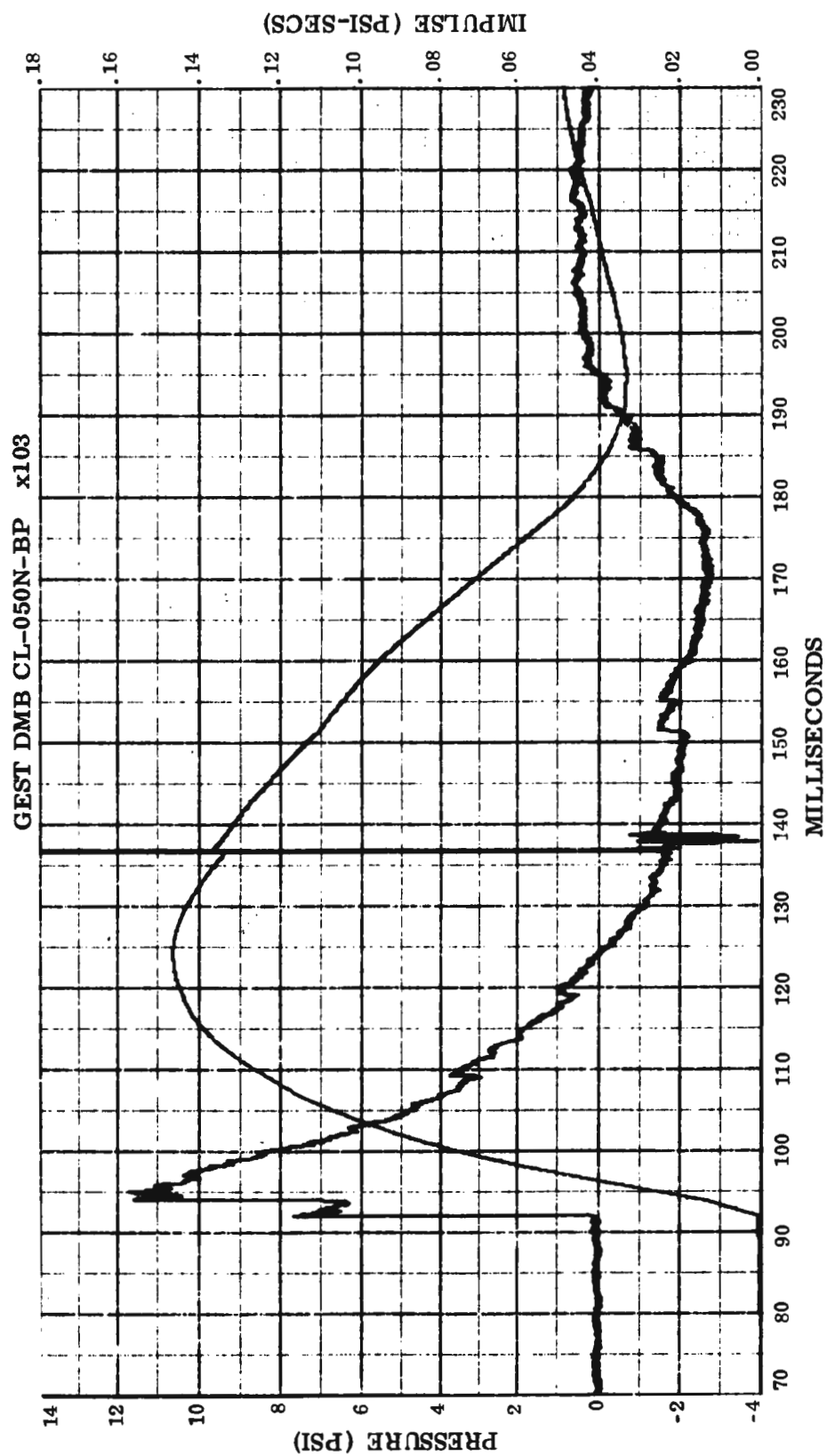


Figure 69. GEST DMB-1 Pressure Measurement 103



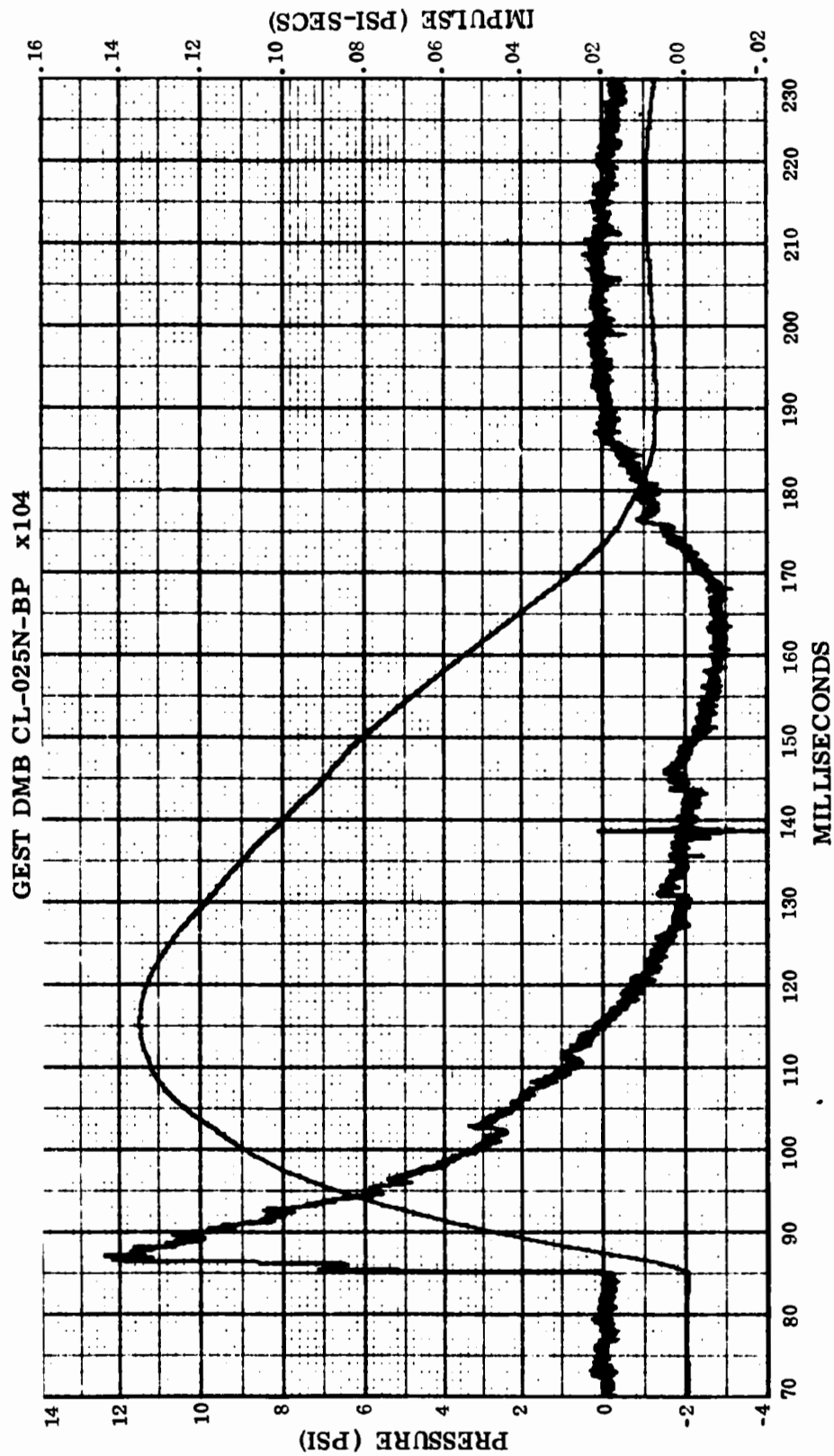


Figure 70. GEST DMB-1 Pressure Measurement 104

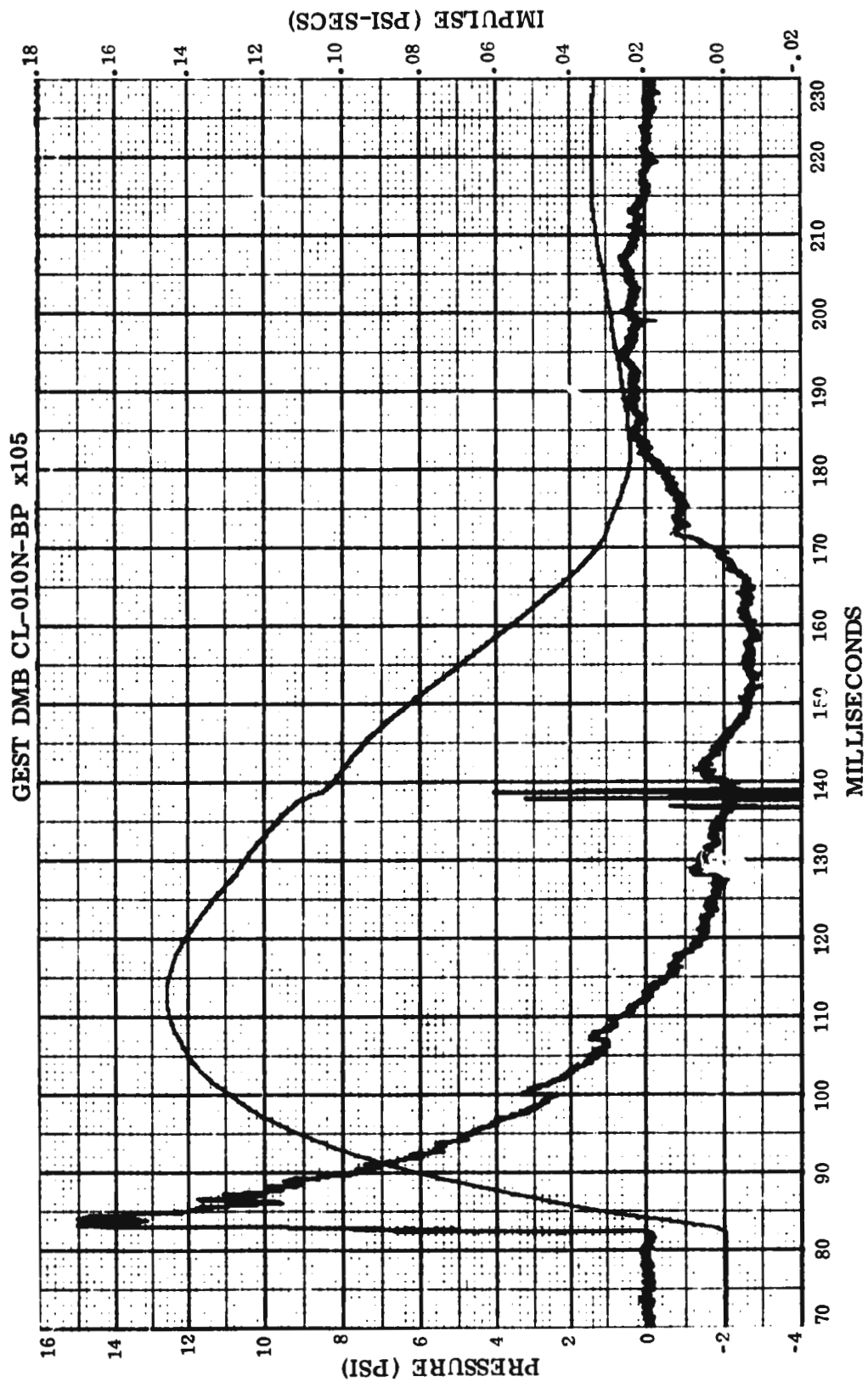


Figure 71. GEST DMB-1 Pressure Measurement 105

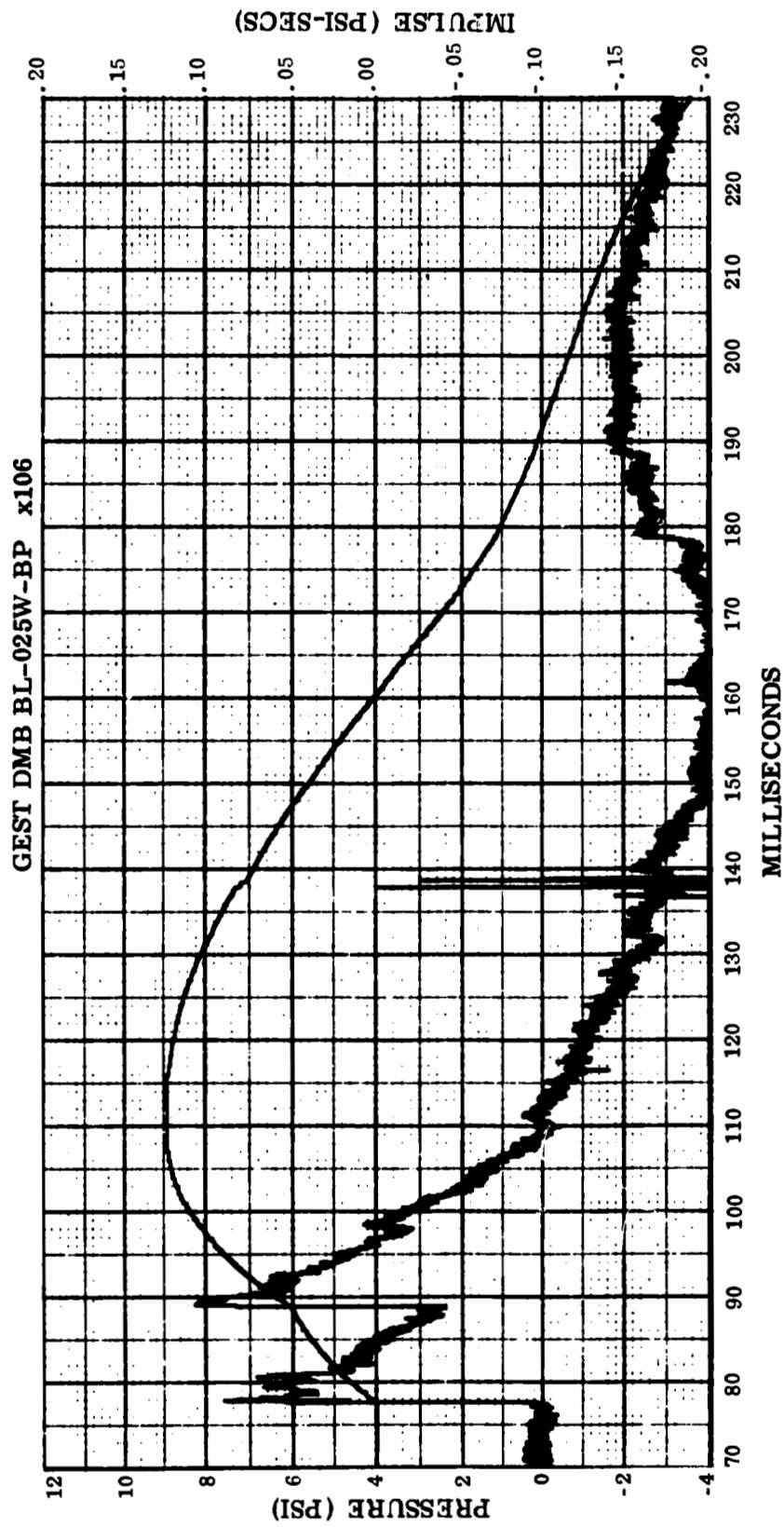


Figure 72. GEST DMB-1 Pressure Measurement 106

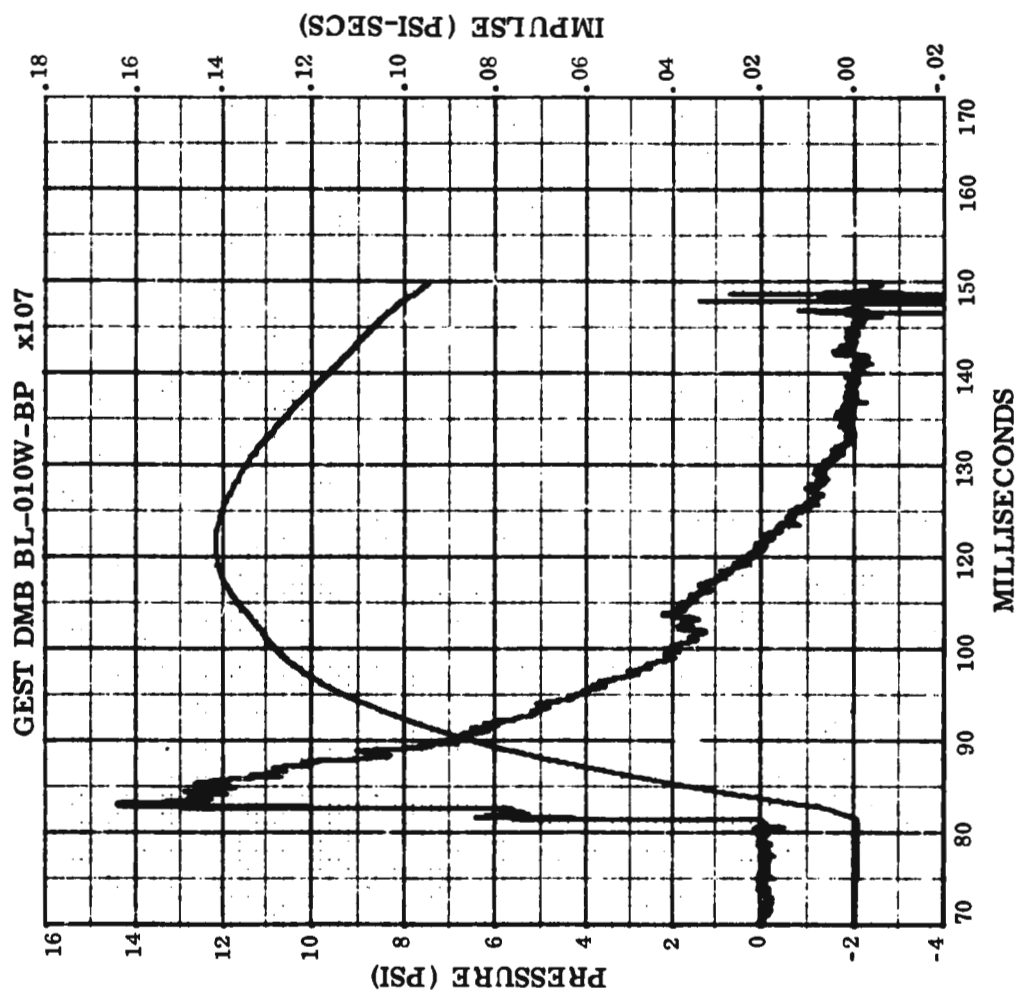


Figure 73. GEST DMB-1 Pressure Measurement 107

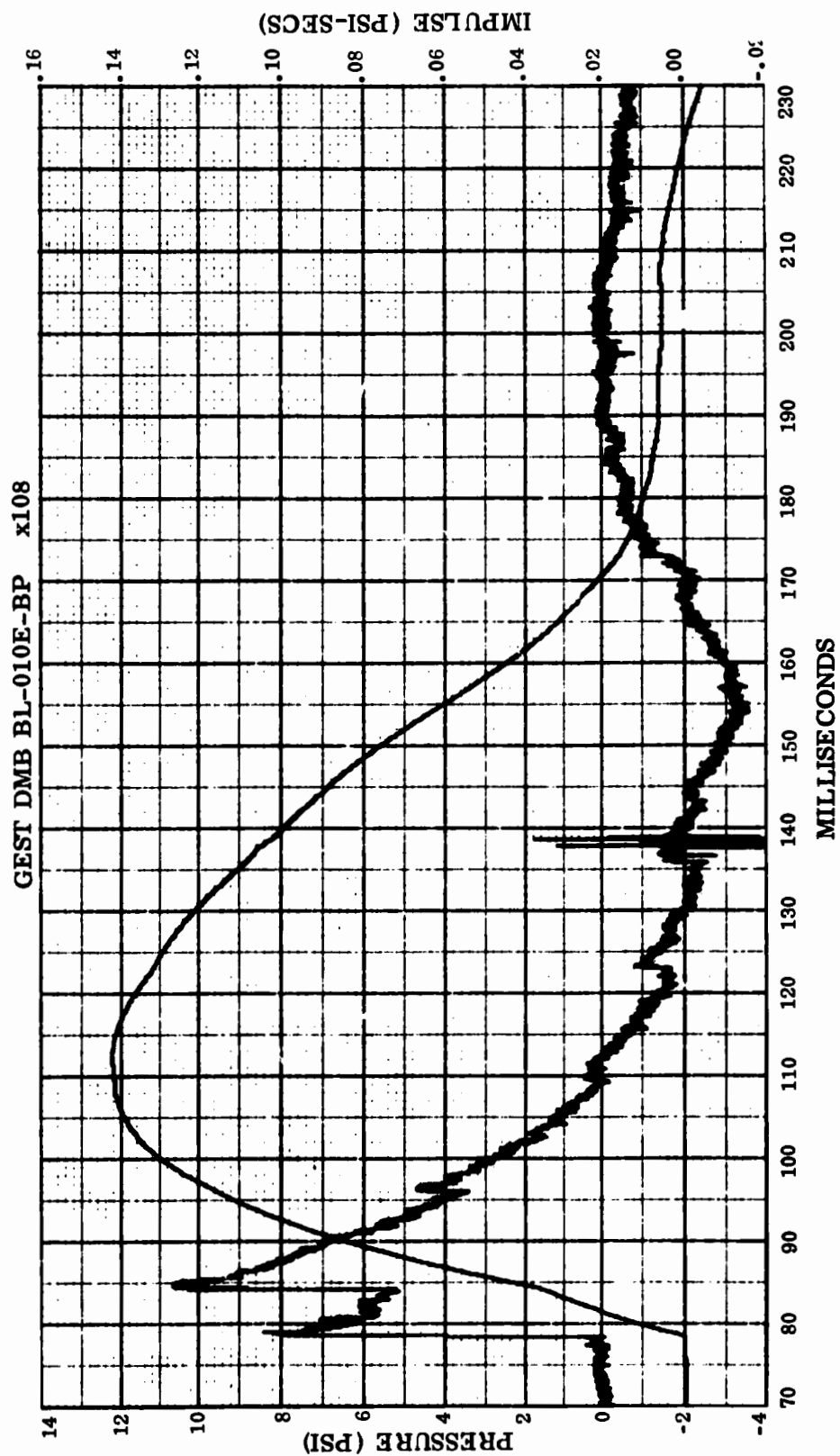


Figure 74. GEST DMB-1 Pressure Measurement 108

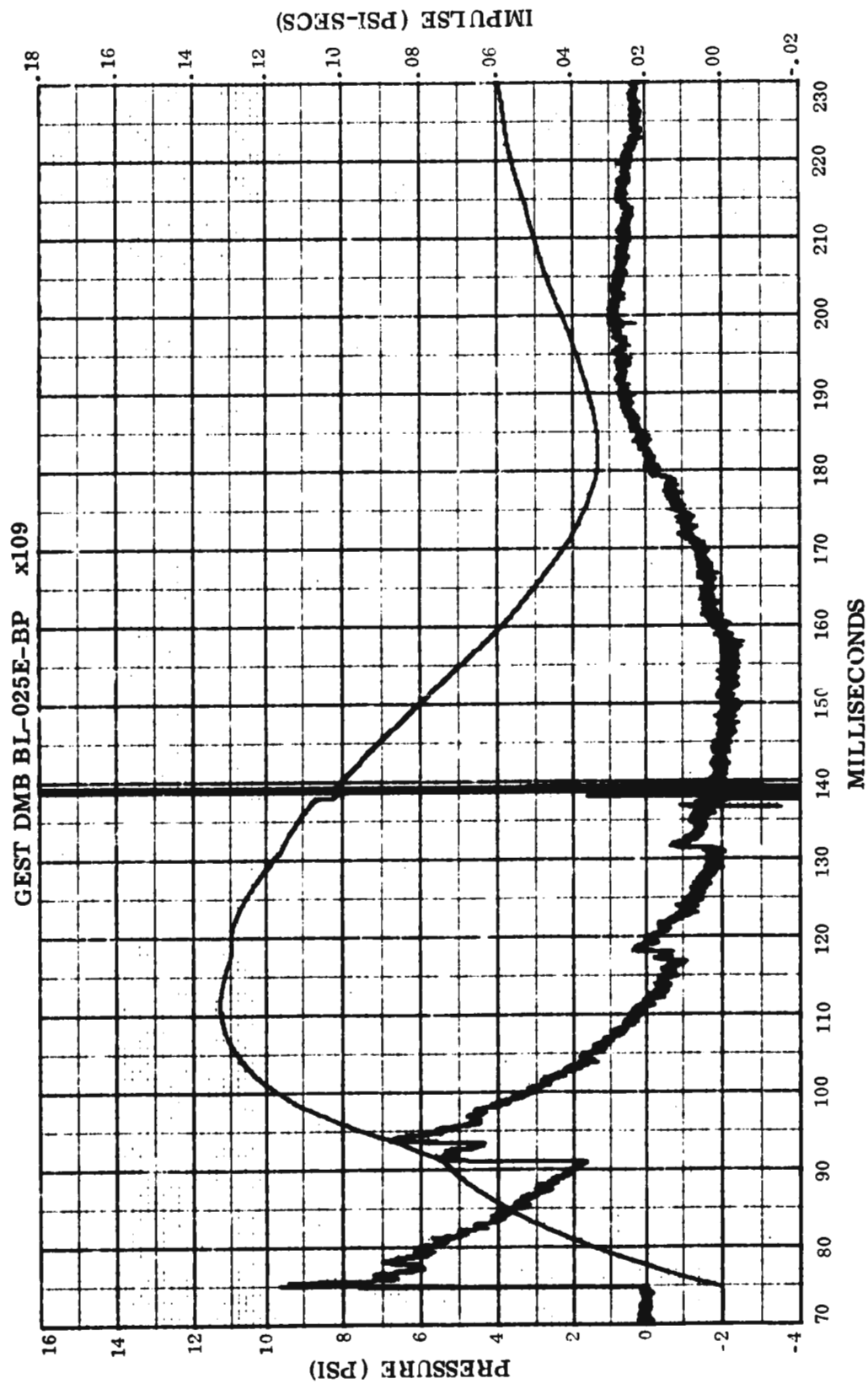


Figure 75. GEST DMB-1 Pressure Measurement 109

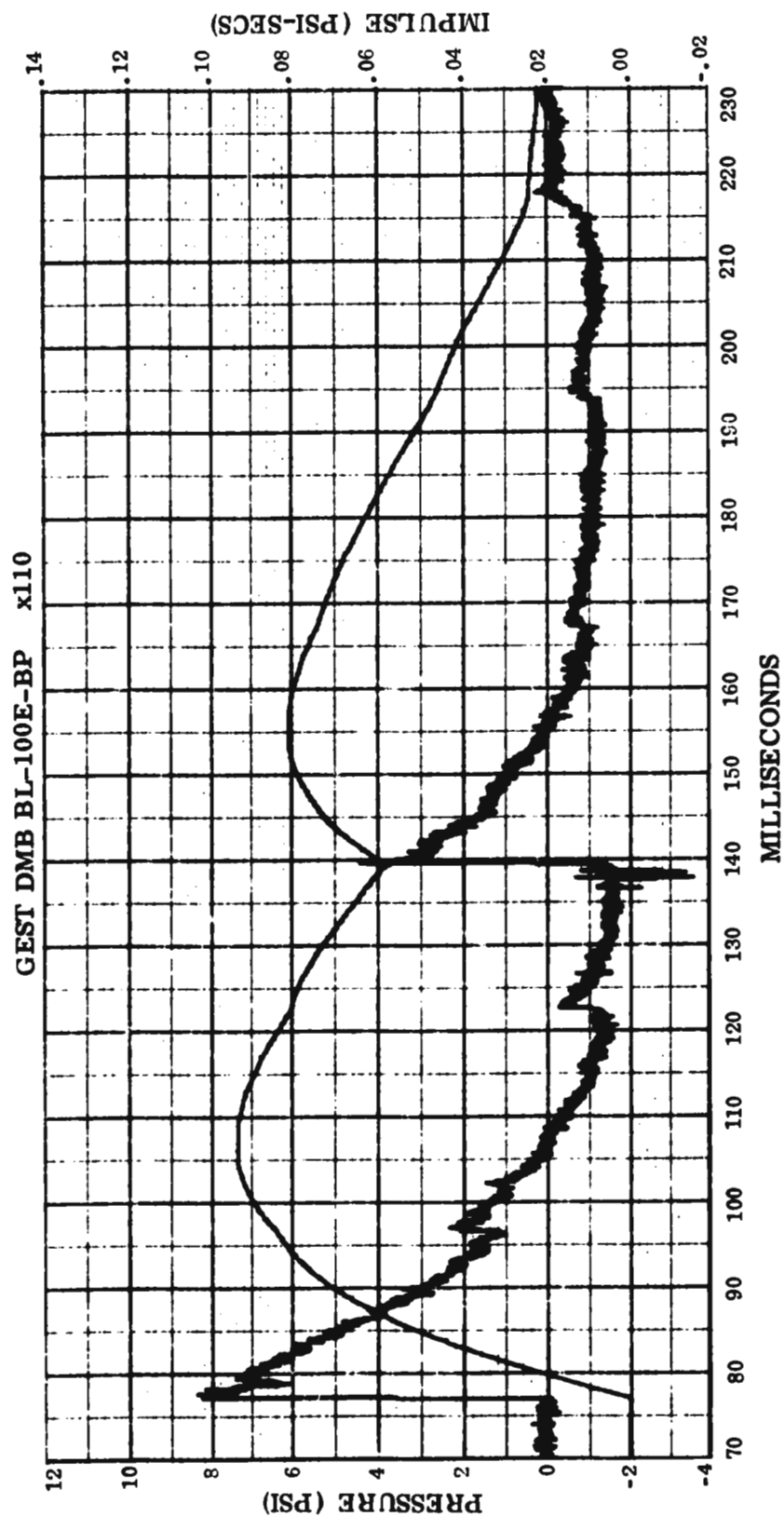


Figure 76. GEST DMB-1 Pressure Measurement 110

GEST DMB BL-200E-BP x111

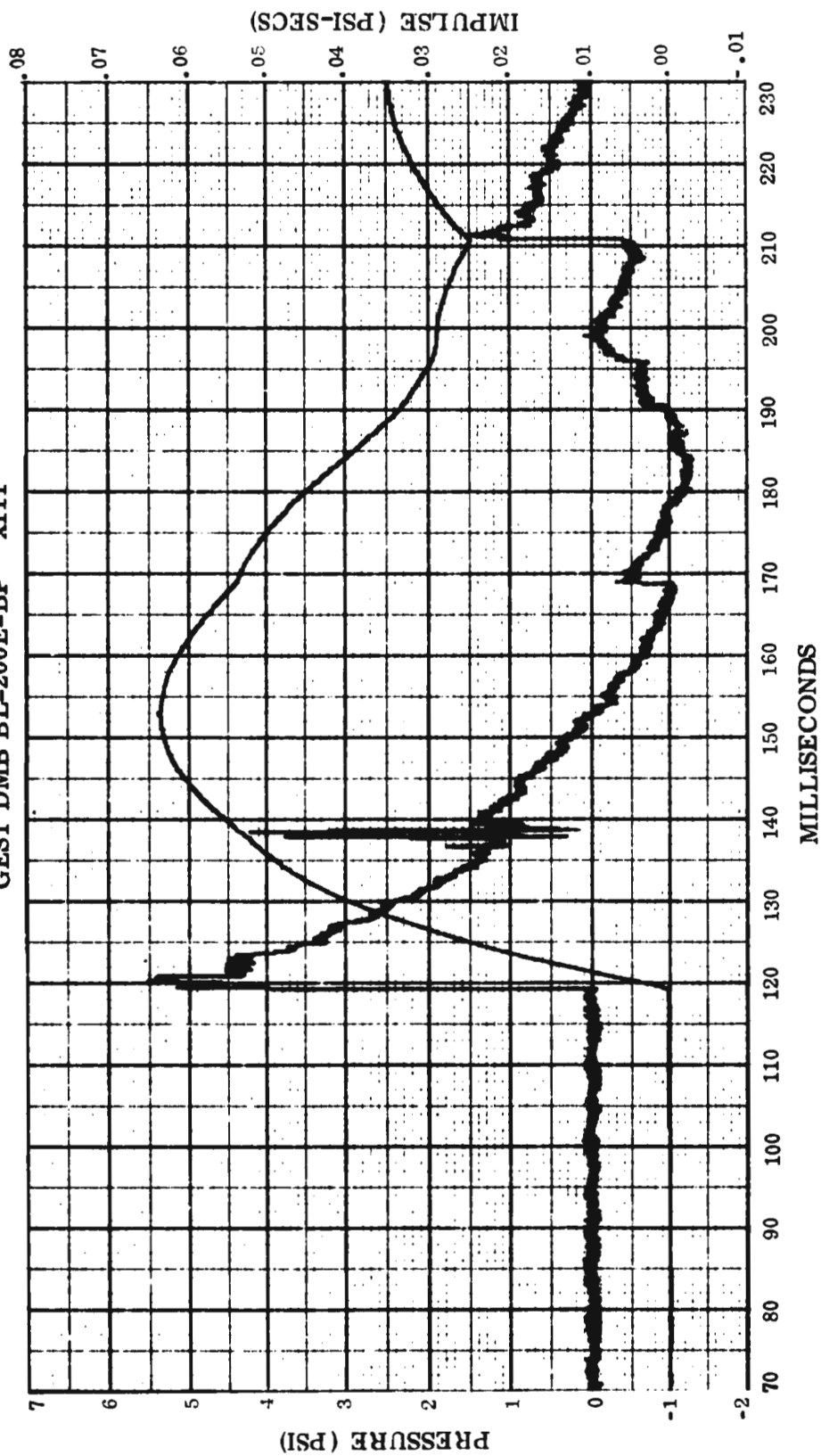


Figure 77. GEST DMB-1 Pressure Measurement 111



## SECTION V

### DISCUSSION OF RESULTS

Generally good results were obtained with the GEST series of balloon explosions. There were the usual experimental difficulties such as loss of the Raman scattering experiment and the failure to place the required quantity of methane in one of the DMB-1 balloons. This latter failure precluded verification of the HULL prediction that the two tori would interact to form a single larger one.

Hot wire anemometry data obtained in the test series can be used to obtain temperature, temperature gradients, temperature fluctuations, velocity, velocity gradients, and velocity fluctuations for comparison with HULL calculations. From the fluctuation data turbulence information can be derived. An approximate value for the ratio  $T_{\text{fluct}}/T_{\text{mean}}$  was determined for the GEST shots to be 0.3. This is important in that it implies that the temperature gradients calculated by a laminar code such as HULL would not be significantly reduced by the inclusion of turbulence.

Preliminary study of the turbulence information yields an estimate of 0.4 seconds for the dissipation time and about 4 meters for the integral scale. Although preliminary, these figures reflect the sort of information obtainable from GEST type events. Figure 78 is the power spectrum derived from one of the TRW hot wire measurements. The straightline fit over much of the frequency range has a slope of  $-5/3$ . That this slope corresponds to that expected in the inertial subrange for isotropic turbulence is reassuring and tends to reinforce confidence in the validity of the data.

The TRW data showed typical values of  $15^\circ \text{C/cm}$  for the temperature gradients at the fireball leading edges and  $0.5^\circ \text{C/cm}$  at the trailing edges. The GEST type detonation with its high temperature gradients appears to offer a useful tool for the study of fireball radar clutter and its origin.

One of the prime reasons for carrying out the GEST series of shots was that it would give data which could be used to verify the accuracy of the HULL code for the prediction of fireball and related phenomenology. Preliminary analysis of the data indicates that the HULL code is a useful tool in this regard. Temperatures, temperature gradients, torus formation rates, etc. as

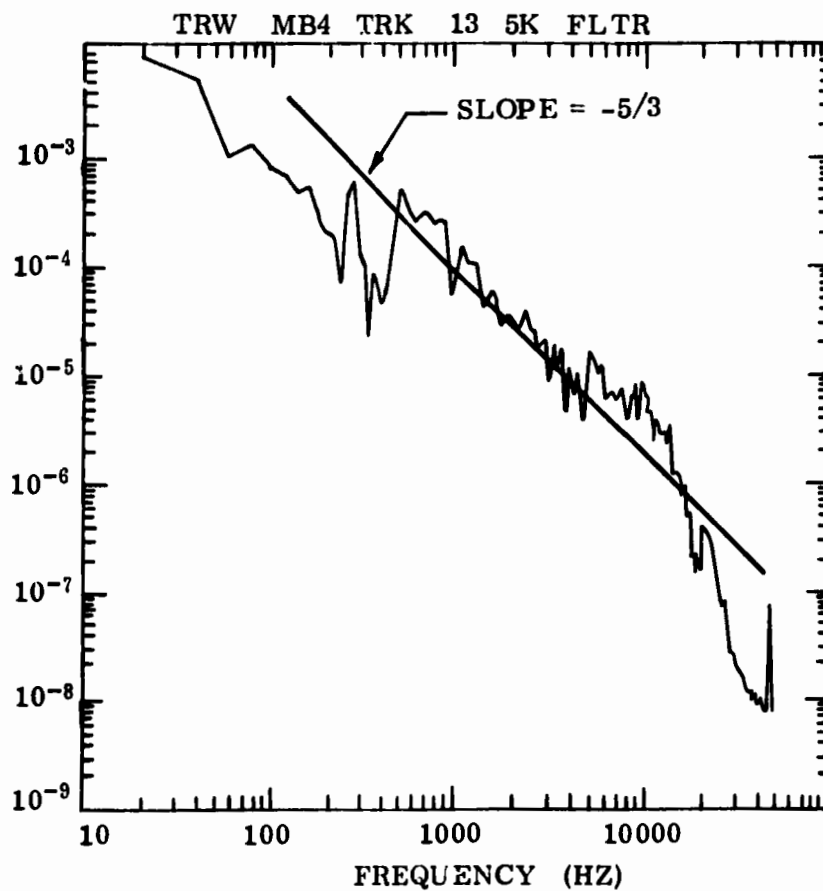


Figure 78. Power Spectrum of MB-4 Temperature Measurement

predicted using the 43 m HOB and the 2 material equation of state were in reasonably good agreement with the preliminary data determinations.

Figure 79 compares the LASL determined temperatures for MB-2 using the AGA camera with the HULL predictions. That the AGA temperatures are low compared to prediction is probably due to the fact that LASL made no allowance for less than unity emissivities, transient cloud transparencies, or masking of the hottest regions by optically thick outer regions. All of these omissions are in the direction to depress the measured temperature determination. That both the 5  $\mu$  and 10  $\mu$  measurements are so close to each other is probably due to the sharp temperature gradients being observed.

Figure 80 presents a comparison of HULL predicted torus dimensions as a function of time with visual (photographic) data. The correspondence is very good.

Figure 81 is a comparison of fireball and debris cloud altitude versus time as observed visually (photographically) and as calculated by the HULL code. Again, the correspondence between prediction and experimental measurement is seen to be quite good.

Torus formation on all single shots was good although for event MB-2 the seedant dispersal was quite non-uniform and the day was somewhat cloudy so that satisfactory optical records were not obtainable. Infrared observations, however, confirmed good torus formation.

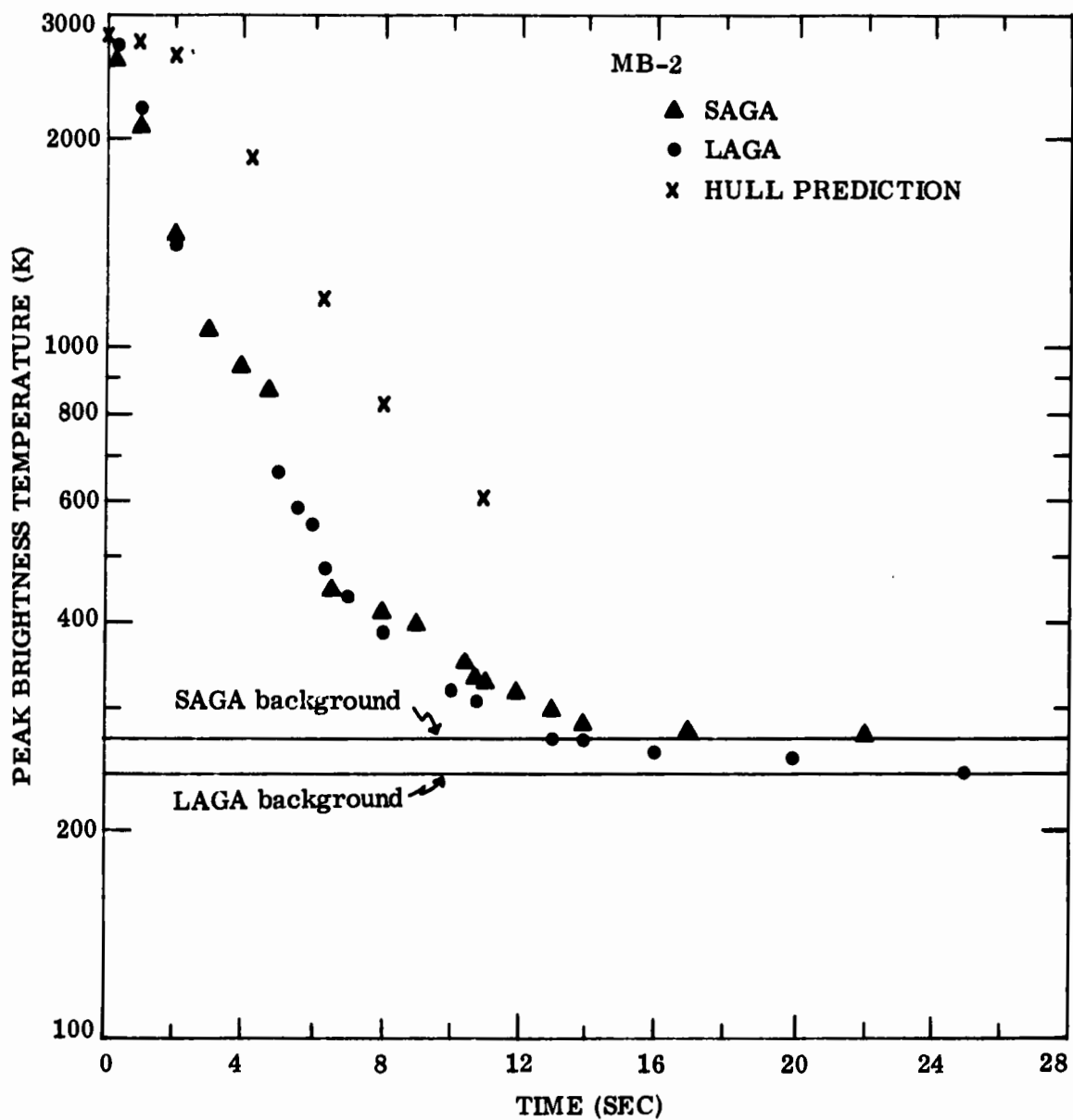
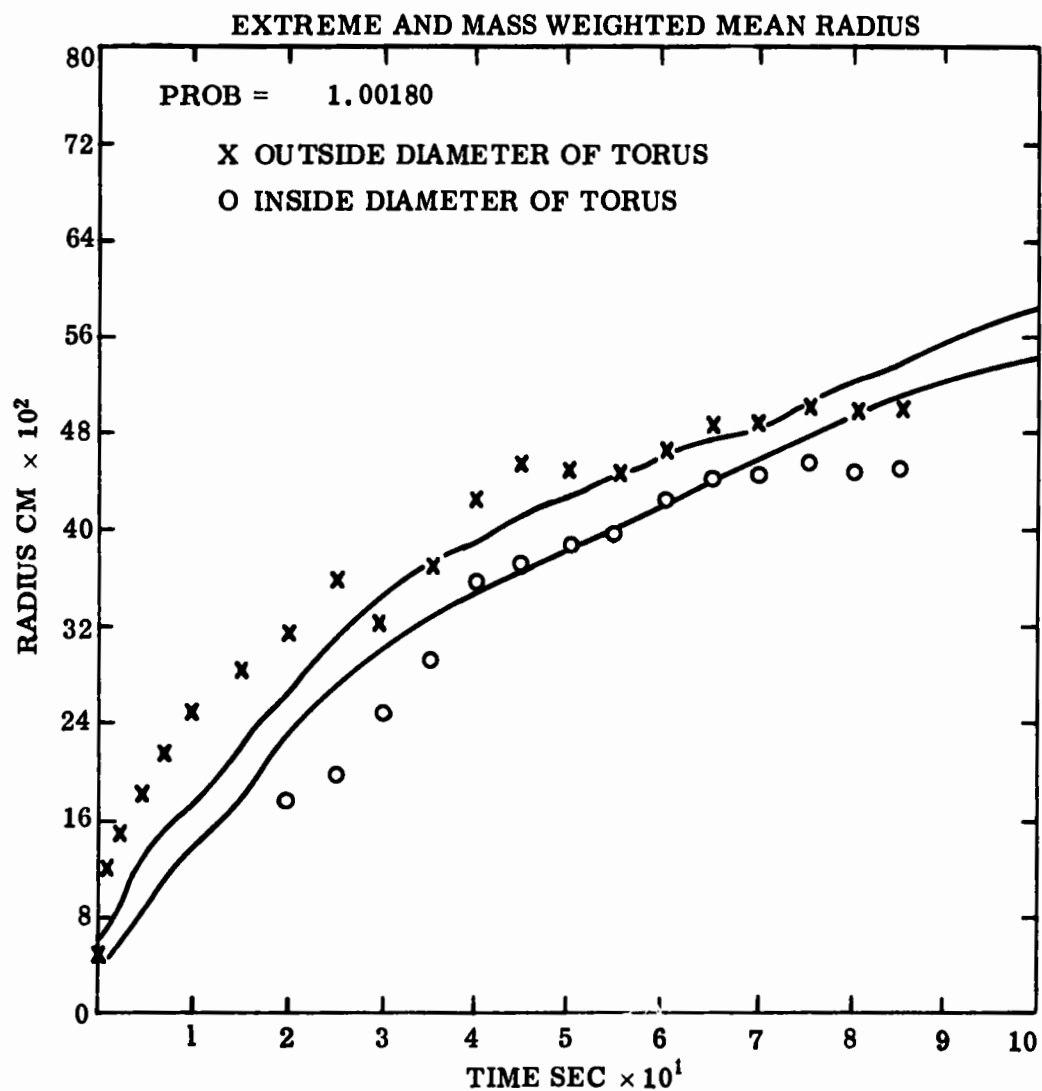


Figure 79. Comparison of LASL Computed Temperatures with HULL Predictions - Event MB-2



AFWL HULL CALCULATION OF 5 M CH<sub>4</sub> BALLOON AT 43 M SAP INPUT

Figure 8) Torus Radius versus Time-Optical Measurements and HULL Predictions Compared

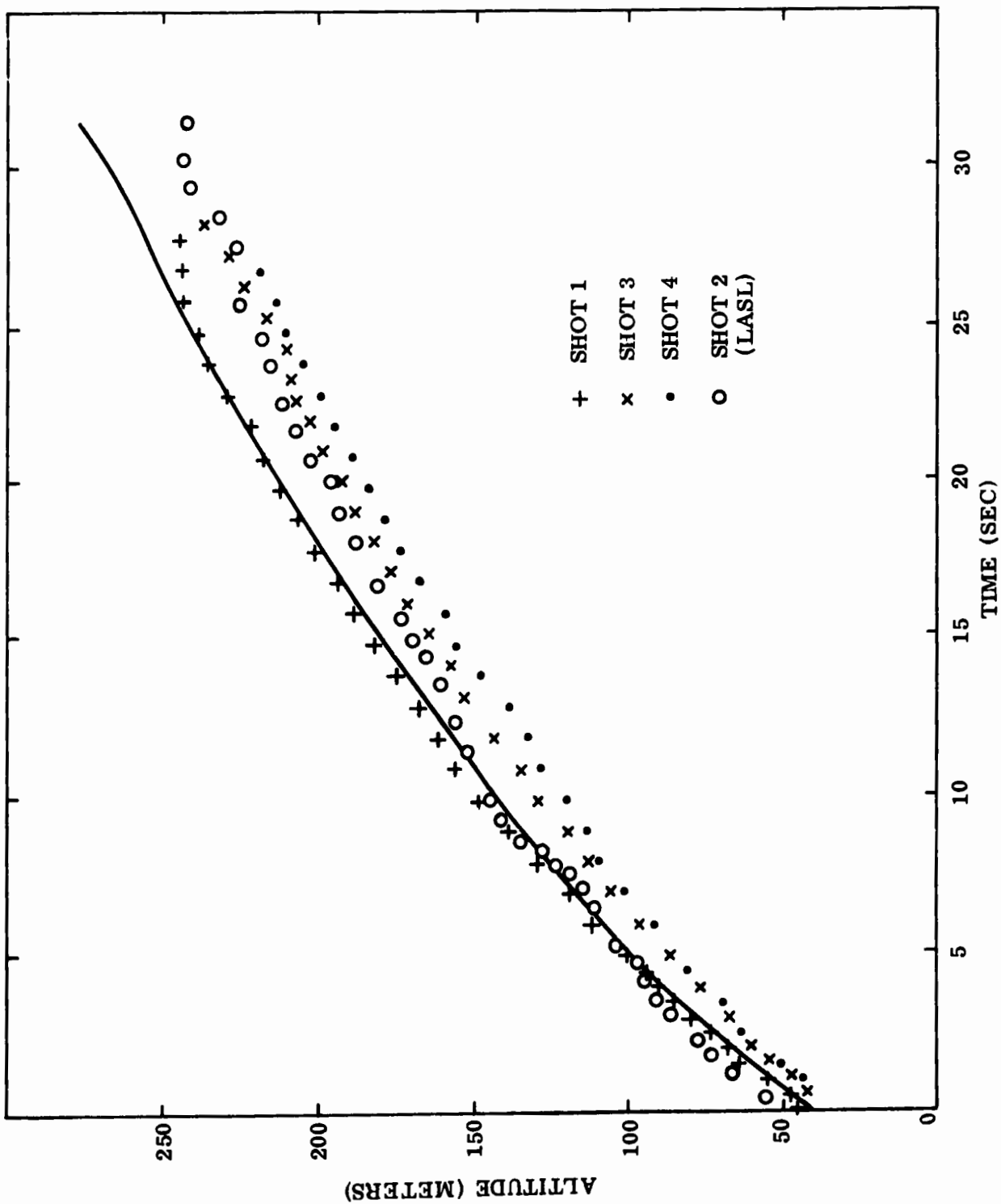


Figure 81. Altitude versus Time - MB Series and HULL Prediction Compared

## REFERENCES

1. Fields, S.F., "High Altitude Blast Generation System: Detonable Gas Mixing Experiments," Final Technical Report GARD Project 1550, General American Transportation Corp., 1972.
2. Bigoni, R. A., and D. A. Matuska, "Gas Explosive Simulation Technique," AFWL-TR-73-129, Air Force Weapons Laboratory, Kirtland AFB, New Mexico, May 1973.
3. Whitaker, W. A., Nawrocki, E. A., Needham, C. E., Troutman, W. W., "Theoretical Calculations of the Phenomenology of HE Detonations," AFWL-TR-66-141, Air Force Weapons Laboratory, Kirtland AFB, New Mexico, November 1966.
4. Doan, L. R., Nickel, G. H., "A Subroutine for the Equation of State of Air," RTD (WLR) TM-63-2, Air Force Weapons Laboratory, Kirtland AFB, New Mexico, May 1963.
5. Powers, C. R., Kendall, "Users Manual Aerotherm Chemical Equilibrium Computer Program," Aerotherm Corporation Report, May 1964.
6. Bronfin, B. R., et al., "Development of Chemical Phase Computer Models," AFWL-TR-73-48, 1973.
7. Davidon, W., ANL-5990, AEC R&D Report, Argonne National Laboratories, November 1959.
8. McClatchey and Selby, Optical Physics Laboratory, Air Force Cambridge Research Laboratories, private communication.
9. Alyea, F. N., "Infrared Vidicon Observations of Exploding Balloon Events," Technical Report RADC-TR-73-365, Oct. 1973.
10. Alyea, Fred N. and Griffith, George, A., "Predictions for Infrared Vidicon Observations of Exploding Balloons," General Electric Company, Space Sciences Laboratory, 1973.
11. Altschuler, T.L., "Infrared Transmission and Background Radiation by Clear Atmospheres," General Electric Company Document No. 61SD199, December 1961.
12. Gulatsi, Richard, L., "Test Plan for Infrared Vidicon Observation of Exploding Balloon Events," General Electric Company, Space Sciences Laboratory, 1973.
13. Carlos, R. C., Los Alamos Scientific Laboratory, Private Communication dated 4/3/74 to Major R. Bigoni.
14. Sandford, B. P., and R. J. Huppi, "GEST Infrared Spectra at 1.56 to 4.67 Microns," Preliminary Report, Air Force Cambridge Research Laboratories, Bedford, Massachusetts 01730, March 1974.

## REFERENCES (CONTINUED)

15. Baum, N.P., and J. R. Bettis, "Investigation of the Feasibility of Using Raman Scattering to Determine Air Entrainment Rates," CERF final report on T. D. 11.01/00 University of New Mexico., Albuquerque, New Mexico, February 1974.
16. Batt, R.G., "GEST-Temperature Measurement Task," Quick Look Report 25308-6001-RU-00, TRW Systems Group, Redondo Beach, California 90278, March 1974.
17. Alyea, F.N., R. L. Gulatsi, and G. Liebling, "Infra-Red Vidicon Observations of Exploding Balloon Events," RADC-TR-74-145 Rome Air Development Center, April 1974.